Universidad de Guanajuato

División de Ciencias e Ingenierías
Campus León

The low-energy electron/positron beam for the MINERνA Test Beam second run

Thesis
submitted in partial fulfilment for the degree of
Master of Physics

By:
Manuel Alejandro Ramírez Delgado

Advisor: **Dr. Julián Félix Valdez**

Co-Advisor: **Dr. Leo Bellantoni**

León, Guanajuato - July 30, 2015

ABSTRACT

MINERvA is a neutrino scattering experiment. Its detector is on the way of the NuMI beam at Fermilab. It is focused on the measurement of low energy neutrino interactions and on the study of the dynamics of nucleons of different materials that affect these interactions.

To calibrate the detector's response to electrons , pions and protons, a down-scaled detector was built, the MINERvA Test Beam detector. It already took data in the 0.4-2.0GeV region (first run), and it has just finished taking in the 1.55-8GeV region (second run); overlapping both stages.

This work presents some characteristics of the low-energy electron/positron beam (1.55-7GeV) used for such calibration. These characteristics are: Beam linearity, measurement of the electron/positron content, efficiency for "tagging" electrons and positrons, difference between polarities, and the reproducibility or tuning of the beam. This study was accomplished with a lead-glass electromagnetic calorimeter and a Cherenkov detector.

ACKNOWLEDGEMENTS

This work means in a sense, my introduction to experimental particle physics. Such a way to do it, in the Fermi National Accelerator Laboratory (Fermilab). Of course, I would not have done anything without the help of Dr. Leo Bellantoni. He guided me step by step from the beginning of my stay to the accomplishment of these results. So, I must and I am glad to give my heartfelt thanks to him, for all his patience and for sharing his great and valuable knowledge and expertise.

Equally grateful, I am with my advisor of the University of Guanajuato, Dr. Julián Félix. He was who with his particular teaching style, helped me to go through this pathway. He also introduced me with the MINERvA collaboration and made me part of this world-leading neutrino experiment.

I would also like to thank all MINERvAns, all collaborators for "bringing neutrinos into sharp focus". Specially Jorge Morfín for this huge opportunity and for his confidence in myself.

Testbeamers and FTBF people, awesome in all senses, gave also a hand, if not both, whenever I asked for. Many thanks to Geoff Savage, Anne Norrick, Rob Fine, Aaron Bercellie, Mateus Carneiro, and especially to Ewa Skup for showing me how to handle for the first time the instrumentation and programs involved.

My fellow countrymen and friends: Rafa, Pavel, Edgar and his family, the Mexican enclave at Fermilab, being like a family while I was there.

To my beloved parents Irma and José, who have loved me and have shown me a good example throughout my life. They; my siblings: Pepe, Juan y Mariana; and of course you, Maricruz, who set me free to do what I wanted to do, are the pushing force as always.

Content

List of Figures

List of Tables

Chapter 1

INTRODUCTION

1.1 The MINERvA Experiment

1.1.1 Introduction

MINERvA is a neutrino scattering experiment which uses the NuMI (Neutrinos at the Main Injector) beamline at Fermilab. It measures low energy neutrino interactions both in support of neutrino oscillation experiments and in the study of the strong dynamics of the nucleons and nucleus that affect these interactions [1].

Its construction was finished by march 2010, and studied interactions of few GeV neutrinos and anti-neutrinos until April 2012. Now, the collaboration is analysing that dataset. The results so far, have already shown evidence for the effect of multi-nucleon processes in elastic scattering, and this observation will improve the knowledge of energy reconstruction in neutrino oscillation experiments.

The study of neutrino interactions is done over a variety of different nuclei: helium, carbon, oxygen, lead, and iron, which complement the already known electron scattering data in helping to understand the weak interaction in the nuclear level and complete the scheme of neutrino masses and mixings.

The next generation of accelerator-based long-baseline experiments is looking to determine the mass hierarchy of neutrinos and test for CP violation by comparing the oscillation probabilities for neutrinos and antineutrinos. Achieving the level of precision desired in these measurements requires a detailed understanding of neutrino- and antineutrino-nucleus scattering processes in the relevant energy range of a few hundred MeV to a few GeV. Currently, however, processes providing signal and background channels for these experiments are, in many cases, either poorly measured or suffer from discrepant measurements across various experiments. In addition, another

important feature of oscillation experiments is the measure of oscillation probabilities as a function of the neutrino energy, requiring to have good models showing the relationship between the initial neutrino energy and the visible energy deposited in the detectors. Such models must incorporate the impact of the complicated nuclear environment in which the interactions occur. Studies have shown that neglecting these effects can lead to biases in the neutrino energy determination. So, the impact of the initial state as well as the interactions of final-state particles traversing the parent nucleus must be understood.

Using measurements of cross sections and comparisons among different nuclear targets, MINERvA can provide data to improve the models of neutrino-nucleus scattering and thus to reduce systematic uncertainties in the results from oscillation experiments. This new models could improve and guide, likewise, future experiments. Its studies are divided into two principal branches:

Low Energy Studies:

- Study both signal and background reactions relevant to oscillation experiments.
- Study nuclear effects in inclusive reactions.
- Measure nuclear effects on exclusive final states.

  *As a function of measured neutrino energy.

  *Study differences between neutrinos and anti-neutrinos.

Medium Energy Studies:

- Structure functions on various nuclei.
- Study high energy feed-down backgrounds to oscillation experiments.

To reach these goals, one of the MINERvA requirements is to calibrate its response to the particles produced during the interaction of neutrinos with its detector. For this reason a scale-down detector was built and placed in the Fermilab Test Beam Facility (FTBF). This detector (MINERvA Test Beam detector) shares the main characteristics of the MINERvA main detector (explained in the following sections). Two different runs were planed for the Test Beam detector in order to match, respectively, the low and medium energy ranges at which the main detector would be run. The first run was accomplished during the summer of 2010 with very important results (section 1.2.3). The second run has not finished yet, and its first dataset already taken, is still under analysis.

The way each run took data was quite different in some aspects, the instrumentation and devices needed were different or at least placed in different configuration, given the difference in the energies.

In order to test the detector's response to different particles, many requirements were needed. Also, each kind of particle gave an extra help. Protons, for instance, were used to calibrate the

Time of Flight System or "TOF"; muons (not checked for response) as cosmic rays or beam-muons were useful to give an average uniform response among the scintillator strips [1].

The electron/positron composition of the beam or the "electron/positron beam", gives interesting an valuable information about the whole beam itself (which will be explained in the remainder chapters).

By the use of specific instrumentation, such as a lead-glass calorimeter and a Cherenkov counter, the electron/positron beam gives valuable information about: the linearity of the beam; efficiency for tagging electrons; differences between positive and negative polarities; the tuning or reproducibility of the beam; and the percentage of electrons and positrons at different energies. Determining these characteristics of the beam is the main goal of the present work.

1.1.2 The NuMI beamline

The NuMI beamline delivers an intense ν_μ beam of variable energy (2-20 GeV) directed into the Earth at 58mrad for short (∼1km) and long (∼700-900km) baseline experiments [2].

NuMI is a tertiary beam resulting from the decays of pion and kaon "secondaries" produced in the NuMI target. Protons of 120GeV are fast-extracted (spill duration 8.6μs) from the Main Injector (MI) accelerator and bent downward by 58mrad toward Soudan, MN (as is seen in figure 1.1)

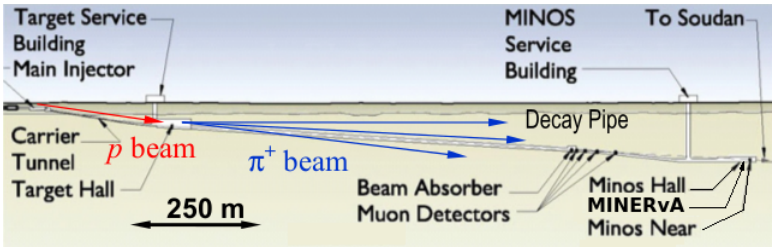

Figure 1.1: Side view of the NuMI beamline.

The line is designed to accept $4{\times}10^{13}$ protons per pulse (ppp). The repetition rate is 0.53Hz, giving $\sim 4 \times 10^{20}$ protons on the target per year. The MI beam is extracted by a set of three kickers. The transport line to the NuMI target is 350m long and it has 2 toroids, 44 loss monitors, 24 BPM's, and 19 dipole correctors [2].

The primary beam is focused onto a graphite production target of $6.4 \times 15 \times 940 mm^3$, segmented longitudinally into 47 fins. The beam size at the target is 1mm.

The particles produced in the target are focused by two magnetic "horns". The relative placement of the two horns and the target optimize the momentum focus for pions, hence the peak neutrino beam energy.

The particles are focused by the horns into a 675m long, 2m diameter steel pipe evacuated to ∼1 Torr. This length is approximately the decay length of a 10GeV pion. 95% of the entering pions traverse the front face of the pipe. The decay volume is surrounded by 2.5-3.5m of concrete. At the end of the decay volume there is a beam absorber consisting of a $1.2 \times 1.2 \times 2.4m^3$ water-cooled aluminum core, a 1m layer of steel blocks surrounding the core, followed by a 1.5m layer of concrete blocks.

Ionization chambers are used to monitor the secondary and tertiary particle beams. An array is located immediately upstream of the absorber, as well as at three muon "pits", one downstream of the absorber, one after 8m of rock, and a third after an additional 12m of rock. These chambers monitor the remnant hadrons at the end of the decay pipe, as well as the tertiary muons from π and κ decays. Figure 1.2 shows the arrangement of the NuMI line.

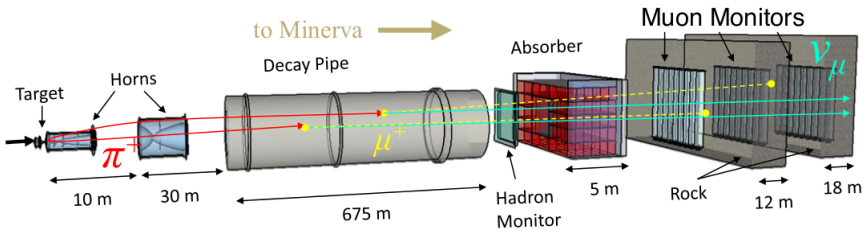

Figure 1.2: The NuMI beamline arrangement.

1.1.3 The MINERvA detector

The MINERvA full or main detector is comprised of a finely-segmented scintillator-based inner tracking region surrounded by electromagnetic and hadronic sampling calorimetry. The upstream portion of the detector includes planes of graphite, iron and lead interleaved between tracking planes to facilitate the study of nuclear effects in neutrino interactions.

Coordinate system

It is very important the definition of the MINERvA coordinate system. The experiment defines the Z axis as parallel to the floor, most nearly in the direction of the neutrino beam. The neutrino beam points down at 3.34° with respect to the Z axis. MINERvA and MINOS share this axis, which points approximately north. The Y axis points up and the X axis completes the right handed coordinate system by pointing "west" [3].

The physics goals of MINERvA require a detector that can resolve multi-particle final states, identify the produced particles, track low-energy charged particles (for energies greater than about 100 MeV), contain electromagnetic showers, contain high-energy (up to at least 10GeV) final states, and resolve multiple interactions in a single beam spill. The detector must include targets with a wide range of nucleon number "A" to enable studies of the nuclear dependence of neutrino

interactions. Full containment of events requires that the inner region be surrounded with electromagnetic and hadronic calorimetry. Ideally, charge identification would be included by adding a magnetic field, but this was no practical for the main detector, the same as the containment of high energy muons. Nevertheless, MINERvA has been placed immediately upstream of the Main Injector Oscillation Search (MINOS) near detector [4], a neutrino detector composed of magnetized iron plates interleaved with scintillator planes, charge and energy measurements of forward-going muons can be made.

A schematic view of the MINERvA detector is shown in figure 1.3.

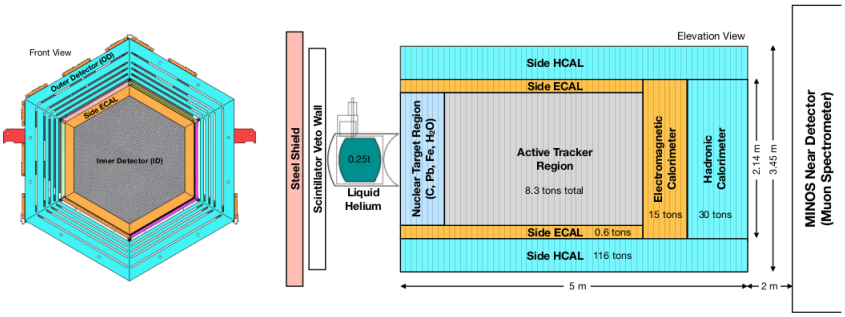

Figure 1.3: MINERvA main detector. Left: front view of a single detector module. Right: side view of the complete detector showing the nuclear target, the fully-active tracking region and the surrounding calorimeter regions.

The main MINERvA detector is segmented transversely into: the inner detector (ID), with planes of solid scintillator strips mixed with the nuclear targets; a region of pure scintillator; downstream electromagnetic calorimetry (ECAL) and hadronic calorimetry (HCAL); and an outer detector (OD) composed of a frame of steel with embedded scintillator, which also serves as the supporting structure. Both the ID and OD are in the shape of a regular hexagon. For construction and convenience of handling, a single unit of MINERvA incorporates both the scintillator and outer frame. Up to two planes of scintillator are mounted in one frame, called a "module". Figure 1.3 (left) shows a view of a tracking module. There are three orientations of strips in the tracking planes, offset by 60° from each other, which enable a three-dimensional reconstruction of tracks. The 60° offset fits naturally with the hexagonal transverse cross section of the detector.

The core of the detector is the active tracking region, composed purely of scintillator, which serves as the primary fiducial volume where precise tracking, low density of material, and fine sampling ensure that some of the most difficult measurements can be performed. These measurements include particle identification using energy loss per unit length (dE/dx), and reconstruction of the neutrino interaction vertex in the presence of several final state charged particles. The upstream part of the detector contains solid targets of carbon, iron, and lead interleaved with the scintillator planes. Because these targets are relatively thin, the ability to precisely reconstruct the location of the interaction vertex is crucial for studies of the "A" dependence.

Electromagnetic calorimetry is accomplished using a 0.2cm thick by 15cm wide lead "collar" between each scintillator plane in the central tracking region (orange region in figure 1.3). Additionally there are lead plates, each 0.2cm thick, covering the full transverse span of the inner detector between each scintillator plane within the 10 modules immediately downstream of the tracking region. For hadronic calorimetry the outer frames of all modules are instrumented with strips of scintillator interleaved into the steel. Further, in the most downstream 20 modules of the detector, the inner detector scintillator planes alternate with 2.54cm thick steel plates. Thus the combination of the outer frame detectors and the downstream calorimeter section provides containment of hadrons initiated by interactions in the tracking region.

Tracking modules

Tracking modules consist of two scintillator planes each composed of triangular scintillator strips (explained below). Each plane consists of 127 strips glued together with epoxy. Sheets of Lexan cover the planes and are attached with epoxy to make them light tight and to add rigidity. Black PVC electrical tape is used to seal joints in the Lexan and patch any light leaks. Optical epoxy provides the coupling between the scintillator and wave length shifting (WLS) fibers (explained below).

A plane can have one of three different orientations, referred to as X-planes, U-planes or V-planes according to the coordinate in the MINERvA system in which each plane measures particle hit positions. X-planes have scintillator strips aligned vertically, hence hits in this view give position information in the horizontal or X-direction. The V- and U-planes are rotated 60 degrees clockwise and counter-clockwise from the X-planes in the X-Y plane, respectively. Three different views are used in order to avoid ambiguities with reconstructed hit associations that can occur when multiple tracks traverse two orthogonal planes. Each tracking and electromagnetic calorimeter module has one X-plane, and either a U- or V-plane, with modules alternating between a UX or VX structure with the X-planes always located downstream of the U- or V-planes. The nuclear target region contains 22 tracking modules, and the central tracking region contains 62. The tracking modules are designed to perform electromagnetic calorimetry using a 0.2cm thick lead collar that starts at roughly 90cm from the module center and extends to the outer frame. The collar forms a hexagonal ring which purpose is to reduce the leakage of electromagnetic showers that originate in the central detector.

Electromagnetic and hadronic calorimeters

An ECAL module is very similar to a central tracking module. It differs in that it has a 0.2cm thick sheet of lead covering the entire scintillator plane instead of a 0.2cm thick lead collar covering only the outer edge of the scintillator region. A transition module is placed between the last central tracking module and first ECAL module. This module contains a 0.2cm thick lead sheet on the downstream end of the last plane in the module so that each plane of the ECAL has a lead absorber upstream of it. The fine granularity of the ECAL ensures excellent photon and electron energy

resolution and provides directional measurement for these particles. There are 10 modules in the ECAL region of the detector (figure 1.3).

On the other hand, the HCAL consists of 20 modules that are similar to the tracking modules, however, instead of two planes of scintillator in each module, there is only one plane of scintillator and one 2.54cm thick hexagonal steel plane in the inner detector region. The scintillator planes located in the HCAL have a repeating pattern of XVXU.

Solid nuclear target modules

In order to study neutrino interactions on different nuclei, the most upstream part of the detector includes five layers of passive targets, the "nuclear targets", separated by four tracking modules each. The four modules (eight planes of scintillator) between one target and the next ensure good vertex position resolution for events originating in the nuclear targets. Each solid nuclear target is mounted in the same instrumented hexagonal steel frame as the scintillator planes for ease of detector construction and for event containment. The five targets are configured such that the thicker targets are most upstream, and the thinner targets are downstream. This optimizes reconstruction of events occurring upstream. The thinner targets are included in order to study specific reactions that contain low-momentum final-state particles. Except for the fourth of the five targets, all contain mixed materials with different orientations in order to minimize the effect of acceptance differences for different regions of the detector. Target 4 is pure lead and aids in upstream electromagnetic calorimetry and serves as the thinnest lead target. Targets 1, 2, and 5 are mixed steel and lead. The steel plate section is larger than the lead plate section, with the dividing line 20.5cm from the plane center. Target 3 is composed of graphite, iron and steel. The graphite covers half the area of the hexagon, the steel one-third, and the lead one-sixth. The orientation of the planes, as viewed looking down- stream, is shown in figure 1.4.

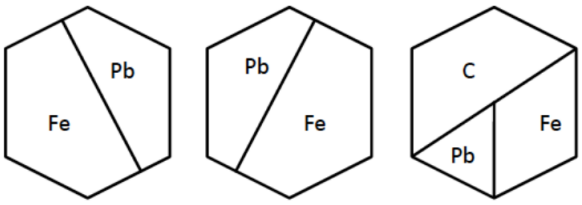

Figure 1.4: Orientation of the nuclear targets looking downstream. Targets 1 and 5 have the leftmost orientation, target 2, the middle orientation, and target 3 the rightmost orientation.

The orientation of the planes along the axis of the beamline is shown in figure 1.5.

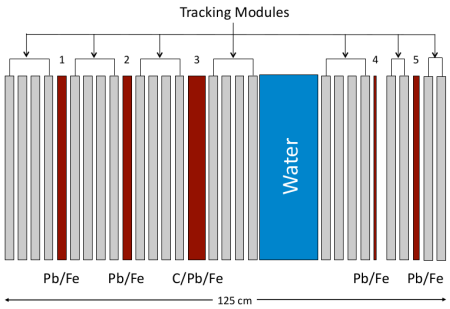

Figure 1.5: Orientation of the nuclear target region along the beamline axis. The thinner targets are located downstream and the thicker targets are located upstream. Extra targets can be placed. A water target is shown in this figure.

Optical system and DAQ

The incoming particles into the scintillator strips (made from polystyrene pellets) produce light in this material, the light amplitude is proportional to their energy. There are wavelength shifting (WLS) fibers in the center of each strip, their purpose is to shift the wavelength of the light produced in the strips to that wavelength at which the photomultiplier tubes (PMTs) have their maximum sensitivity.

The PMTs are in charge of transforming the incoming light into electrical pulses at its output, by means of the photoelectric effect. These pulses carry information about the interaction's energy produced inside the strips. The PMTs are mounted in a front-end electronics board (FEB) which handles the signals to be sent to the data acquisition system (DAQ) and also has a Cockcroft-Walton generator for the high voltage to the PMTs, and two additional optical fiber ports terminated by diffusers, which permit the controlled light injection to all the pixels, for purposes of gain measurement correction.

The readout electronics and the DAQ consist basically in the equipment processing the fast analog signals from the PMTs. These are sent to the FEBs, which digitize timing and high-pulse signal, they also have the high voltage source for the PMTs, and communicate with the VME (a high speed bus) readout controller modules. Up to ten FEBs form a chain, which is connected at both ends to a VME, called the Chain Read Out Controller (CROC). Trigger and timing information is sent to the CROC from a module called the CROC Interface Module (CRIM). The readout system is a non-trigger integration-style one, which means that there is a timing based integration gate synchronized to the Main Injector timing signal, and therefore, individual events are separated by timing information [5].

The scintillator strips for the inner detector (ID) have the shape of a triangle for their cross section, with 17±0.5mm high, and 33±0.5mm wide. The strips for the outer detector have different cross sections, with 19±0.5mm high and 16.6±0.5mm wide.

The WLS fibers are 1.2mm diameter, 320cm long, made of multiclad. They are readout just in one end and the other is mirrored to maximize light collection.

The PMTs are H8804MOD-2, made by Hamamatsu Photonics. These 12-stage photo tubes can detect the light from a minimum ionizing particle inside a strip, this model has an 8×8 array of pixels laid out on a 2cm×2cm grid, i.e., 64 pixels per PMT. Their spectral response goes from 300-650nm with a peak wavelength at 420nm at which its quantum efficiency is 20%, and an average anode current of 0.1mA.

Track reconstruction

When the position of the signals taking place in the scintillator strips are analysed, it can be seen frequently, a kind of well defined trajectory, due to a charged particle. The reconstruction of this trajectory is called a track. When a particle decays or undergoes a large angle due to scattering, it is necessary the use of multi tracks.

There is a pattern recognition depending on the type of cluster and on the orientation of the panel in which the cluster is present. Track candidates do not need to share clusters, which means that they can have gaps, and in this way, track candidates can follow a particle's trajectory even when these pass through regions of "dead" material (non-scintillating material), such as lead, iron, etc. 3-D track reconstruction is possible using algorithms based on the orientation of the strips (X, U and V views).

Energy and muon momenta are measured using the MINOS calorimetry. Muons with momenta between 0.5 to 6.0GeV are stopped by MINOS calorimeters, while muons with higher momentum are either stopped in the MINOS spectrometer or scape. In the figure 1.6 is shown a reconstructed neutrino event.

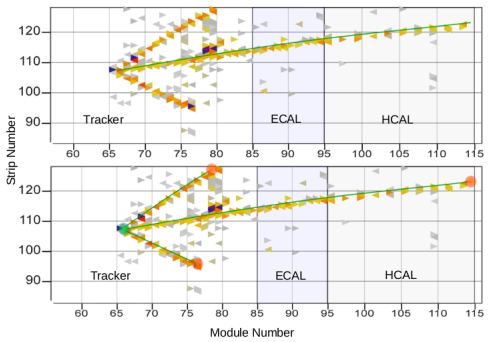

Figure 1.6: X-view of a neutrino interaction.

1.2 Test Beam Detector, Response Calibration

1.2.1 Introduction

In 2010 a scale-down detector was placed in the Test Beam facility to validate the MINERvA's main detector calorimetric response to electrons, pions and protons [6]. The first run at that year tested the Test Beam detector using particles with momenta between 0.4 and 2.0GeV/c. The reason for this energy range has to do with the fact that this range is well-matched to the energy range of protons, pions, and electromagnetic showers in the 2010 to 2012 MINERvA low-energy neutrino and antineutrino data. This is especially true for the reactions from neutrino quasi elastic scattering through Δ and N^* resonance production. Measuring differential cross sections for these exclusive final states is a break point of the MINERvA neutrino physics program. These energies also cover the lower part of the range expected for hadrons produced in neutrino deep inelastic scattering. In the fall of 2014, began the second run to calibrate the MINERvA main detector, but now in the medium energy range, from 1.55GeV/c to 8GeV/c momenta. This run is currently taking data. The reason for this "medium" energy range is the interest for the MINERvA data in the NuMI NOvA-era medium energy beam, which is dominated by deep inelastic scattering (DIS) interactions.

In order to understand how the Test Beam detector works it is mandatory to know first how the incoming beam is, what is made of, and some other characteristics. Therefore, the following subsection is devoted to this aim.

1.2.2 Fermilab Test Beam Facility and beam production

FTBF is operated by the Particle Physics Division, and it is a high energy beam facility devoted to Detector, Research and Development [7]. The facility is located on the Fermi National Accelerator Laboratory [8], in Illinois, USA, on the west side of the Meson Detector Building.

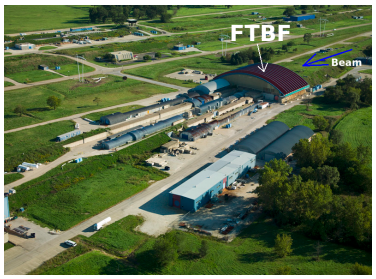

Figure 1.7: Fermilab Test Beam Facility.

The facility uses two versatile beamlines (MTest and MCenter) to provide beam in a multitude of particle types and a range of energies, in which users can test equipment and detectors.

MTest

The MTest (Meson Test) areas are the most commonly used (the only involved in this work). They have all of the features in facility infrastructure, and all of the instrumentation available to them. The primary beam (described below) consists of high energy protons (120GeV) at moderate intensities (∼1-300kHz). This beam can also be targeted to create secondary particle beams of energies down to about 1GeV, consisting of pions, muons, and electrons.

MCenter

Meson Center, commonly referred to as MCenter, can be divided into two distinct areas. The first is the primary proton beamline. At the upstream end of an area called MC6, the beam can interact with a long, narrow solid copper target to create the so called "tertiary particles".

But before going further, it is necessary to understand, how the beam used is produced and delivered to MTest and MCenter.

Beam production and delivery path

The beam sent to FTBF begins in the negative hydrogen ion source [9]. The radio-frequency quadrupole accelerator, or RFQ, is the starting point of the Fermilab's chain of accelerators. The 11-foot-long accelerator takes the low-energy proton beam from the ion source, accelerates and "bunches" it into separate packets of particles, and injects it into Fermilab's linear accelerator, or Linac. The RFQ accelerates the beam from 35keV to 750keV.

Fermilab's linear accelerator, better known as the Linac, is a roughly 150-meter straight accelerator. It accelerates the ions to 400MeV, and then extracts them to the Booster Accelerator. As the ions are injected into the Booster, the electrons are stripped off leaving 400MeV protons to circulate in the Booster. Proton beam enters the Fermilab Booster, accelerating through its approximately 460-meter-circumference ring to an energy of 8GeV. The Booster then provides beam to the Recycler.

The Recycler is a kind of staging area for proton beams after they exit the Booster. Once the beam enters the Recycler, a 2-mile-circumference ring, it is "slip stacked" combined into batches of protons to form a more intense beam. Once this is done, the proton beam enters the Main Injector, on top of which the Recycler sits.

The Main Injector, situated directly beneath the Recycler in the same tunnel and two miles around, ramps up the proton beam from the Recycler, from 8GeV to 120GeV. It delivers beam to the MTest and MCenter areas, to the neutrino area (Sea Quest) through the Switch Yard (shown below), and of course to the MINERvA and MINOS detectors.

Figure 1.8 shows the chain of accelerators and beamlines needed for the particles to reach the Test Beam facility.

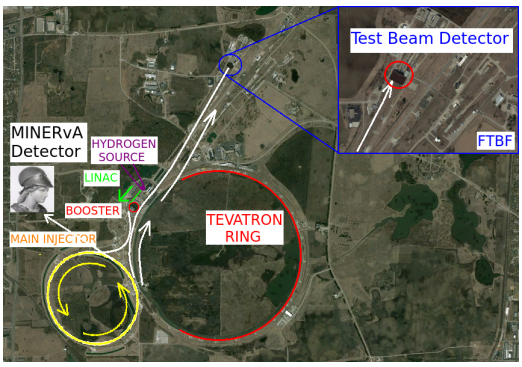

Figure 1.8: FTBF Location and the accelerators chain towards the Test Beam facility.

Beam destined for Switchyard is extracted in a mode called "slow spill". The slow spill mode uses the QXR (Quadrupole eXtractor Regulator) quadrupole circuit to resonantly extract beam over ∼4 seconds.

In its way from the Main Injector to the Switch Yard, the beam passes through the P1, P2 and P3 lines. These lines make the connection line between the MI and the Tevatron ring and between the Tevatron ring and the Switch Yard. They contain the magnets steering and focusing the beam, the vacuum system, cooling system, and many other devices.

The Switchyard begins in the Transfer Hall, where the P3 line ends and the beamline branches away from the Tevatron to continue onwards through the Transfer Hall to the "Continental Switchyard", i.e., enclosures B, C, D and E, as shown in figure 1.9

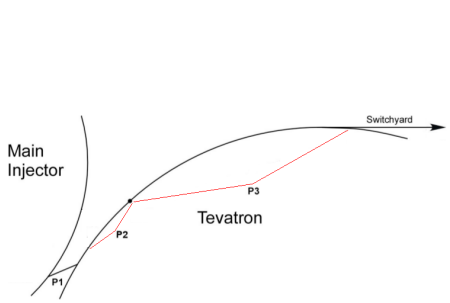

(a) Transition between the Main Injector and the Switchyard.

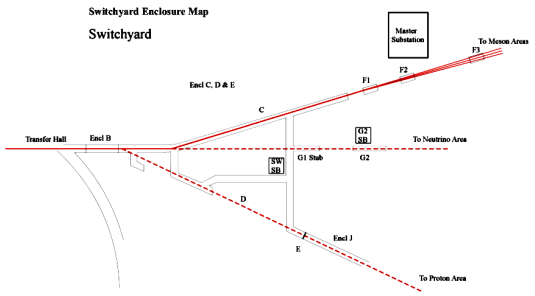

(b) Inside the Switchyard.

Figure 1.9: Beamline from the Main Injector ring to Mtest.

Towards the end of enclosure B, the beam is split. The position of the Meson Septa (S:MSEP), determines whether the beam will pass through the magnetic field gap to be bent west and continue onward to Meson, or the field-free region which will let it pass to the Neutrino

beamline or let it pass through to the SY dump (located in enclosure C) [10, 11]. Then, in the enclosure C, if the beam is chosen to go to the meson area, it is split vertically by the "septa magnets" [10, 11], into two different beams. Next up is the F1 manhole, notable for containing the electrostatic septa (FSeps) that are capable of splitting the "Meson" beam vertically into 2 streams. Finally, the two streams of beam continue through the F2 and F3 manholes to the first Meson area enclosure, M01. At enclosure M01 the 2 vertically separated streams of beam coming uphill from the C enclosure have now diverged to about 1 inch apart. The beams rise up to M01 from enclosure C at an angle of about 1 degree. The upper stream is bent horizontally west into the Mtest beamline by the critical device for MTest enclosures MT6A and MT6B. MTest and MCenter share enclosures M01, M02, M03 and M05. By the end of M05, the beamlines have diverged sufficiently so there is finally room for independent enclosures, target halls, and shielding for each beamline. MTest concludes in enclosures MT6A and MT6B. All these areas are shown in figure 1.10 below.

The beam at MTest can be run in three different modes. In all cases the primary 120GeV protons from the enclosure-F1 triple split are transported through MW1W (the critical device which prevents the beam to reach some populated or dangerous areas) to an "aluminum target" on the upstream end of the Meson Target Train. The three modes determine whether the un-interacted protons traversing this target, the produced secondary pions produced in this target, or pions produced on the new target in M04, are transported to the Meson Test Facility in MT6. This point is the beginning of MCenter and MTest areas.

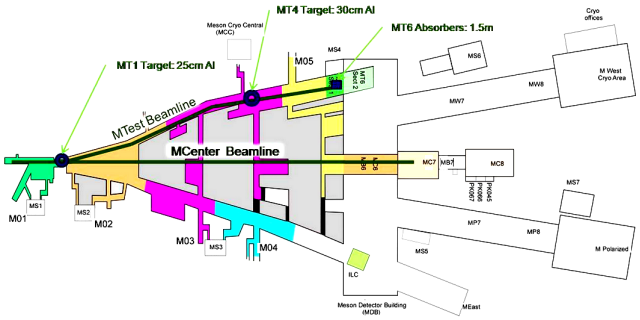

Figure 1.10: Meson facility areas.

Beam structure

The Booster captures the protons from the LINAC into 84 buckets (1 batch) and accelerates them. The particles are grouped in these small packets to have a more intense beam. Each of these buckets is 19ns long. Typically, 8-30 of these buckets are extracted to the Main Injector (MI) for Test Beam operations (a process known as Partial-Batching). MI works at a radio frequency (RF) value of ∼53MHz, each period is called a RF bucket, and is 19ns long. At the injection total energy

of 8GeV, the Main Injector has a circumference in time of T_0=11.13μs, which is exactly 7 booster batches long.

The Main Injector accelerates the beam to 120GeV at a frequency of 53MHz, at which point a process called "Resonance Extraction" is started and a fraction of the beam is resonantly extracted in a slow spill for each Main Injector rotation. Just one spill per minute is allowed and is ∼4s long. In figure 1.11 can be seen the beam time structure in the accelerators chain.

There is a kind of issue with the way particles are delivered to the Meson area. Some of the buckets deliver two or more particles. If beam were extracted smoothly, only one particle per MI RF bucket would be extracted per rotation, but for intensities up to 100kHz, double occupancy occurs 35% of the time and two particles are extracted instead [12]. This percentage can increase at higher intensities.

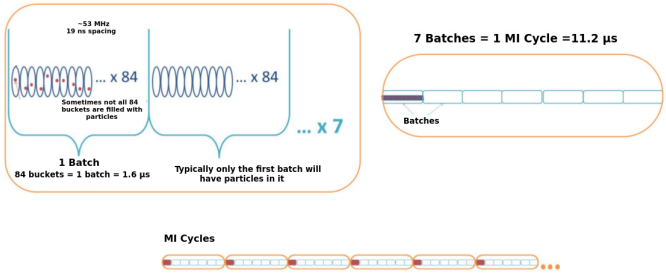

Figure 1.11: Beam structure.

MTest beamline

So far, it has been shown how the beam is, how is "created" and delivered upstream the Meson area. Once the beam reaches this area, the primary proton beam can be used to "create" different beams.

There are 2 movable targets in the MTest beamline:

- MT1 Target (25cm of aluminium) is 435m upstream of the MT6 enclosure.
- MT4 Target (30cm aluminium) which is 145m upstream of the MT6 enclosure.

There is also a pinhole (1mm×1mm) collimator (MT3CH) in MT3; and two absorbers each 1.5m long at the end of the MT6.2 enclosure (F:MT6AB1,2) used as beam dump for muon running.

The MT1 target is about 2.1m upstream of MT4. Secondary particles are created in this target. Both targets can be moved in various configurations to create the following beam modes:

MTest proton mode (primary beam)

In proton mode, most of the un-interacted 120GeV protons that survived the Meson Target Train are absorbed on the pinhole collimator in the M03 MTest alcove. The MT2Q1/2 and MT3Q1/2 doublets [11] are required to be off so that 120GeV protons cannot be focused through the pinhole collimator. The highly attenuated 120GeV proton beam is then transported to the Meson Test Facility in MT6 for different uses such as: beam profiles checks, wire chambers efficiency tests, or for testing and calibrating some other detectors.

MTest pion mode (secondary beam)

In pion mode, the 120GeV protons which interacts in the 30cm aluminium target on the Meson Target Train create copious lower energy pions (and other particles) at 0°. The MT2W1 double dipole string then separates the secondary hadrons from the more copious un-interacted 120GeV proton beam (the protons are absorbed on the steel pile in M02). The pions are then transported to the MT6 test facility. In this mode the pinhole collimator is removed from the beam in order to maximize the flux of pions reaching MT6, and the dipole magnets in M02 are limited by interlocks to 66GeV equivalent current or below (highest energy of pions in this mode).

There is a low-energy version of the pion mode: the MTest Low Energy Pion Mode. **Later it will be shown that this beam mode is the central part under study in this work**, given that it is the one used in the Test Beam second run. In this mode, 120GeV primary protons (the target in M01 is removed from the beam) are transported to the MT4 target in M04. The magnets downstream of MT4 are limited by interlocks to 30GeV.

MTest tertiary beam

This beamline was built in order to reach even lower energy values, from the secondary beam which consists of 16GeV pions among other particles (such as kaons). This secondary beam collides with a copper target placed at MCenter. Downstream the copper target there is a steel collimator from which all the particles (mostly pions, protons, electrons, and even a very few kaons and deuterons) exit. There is an angle relative to the incoming pions at which the particles exit, it depends on the experiment and detector under study. MINERvA used an exit angle of 16° as explained below.

Momentum, identification and position measurement of each particle were achieved by the use of a TOF system and MWPC's.

1.2.3 Test Beam detector-first run

Introduction

The detector consisted basically of 40 planes of scintillator with the same width (1.7cm) of those of the MINERvA's main detector, but with smaller transverse dimensions (107cm per side). These planes conformed the active area of the detector (see figure 1.12).

The planes were placed in two different configurations to emulate: the Hadronic Calorimeter (HCAL) and the Electromagnetic Calorimeter (ECAL) regions, and the downstream tracker and ECAL region, of the MINERvA full detector.

The HCAL/ECAL region had 20 planes with 1.99mm thick lead absorber (ECAL) followed by 20 planes with 26.00mm thick iron absorber (HCAL). The absorber was interleaved by placing one absorber upstream of each scintillator plane. The Tracker/ECAL region had 20 planes with no absorber (tracker) followed by 20 planes of ECAL [6].

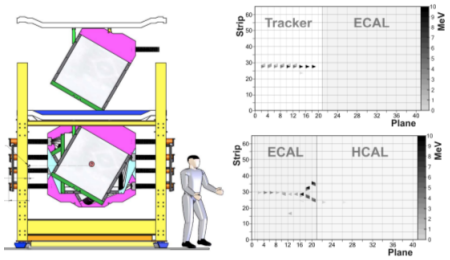

Figure 1.12: Test Beam detector, run 1.

The MINERvA Test Beam detector was meant to follow as much as possible, all the features of the main detector: its electronics, DAQ, software in general, etc. Nevertheless, there exist important differences between both detectors, for instance: The average fiber length in the Test Beam is half the length of the main detector, therefore the light yield is the double; the air gap between absorbers and planes is larger. These differences cause differences in response, and they are taken into account during the simulation and the calibration procedure. Calibrations were performed for the beamline momentum, response to cosmic muons and unrelated particle activity from the beamline.

All the data obtained from here were compared to a Monte Carlo simulation of the detector's response and geometry, which uses GEANT4 [13].

Tertiary beam for the MINERvA Test Beam

The tertiary beam was actually design for the MINERvA first run [14]. Here are shown the beamline details [15]:

- 1. A copper target, used to generate tertiaries from the 16GeV/c secondary beam.
- 2. A steel collimator, for tertiaries which also serves as a dump for the incoming beam.
- 3. Two time-of-flight (TOF) scintillator planes (120ps resolution), for timing and particle identification.
- 4. Four Fenker wire chambers (0.5mm resolution), for angle measurements and tracking.

- 5. Two dipole magnets(10 IV 18), used as a spectrometer for momentum measurement.

This beamline was built in order to reach the low-energy values (0.4GeV to 1GeV as mentioned above). The particles exited the collimator at an angle of 16±1° relative to the incident pions, this angle was chosen according to a Monte Carlo simulation [14,16]. The production of low energy pions and protons is essentially "flat" from 10° to 20°. 16° was a good choice, given the most number of particles coming from the collimator at that angle [16].

The particles composing the beam are quite well separated at a certain momentum range, as shown in figure 1.13. This separation allows the selection of different particles. This was one of the most important results in Test Beam first run.

Momentum, identification and position measurement of each particle was achieved by the use of the TOF system and the four MWPCs. Figure 1.14 shows the arrangement of the tertiary beamline.

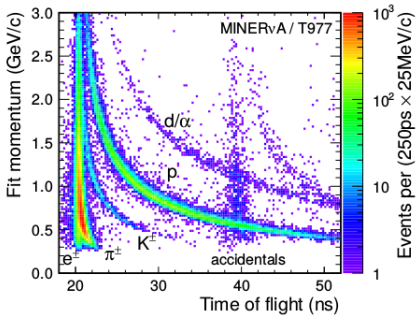

Figure 1.13: TOF versus measured momentum. Here is shown the separation between the different particles composing the beam, as well as the background due to the acceleration time structure (53MHz frequency).

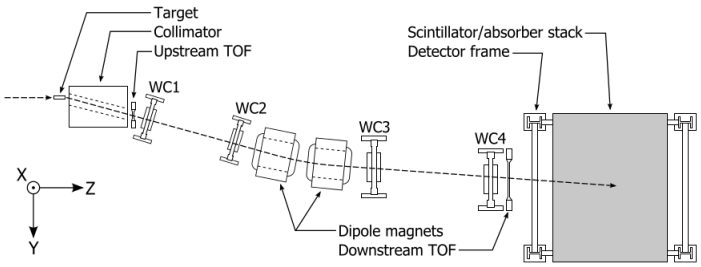

Figure 1.14: Tertiary beam, seen from above (beam going from left).

The path followed by the particles coming from the target was: through the collimator, then two MWPCs and two magnets. The latter had the functions of bending the particle coming from

the collimator, as well as to permit the selection of a particular momentum. The actual bending together with data from the TOF, permitted to characterize the different particles hitting the detector. After the last magnet, particles went through two more MWPCs to help tracking the particles that reached the Test Beam (TB) detector, at last.

DAQ and readout

The Data Acquisition System for the Test Beam, collected data from 16μs gate, just as the MINERvA main detector, there is, though, an essential difference between both. The DAQ for the Test Beam saved data only at the presence of the trigger formed by the coincidence among scintillator counters and the spill signal present at the facility; or due to the cosmic rays trigger used for calibration. A deeper explanation of the Test Beam DAQ system based on the Test Beam trigger is given in appendix A.

Energy calibration

The calibration process was pretty similar to that of the main detector. Through pedestal subtraction and gain measurement using light injection, was possible to have a first estimate of the the photoelectrons yield. Muons going through the detector, helped introducing a correction factor to have an average response for the strips. The absolute energy scale was gotten using a simulation in GEANT4.

Proton calorimetry

When the hadrons interact in the detector, some of their incoming energy is used to unbound nucleus from nuclei. Moreover, some of this initial energy is taken by neutral particles. This way, an estimate of this missing energy was made in order to correct the observed response. The hadron events are reconstructed by summing the calibrated energy measured in the scintillator.

Then the resulting corrected estimate for the energy is compared to the available energy, which is simply the kinetic energy for the incoming proton. The distribution of the response is measured and calculated event-by-event (that is why double occupancy is an issue 1.2.2). Taking the mean for each energy point results in figure 1.15

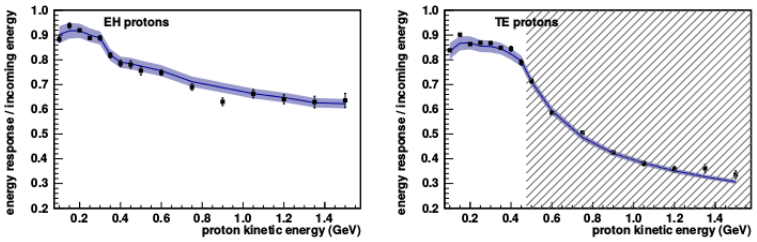

Figure 1.15: Proton response for ECAL/HCAL (left) and for Tracking/ECAL (right).

From figure 1.15, some characteristics of the proton response can be inferred. It is shown that at low energies the missing energy is small, this is because at this energy range, the probability for a proton interacting with a nucleus, is also small. When the protons reach the HCAL and interact with nuclei, start producing Δ resonances. Though the same happens in both configurations, the energy at which it happens is different depending on the configuration. For the ECAL/HCAL configuration is clear that this happens at about 300MeV, and at about 450MeV for the Tracker/ECAL configuration. Then there is more missing energy as the incoming energy increases. The hatched region in the Tracker/ECAL plot, shows the energy region in which there is not full containment of events (charged particles produced in hadronic interactions). The calorimetric response here, is just useful to validate the Monte Carlo (MC) model.

Pion calorimetry

The Tracker/ECAL region is not quite suitable for the containment of pions. In contrast to protons, which have a smaller interaction length [17]. Many pions (about 50%) get to the HCAL calorimeter, before start interacting or showering, but even if they start showering in the ECAL region, certainly, they will deposit just a small fraction of their energy in this region. Actually there is a small probability for pions to go all the way through the HCAL region. Therefore, for the pion analysis just the ECAL/HCAL region was used.

The event selection and the energy measurement were quite similar to those of the proton analysis, but in this case there exists some contamination due to electrons at low energies and kaons at higher ones as shown in figure 1.13, but even making different changes in the selection process, the response is practically the same.

The response for pions is shown in figure 1.16. Here, the errors in data are just statistical, while the Monte Carlo band presents the systematic uncertainties.

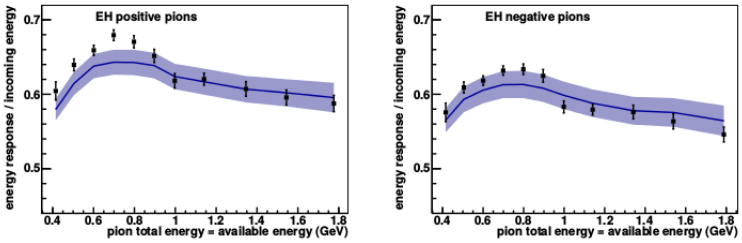

Figure 1.16: Calorimetric response for charged pions.

It can be seen that at about 900MeV there is a smooth change in the response, for which the Monte Carlo calculation does not account. This "change" happens at the same energy level for both positive and negative pions and it has almost the same difference between consecutive points in both cases.

Furthermore, there is a difference between data and MC about the ratio of the π^+ response over the π^- response. Data showed a ratio of 6.2% while MC of just 4.8%.

Electron calorimetry

The electron was meant to perform studies for the ECAL region of the detector. Electrons were only present from 400 to 500MeV. At this same range the electron production was lower than pion production, and at about 700MeV, electron production is negligible.

With the ECAL/HCAL (EH) configuration, electrons (and positrons) deposited around 95% of their energy in the ECAL region. For the Tracker/Ecal (TE) configuration, they went through the Tracker without showering, until they reached the ECAL part. Electrons were separated from pions using a TOF selection (but just at low momenta), see figure 1.13. Events resembling late showering pions and events with a considerable amount of energy deposited in the back part of the detector, were rejected.

Given the narrower range of energies for electrons, compared with those for protons and pions, there is just one value of the response: 0.763±0.013 (statistical) in data and 0.740±0.002 (statistical) in MC. It is important to mention that there were just "49" electron event registered in the EH configuration and "62" more in the TE configuration. The response was 3% higher for the TE configuration, because there were more ionized electrons in the Tracker region before the electromagnetic showers took place in the ECAL.

Systematic uncertainties

These apply for protons, pions and electrons. There are a few sources of uncertainty:

- Beam momentum. This is related with the design of the beamline itself, causing an uncertainty in the x axis of the response (figures 1.15 and 1.16), i.e., the advertised energy of the incoming particles. This has to do, among other things, with the measurement and simulation of the magnet's magnetic field. In the same token, protons at low energies have an extra 0.7% uncertainty due to the higher scattering processes along the beamline.
- Some others like the Birks' parameter [6].
- Temperature stability in which the detector's response to cosmic rays is calibrated against the measured hall temperature as a function of time.
- PMT non-linearity, not significant source of uncertainties for low-energies hadronic showers and tracks, however is a large effect for high activity strips (though, these are rare).
- Events selection, for pions, for instance, there is always a fraction of electrons and kaons, variations in pion selection introduces an extra uncertainty. For protons the selections does not cause a significant uncertainty.
- Crosstalk from electronic and optical devices introduces an uncertainty up until ∼4%.

Adding all contributions here mentioned plus a few more, the total uncertainties obtained for each configuration, are: Tracker/ECAL for protons, 2.7 to 3.3%; HCAL/ECAL for protons, 2.9 to 3.4%; ECAL/HCAL for π^+, 2.6 to 3.4%; ECAL/HCAL for π^-, 2.9 to 3.6%; Tracker/ECAL for electrons, 2.3%; ECAL/HCAL for electrons, 2.6%.

1.2.4 Test Beam detector-second run

Introduction

The second run of the MINERvA Test Beam or Test Beam II, began in the fall of 2014. As much of the goals and primary procedures for the second run are the same than those for the first one, some of the explanations will be omitted.

The Test Beam detector is practically the same, the frame has been practically the same for both runs (it was just repainted and re-enforced for a new heavier configuration), and its dimensions are shown in figure 1.17 (inches [mm]).

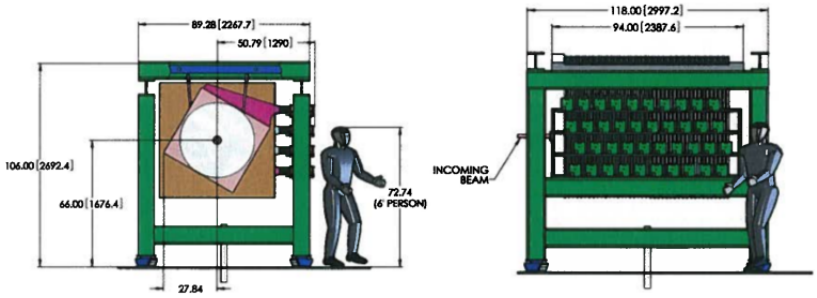

Figure 1.17: Test Beam Detector, run 2.

The main purpose of the second run, is to extend the response plots like in figure 1.16, by making particles to hit the detector with higher energies, up to 8GeV. Therefore, basically, Test Beam II is just an extension in energy (or momentum) of Test Beam I, nevertheless this transition is non-trivial and the instrumentation available in both cases is not the same.

Perhaps the most important difference between runs is the beam itself. Test Beam I used the tertiary beam, while the second run is using the secondary beam at MTest. Due to these unlike beams, there is a different particle composition, for instance in the secondary beam there is a larger sample of electrons, and for example at 1GeV, the percentage of pions in the beam is just a few percent and the electron content is dominant [18], while for the first run (tertiary beam), the electron content was so low (on the order of 10^2 events in total).

The ECAL/HCAL (21 + 21 modules respectively) configuration was used again, which is the ideal configuration for high energy pions, and electrons. This time a new configuration,

called heavy HCAL has been used, which consists in 32 planes of steel, providing a more uniform measurement of the calorimetric response for pions at the highest momenta (more containment of events).

Finally, the configuration with 20 tracker + 21 ECAL planes is used for tracking studies.

Secondary beam for the MINERvA Test Beam

The secondary beam is ideal for the range of energy needed in the second run [10]. Even though the subsystems used in both runs are quite similar, the arrangement is pretty different. This time, the line of the secondary beam got rid of the magnets which are not useful at the new energy levels and not needed to steer the beam given that there is no collimator; the TOF system has a larger distance between the upstream and downstream stations; helium tubes were placed along the line to reduce particle scattering [19]; a Cherenkov counter was used to tag electrons; among a few other smaller changes. The beamline details are best explained in the figure 1.18, where the main components are:

- 1. Downstream Cherenkov counter.
- 2. Upstream TOF station.
- 3. Scintillator counters 1, 2 and 3.
- 4. Fenker MWPCs 1 to 4.
- 5. Veto system.
- 6. Downstream TOF station.
- 7. Cosmic planes.
- 8. Test Beam detector.
- 9. Downstream cosmic plane.
- 10. Scintillator counter 4.
- 11. Helium tubes along the line where possible.

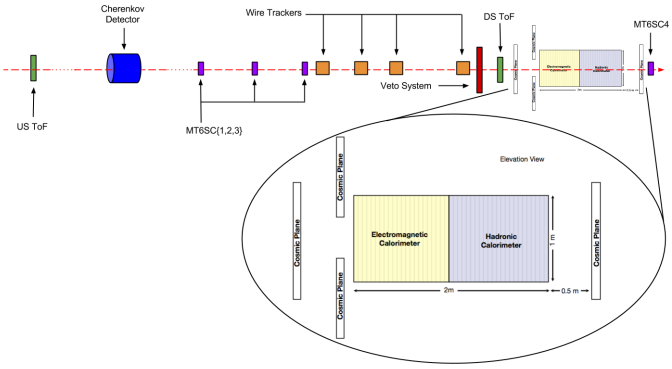

Figure 1.18: Beamline for the second run.

TOF system

The TOF was built specially for the second run. It consists basically in the START and STOP stations, the first one is made of 4 fast (1.3ns) PMTs (5cm diameter), attached to a 5mm thick piece of plastic scintillator (Bicron 400), see figure 1.19. The STOP station, on the other hand, has 2 not-so-fast (3.0ns) PMTs (5cm diameter), both looking at a single 25.4mm thick piece of plastic scintillator (Bicron 404). The scintillator is a 130×130mm square, in order to completely cover the span of the "Fenker" MWPC trackers used.

In general a TOF system is used to get the velocity of the particles traversing a known distance, the velocity can be used to determine either the mass-to-charge ratio of the particles (when their energy is known) or to determine the energy of a known particle.

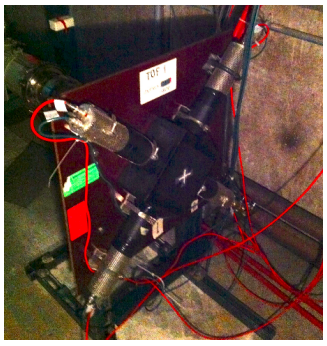

(a) Start TOF station.

(b) Stop TOF station.

Figure 1.19: Time of Flight stations at Mtest.

For the Test Beam, the purpose of the system is to distinguish between the different particle species from which the beam is made of. This is done measuring the time that it takes for a particle

of known momentum to travel between two known locations. This allows to calculate the mass of the particle.

The distance between stations is 104.5m. To measure the time it takes for a particle to traverse this distance, it is necessary to have two time readings, one at each station. In order to do this, the signals from the PMTs are connected to time to digital converter (TDC) modules [20], then the times registered from all the PMTs are averaged, reducing effects of the particle's hit position in the scintillator. When the time in the STOP station is subtracted from the time in the START station, the time of flight for a given particle is gotten, using the following expression:

$$\frac{PMT1 + PMT2 + PMT3 + PMT4}{4} - \frac{PMTL + PMTR}{2} \tag{1.1}$$

a preliminary result is shown in figure 1.20

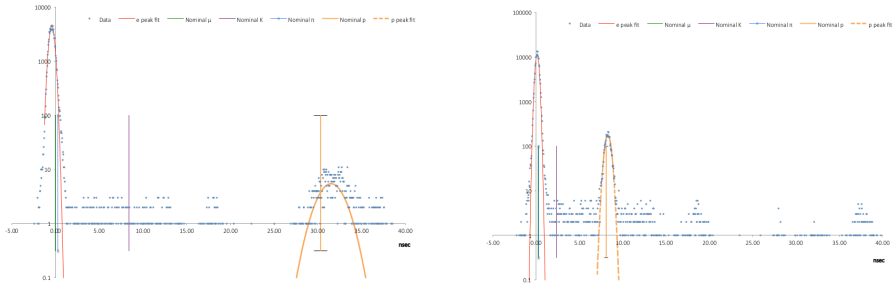

(a) 2GeV beam.

(b) 4GeV beam.

Figure 1.20: Time of flight distributions for electrons and protons at 2 and 4GeV.

In figure 1.20 are shown the distributions for electrons and protons (red and orange lines, respectively) taken from a 2GeV and a 4GeV pion beam. The reason for using 4 PMTs in the upstream station is just for easiness and safeness, given that the station is located in an oxygen deficiency area. In case of a failure in one of the PMTs, data can still be taken with at least two tubes as long as they are in front of each other.

Just about 48% of the events are present in both stations due to scattering of particles in the MT6 area, that is one of the reasons for using the helium pipes. Using these pipes the percentage can be raised up to about 67%. It has to be mentioned that for times in figure 1.20, the distance considered between stations is 82.122m due to a previous placement of the START station, but according to the fits in the same figure, evidently, either the energy was lower or the beamline is longer!

The efficiency for the START and STOP stations were measured as 99% and 93% for a 6GeV pion beam, respectively.

Another very important application of the TOF system is the measurement of the actual beam incoming momentum, as will be shown later, this is one of four methods implemented in Test Beam II for getting the energy of the incoming particles.

Times of flight were taken, and the values gotten so far, for different energy configurations are shown in table 1.1.

	Total	**Within Fit Boundaries**	**Advertised**	**Measured**	**Advertised-Measured**
Config.	Entries	N	Nom. p(GeV)	Meas. p(GeV)	Δ p(GeV)
1.77 Pos Pr	4121	982	2.162±0.059	2.094±0.003	-0.068
2.0 Pos Pr	3805	919	2.392±0.066	2.353±0.003	-0.039
3.0 Pos Pr	2388	437	3.392±0.096	3.254±0.006	-0.138
4.0 Pos Pr	2821	447	4.392±0.126	4.179±0.007	-0.213
6.0 Pos Pr	3764	551	6.392±0.186	5.622±0.009	-0.770
7.0 Pos Pr	8343	1269	7.392±0.216	6.667±0.009	-0.726
8.0 Pos Pr	2809	423	8.392±0.246	7.181±0.015	-1.211
1.77 Neg Pr	0	0	1.378±0.047	0.000±0.000	0.000
2.0 Neg Pr	0	0	1.608±0.054	0.000±0.000	0.000
3.0 Neg Pr	0	0	2.608±0.084	0.000±0.000	0.000
4.0 Neg Pr	988	11	3.608±0.114	3.642±0.055	0.035
6.0 Neg Pr	3583	104	5.608±0.174	5.878±0.029	0.270
7.0 Neg Pr	0	0	6.608±0.204	0.000±0.000	0.000
8.0 Neg Pr	3631	100	7.608±0.234	7.633±0.033	0.026

Table 1.1: TOF data taken so far.

Veto system

The veto system was designed specifically for the Test Beam II, its purpose is to "veto" the multi-particle events and discard them from analysis; and also to veto all the particles not passing through a fiducial area, defined by the MWPC number 4, which is the most downstream in the beamline, and closer to the Test Beam detector.

In section 1.2.2 was already explain that The Accelerator Division (AD) would ideally deliver exactly zero or one particles of known energy per MI bucket. But of course that is not the case. Sometimes they send >1 particle in a single MI bucket. Sometimes they send $\geq$1 particles in adjacent buckets. Sometimes they send one particle, which for one reason or another, causes multiple particles to enter the detector during the same bucket.

For all these cases above, there is not the ability to resolve in time the activity in the Test Beam detector corresponding to separate particles. That is why the veto exists.

The system consists of 12 scintillator counters, each one-tuned for maximum efficiency (>98%). By design, all of the space for approximately 0.5m around the beam axis must be covered by at least two layers of veto counters (figure 1.21).

Vetoing. Wire Chamber number 4 (MWPC4) is a 12.8cm×12.8cm tracking region centered (in theory) on the central value of the beam position in X and in Y. MWPC4 by itself does not cover a wide enough range of angles to handle all cases of two particles originating from the beamline entering the detector.

The veto system is approximately 1m×1m with a 11cm×11cm hole cut out of the middle, centred on MWPC4. It consists of an array of scintillator counters.

The settings of each counter are tuned independently to maximize efficiency, that is how the Test Beam crew vetoes.

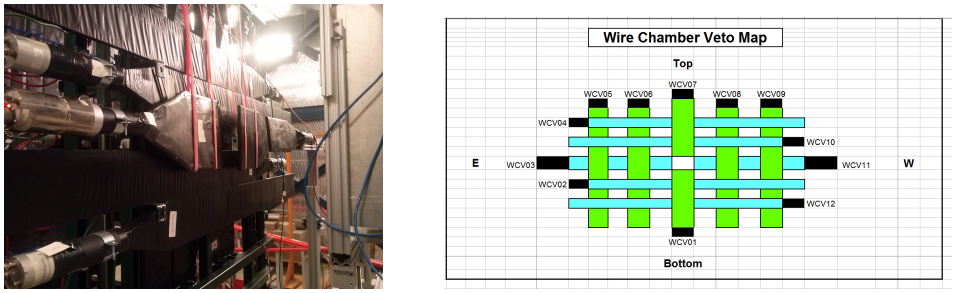

(a) View of the veto paddles.

(b) Veto map.

Figure 1.21: Veto system arrangement.

The veto structure is referred to as a map (figure 1.21), the efficiency for the paddles is related as the ratio between the events in double coincidence and the events in triple coincidence, this is obtained for each counter, as shown in table 1.2

Veto Counter #	Triple Coincidence	Double Coincidence	Raw Efficiency	Rounded Efficiency
1	44630	44881	0.99441	99.4%
2				
3				
4	14628	14676	0.99673	99.7%
5	21810	21854	0.99799	99.8%
6	14501	14591	0.99383	99.4%
7	46982	47205	0.99528	99.5%
8	24915	25043	0.99489	99.5%
9	48331	48647	0.99350	99.4%
10	24335	24360	0.99897	99.9%
11	28237	28292	0.99806	99.8%
12	5916	5925	0.9985	99.9%

Table 1.2: Efficiency of veto paddles.

Timing is needed to define a time window within which a trigger is centred, i.e., a veto signal coincident in real time when the formation of the trigger arrives to a logic module 150ns after the trigger signal. The output of each counter is timed into each other.

The 300ns time is motivated by the ability of the Test Beam detector reconstruction to resolve spatially coincident showers in time. In figure 1.22 can be seen the typical way the system performs. Black line is the spectrum for all the events previous to have been vetoed, the blue spectrum are the events not vetoed, and the red ones the events vetoed. It can also be seen the difference in the percentage of events with more than one particle per bucket by looking at the vetoed events.

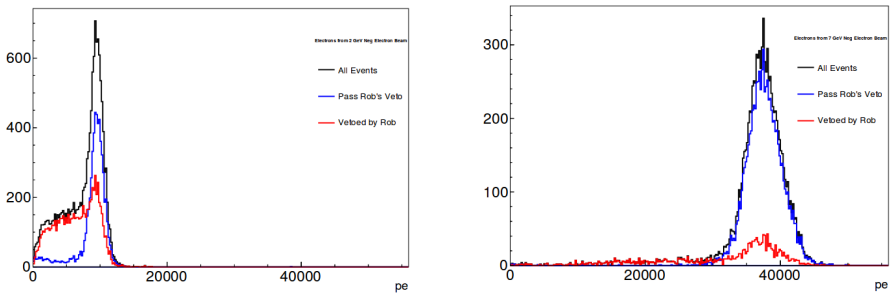

(a) 2GeV vetoed events.

(b) 7GeV vetoed events.

Figure 1.22: Outcome of the veto system.

Tracking system (MWPCs)

The physical principle of operation of the wire chambers is covered in the next chapter, when talking about the instrumentation. Here is explained how the tracking system is used as a whole in the Test Beam second run analysis.

MWPCs are useful in: finding any events that have multiple incoming particles; and in getting the path of incoming particles before they hit the main detector in order to reconstruct the track of these particles.

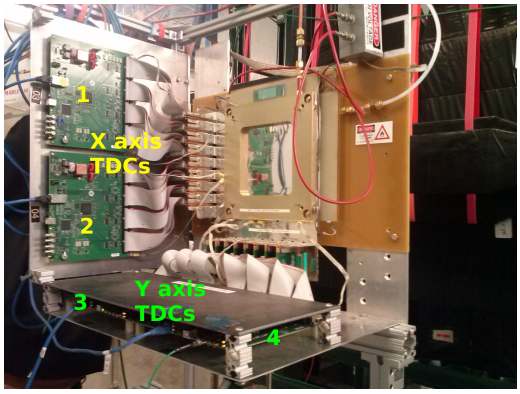

Figure 1.23: MWPC number 4, just upstream the veto paddles.

The way this subsystem works. There are 4 wire chambers, all upstream the Test Beam detector as in figure 1.18. When a particle passes through a chamber, some of its wires send a pulse, indicating the particles passed close to them. All the chambers have two planes, one for each axis (X and Y). The position and distances between chambers is well determined, thus, registering the coordinate in each chamber it is possible to reconstruct the trajectory through which a single particle passed. In this way is possible to reconstruct the pathway of the particles before reaching the TB detector.

The resolution of the chambers is 0.5mm (half of the distance between adjacent wires). The four chambers are readout by 16 TDCs, there are four per chamber (two for each axis), these delivered a reading in nanoseconds, allowing to determine the time at which each event occurred. This time permits to find particles that went through, earlier on. When plotting the time spectrum, two peaks appear, as in figure 1.24:

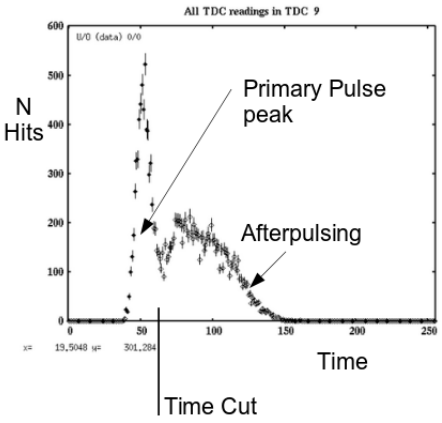

Figure 1.24: Wire chambers time spectrum.

The DAQ delivers a ".dat" file which indicates the hit time in each "excited" channel (wire) for each module (TDC). The hit time of channels (wires) corresponding to the first peak are the ones corresponding to a particle (they are close in time) and hence, only the channels corresponding to the first peak, are chosen. The second peak or bump corresponds to the afterpulsing (electronic garbage) from channels more spread in time. Therefore, when making tracking (position) analysis, these channels are discarded.

The timing cut is not the only one. There is another key cut. It consists on finding the first lit wire, and starting from the closest lit wire to the first hit, there are three options when finding additional wires:

- Add lit wire to hit object if:

  it is 1 wire away from edge of hit, and if:

  it is within 5ns of first hit time (else it is afterpulse or drift [20]).

- If the wire is within 5 wires (but >1 wire) of edge of hit object, then:

  It is afterpulsing or a distant drift of electrons.

- Otherwise, it is a second hit and the event must be marked as having a second particle and must be rejected.

The 5ns are due to the timing resolution, the system cannot tell particles that are less than 5ns apart.

As an extra application, finding the track of a particle can give some help to other subsystems, for instance, the point of the scintillator of the TOF's STOP station at which a particle passed can be found, reducing effects of the particle's hit position for the TOF (section 1.2.4), given that this station is just downstream chamber 4 (figure 1.25).

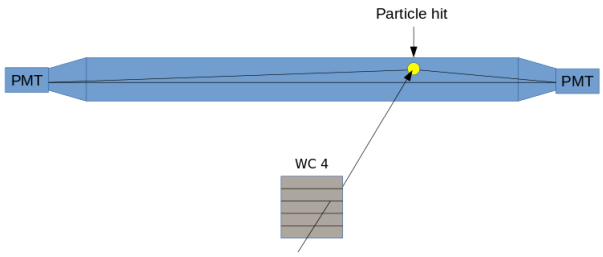

Figure 1.25: Hit point in TOF station, using the tracking system.

Therefore the Tracking system, together with the veto system, are in charge of rejecting events with more than one particle per bucket. Besides that, the tracking system makes possible the reconstruction of the pathway of the particles reaching the TB detector.

Test Beam detector-final configuration

Once all the subsystems were installed, this is how the TB detector looks like in figure 1.26; and in figure 1.27 there is a side view with the ECAL/HCAL configuration.

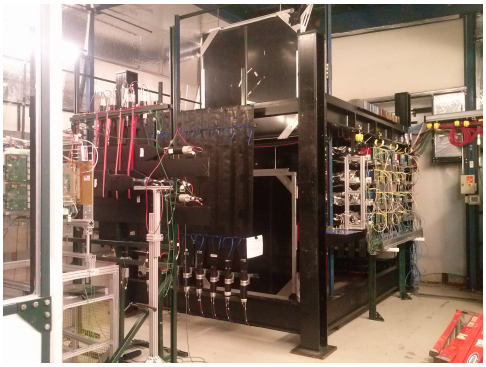

Figure 1.26: Test Beam Detector final ensemble.

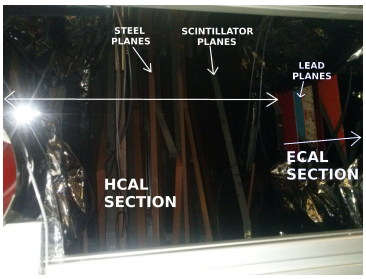

Figure 1.27: Side view showing the ECAL/HCAL configuration.

1.2.5 Beam energy

Beam energy measurements are attempts to get the actual energy of the secondary beam at MTest, which is the beam reaching the TB detector. Getting the absolute energy is a still-in-progress work, where a Monte Carlo based simulation using GEANT4 is being developed for this purpose.

The Test Beam crew launched 4 different ways of approaching this problem, i.e., four measurement methods:

- Time of Flight.
- Electrons in TB detector.
- Hall probes in the beamline.
- Lead-glass calorimetry.

Getting the actual energy would determine the horizontal (advertised) values of the plots in figures 1.15 and 1.16, i.e., the energy of the incoming particles, to within a certain uncertainty.

Accelerator Division (AD) at Fermilab adjusts the current in momentum-selection magnets so that the magnetic field of a probe installed in the magnets stays at a certain value, then they leave the current fixed, that is the way the Main Control Room (MCR) sets the required momentum by MTest in the secondary beamline. There is a crucial question: how fixed is P_{Beam}/I_{Magnet}? Where P_{Beam} is the beam momentum and I_{Magnet} is the current on the magnet.

AD uses an equation in which they set the momentum required by the users, changing the current in the momentum selection magnets. This equation is explained later on.

TOF energy validation

For the case of the TOF system, looking at table reftable1.1, a plot comparing advertised versus measured energy can easily be done, as in figure 1.28:

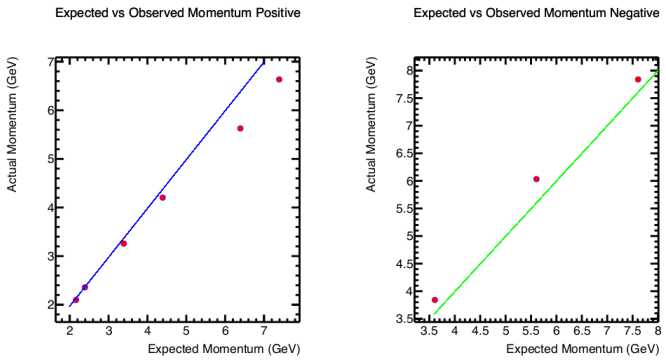

Figure 1.28: TOF energy validation.

For the positive beam, the rage from 0 to 5GeV seems equal to what the probe hall (P_{Hall}) showed, this means that the measured energy is quite similar to the expected energy, at the 3.1%, 1.6%, 4.0% and 4.8% level, for the expected values of: 2.16, 2.39, 3.39 and 4.39GeV, respectively. All these values can be better understood from table 1.1 (and there is a further explanation about these specific values at sections 1.2.5 and 3.5.2).

Electrons in TB detector, energy validation

Electron showers that are well contained in the detector leave $\sim$ 100% of their energy in the detector. Using cosmic running calibration [1], makes possible to get the following spectra for electrons:

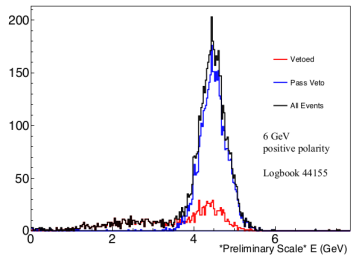

Figure 1.29: Electron spectrum using the TB detector.

From figure 1.29 is clear that measured energy is again not the same as the expected energy. Repeating measurements at 2, 3, 4, 7 and 8GeV, a plot like in figure 1.30 arises:

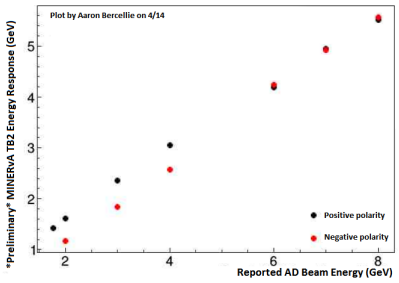

Figure 1.30: TB detector calorimeter energy validation.

As before, there exists a discrepancy between polarities and between the expected and measured values. This time the differences are bigger, around 30%. However, the fit over a straight line has a residual $\sigma(residual) = 2.2\%$.

Hall probes, energy validation

Main Control Room manages a considerable number of beam setting devices, such as "sweeper" magnets, momentum selection collimators, momentum selection magnets and focus quadrupoles. They adjust the current in the magnets so the hall probe has a magnetic field (given in Gauss) needed to send particles of a required momentum.

The way they used to set the magnetic field (previous to lead-glass and TB calorimeter results) was, making use of the "old beam equation":

$$MT4W(Gauss) = +10.96Gauss + (57.92Gauss/GeV)\, P_{BEAM} \tag{1.2}$$

Where: "P_{BEAM}" is the desired beam momentum in GeV, and the units for "MT4W" (the Hall probe) are given in Gauss, which is the magnetic field in the probe. The 57.92 value is from the 120GeV scale, and +10.92 is from the DC offset of the Hall probe in MT4W.

When the studies using the TB detector calorimeter and the lead-glass calorimeter showed up, AD and specifically MCR went to re-measure the offset in equation 1.2. Right after the new offset (the corrected offset) was found to really be "-11.75Gauss". With this, the "new equation" turns out to be:

$$MT4W(Gauss) = -11.75Gauss + (57.92Gauss/GeV)\, P_{BEAM} \tag{1.3}$$

With the new equation, it can be said, retroactively what really the beam energy was. This is summarised in table 1.3:

Request	**Old MT4EH (Gauss)**	**New & corrected "P"**
1.77	113.48±1.00	2.16±(0.06) → (2.8%)
2	126.80±1.00	2.39±(0.06) → (2.7%)
3	184.72±1.00	3.39±(0.08) → (2.4%)
4	242.64±1.00	4.39±(0.10) → (2.2%)
5	300.56±1.00	5.39±(0.12) → (2.1%)
6	358.48±1.00	6.39±(0.13) → (2.1%)
7	416.40±1.00	7.39±(0.15) → (2.1%)
8	474.32±1.00	8.39±(0.17) → (2.1%)
-1.77	-91.56±1.00	-1.38±(0.04) → (3.2%)
-2	-104.88±1.00	-1.61±(0.05) → (2.9
-3	-162.80±1.00	-2.61±(0.06) → (2.4%)
-4	-220.72±1.00	-3.61±(0.08) → (2.3%)
-5	-278.64±1.00	-4.61±(0.10) → (2.2%)
-6	-336.56±1.00	-5.61±(0.12) → (2.1%)
-7	-394.48±1.00	-6.61±(0.14) → (2.1%)
-8	-452.40±1.00	-7.61±(0.16) → (2.1%)

Table 1.3: Summary of the survey looking at both old and new magnets settings.

With this method it can be seen there was a difference as high as ∼20% at the 1.77GeV, for instance.

Lead-Glass, energy validation

The Lead-glass method is the central work of this thesis and is presented in detail in chapters 2 and 3.

Chapter 2

EXPERIMENT - TESTING THE LOW-ENERGY ELECTRON/POSITRON BEAM

2.1 Goals and First Analysis

The main idea of the experiment is to compare the expected or "advertised" energy (by MCR) of the incoming electron/positron beam, against the relative energy measured with a "lead-glass Electromagnetic Calorimeter (EMC)".

Along with the EMC, a "Cherenkov" counter (CC) was used to focus on the following aspects of the electron/positron (e^-/e^+) beam (which is the already expalined secondary beam at low energy) hitting the TB detector. The aim for each of these goals is explained in due time.

- 1. Its linearity, i.e. how much, the advertised energies deviate from an ideal straight line.
- 2. Measured Cherenkov efficiencies.
- 3. Measured differences between positive and negative polarities.
- 4. Consistency of the tuning from the Main Control Room (MCR).
- 5. Measured e^-/e^+ content of the beam using the Cherenkov counter.
- 6. Give an experimental value of the energy resolution.

The MINERvA Test Beam detector in its second era, has been running at the so called medium energy, from 2GeV to 8GeV. To overlap this era with the values taken at the first one, Test Beam II has been taking data at 1.55, 2.0, 4.0, 6.0, 7.0 and 8.0GeV, and for the same reason, the lead-glass detector was run at the same energy levels but the 8-GeV, due to a device constraint explained in the following sections.

2.2 Instrumentation

This section is devoted to explain the functioning principle of the main equipment used during the experiment at MTest. Magnets and other important parts upstream the beamline are not included. FTBF personnel provided the calibration tests and they were the only responsible and authorised to handle equipment such as the MWPCs and the CC. The MINERvA Test Beam folks were in charge of handling from the "counting house", all the electronic devices related to the signals coming from such equipment. The origin of the equipment and devices goes back to the late 70's, then throughout the text, devices such as CAMAC and NIM modules are quite used.

2.2.1 Lead-glass calorimeter

The particles of interest, and under study are electrons and positrons. The idea was to contain all of their energy in a detector, to have an actual measure of the beam energy, and this way get the measurements required in section 2.1. Therefore, given the nature of e^-s and $/e^+$s, the detector required was an electromagnetic calorimeter (EMC). FTBF has 8 EMCs made of lead-glass.

But why lead-glass? At high energies(>100MeV) [21], electrons and positrons lose their energy mainly through bremsstrahlung and subsequent electron/positron showers [22]. High "Z" materials facilitate showers, helping all the energy be absorbed by the detector [22]. Lead-glass is a Cherenkov radiator with Z∼80 [23], given that most of its material is lead oxide ($Z_{PbO} = 90$). Lead-glass is a non-scintillating Cherenkov radiator that detects the Cherenkov light of shower electrons and positrons and has an energy resolution of $\sim 6\%$ for 1GeV electrons and $\sim 3\%$ for 8GeV electrons [20], [24].

The electromagnetic calorimeter search

The blocks were made of lead-glass, and that was everything what was known about them, i.e., there were not data sheets, nor clue about their origin, neither their composition, just the blocks.

The composition of the material is very important, because thereof, experimenters can have an idea of the energy containment and the resolution of the calorimeter [20], [22]. The bigger the energy containment, the better the detector's resolution and the better the energy of the beam can be determined.

In order to know if the available detectors could have a good resolution, it was necessary to know their longitudinal and transverse energy deposition. The standard way of getting the former in a detector is by means of the quantity known as the "Radiation Length (X_0)", where

$$\frac{1}{X_0} = \frac{4\alpha N_A Z\left(Z+1\right) r_e log\left(183 Z^{-1/3}\right)}{A} \tag{2.1}$$

Where α is the fine structure constant, N_A is the Avogadro's constant, Z is the atomic number, and r_e is the classical electron radius.

And the standard way to get the transverse deposition is by the "Molière Radius" of the material [23]:

$$R_M = \frac{X_0 \times 21.2MeV}{E_C} \tag{2.2}$$

Where E_C is the critical energy of the material [22].

According to [25], for any homogeneous electromagnetic calorimeter, at $\sim 20X_0$, the energy fraction escaping out of the back is 2%. And 95% of the total energy is contained in a cylinder of $2R_M$ centred in the axis of the block [26]. So, the procedure taken was to get the radiation lengths and Molière radii for all of the blocks (EMCs) and see how far each detector would be from the ideal values, and finally pick the one that gave the greatest energy containment.

The densities of all the blocks were gotten at MTest, and the blocks densities were matched with different kinds of lead-glass densities found in literature [22], [21], [23]. In table 2.1 appear the measured densities of the EMCs calorimeters, and the highlighted is the one chosen for the experiment due to its length and width, which happened to be lead-glass "SF5" [21], [23], [27].

Label in Calorimeter	**Dimensions (cm)**	**Volume (cm^3)**	Mass (g)	Density (g/cm^3)
Pb Glass block # 1	35.5×14.7×14.7	7671.2	32700	4.04
Pb Glass block # 2	45.0×15.2×15.2	10396.8	43900	4.00
BL-18, RCA	35.2×14.6×14.6	7503.2	31400	4.18
169	35.2×14.9×14.6	7657.4	32200	4.20
BL1, 11-17-99	35.2×14.6×14.6	7503.2	32100	4.27
BL7, PM 59	40.3×10.1×10.1	4111.0	14600	3.55
"Longest block" (no label & broken)	92.7×15.2×15.2	21417.4	70900	3.31
EDR	35.2×14.6×14.6	7503.2	33300	4.43

Table 2.1: FTBF EMCs dimensions and densities.

The SF5 lead-glass calorimeter has the following properties:

- $\rho = 4.0 g/cm^3$
- $X_0 = 2.36 cm$
- $R_M = 4.2 cm$
- $n(indexofrefraction) = 1.67$

So, the block picked ($42.0 \times 15.2 \times 15.2 cm^3$) is $17.8X_0$ long, $3.6R_M$ sideways, and has a composition of $55\%PbO, 38\%SiO_2, 5\%K_2O, 1\%Na_2O$, and an ideal energy resolution of $0.01 + 0.05\sqrt{E\,(GeV)}$ [28]. The results of the measurements will show how far the experimental value is from this prediction.

Based on the above, going forward with this detector seemed pretty feasible and the $17.8X_0$ is not so far from the $20X_0$ required for the 98% longitudinal energy containment ($\sim 90\%$ of this length). However, a mention has to be made about the fact that longitudinal leakage has a "worst" effect in resolution than lateral leakage, according to [29].

In figure 2.1 is the lead-glass detector being prepared and already positioned for data taking:

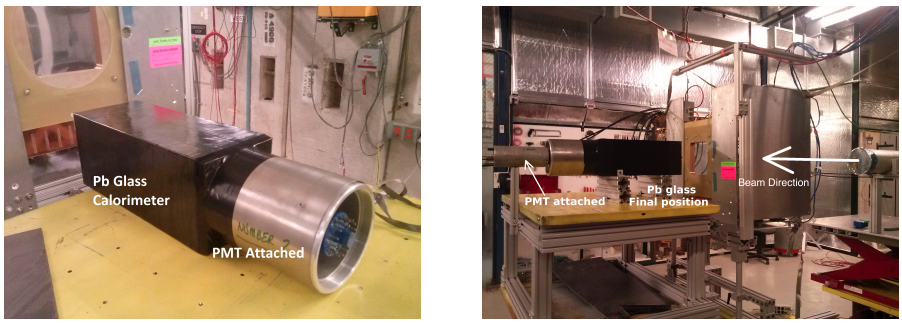

(a) Positioning. (b) Ready for the beam.

Figure 2.1: The lead-glass EMC.

Base and PMT

PMTs are electron-tube devices which convert light into a measurable electric current by means of the photoelectric effect. The basic construction and working principle can be fully understood in [20].

The PMT attached to the EMC is a THORN EMI, type 9791KB, is a 130mm (5") diameter, 14.5cm long photomultiplier with blue-green sensitive (380nm max), bialkali photocathode with enhanced cathode sensitivity, 30 high maximum gain, 7 high typical gain, high stability, quantum efficiency$\sim$ 27%, 9 CsSb dynodes of highly stable and efficient secondary emitting surfaces. Max anode current of 1mA, max HV of 2.2kV [30].

The base is a 14-pin base. Low loss pressed glass base furnished with appropriate high quality Teflon socket. Tubes with "K" suffix (as this) overcapped with diheptal base type B14A. Figure 2.2 shows the base and PMT used [30].

(a) Base (b) PMT attached

Figure 2.2: Base and PMT.

2.2.2 Cherenkov counter

Cherenkov radiation

A charged particle radiates if its velocity is greater than the local phase velocity of light (Cherenkov radiation), i.e., such radiation takes place only in material media. The process is negligible for energy loss (1 to 5% of ionization losses), but it is highly used in high-energy and cosmic-ray physics detectors [21]. Given that the particles are going faster than the light and all electromagnetic waves, the particles leave a cone behind it, due to the retarded emission of the light waves as in figure 2.3. The emission of the Cherenkov radiation is at a well-defined angle. The angle θ_C of the Cherenkov radiation relative to the particle's direction, for a particle with velocity βc in a medium with index of refraction n is

$$\theta_C = arccos\,(1/n\beta) \tag{2.3}$$

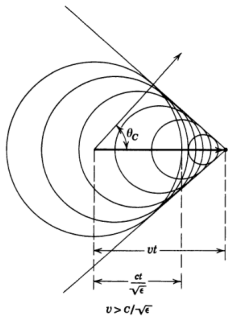

Figure 2.3: Cherenkov radiation profile.

But this is not the only requirement for the particle to radiate. There is also a frequency threshold, below which, no Cherenkov light is emitted: $n\,(\beta) > 1$.

The CC at FTBF

The Cherenkov counter (CC) at FTBF is a Cherenkov threshold detector [31]. The counter head is 2.92m long, is made of aluminum and contains all of the optical elements (mirrors and PMTs). Integral with and upstream of this is a beam tube 15.6m long within which the Cherenkov radiation is produced.

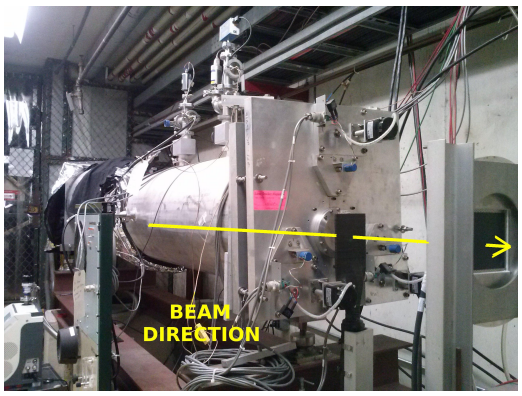

Figure 2.4: Cherenkov Counter at MTest.

All inner surfaces, save for the optical elements, are painted black to reduce unwanted scattered light and to preserve the Cherenkov angle of the retained light (when used as a differential Cherenkov counter). The medium into which Cherenkov light is emitted is a gas, this fills the counter, typically nitrogen. A very important feature of using gas is that the diffraction index of gas radiators may be modified with pressure: $(n-1) = (n_0 - 1)\, p/p_0$, [32], [33].

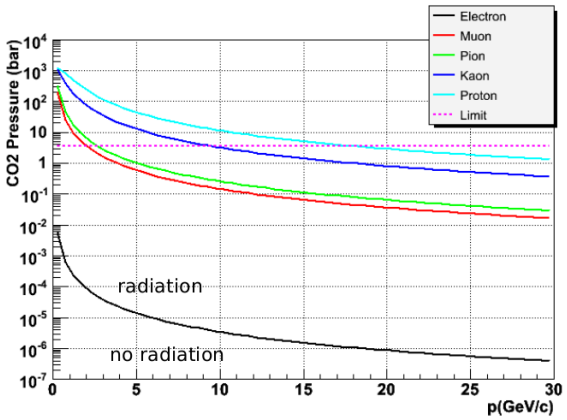

Figure 2.5: Cherenkov radiation dependent on pressure.

Figure 2.5 shows the regions of Cherenkov and no Cherenkov light emission as a function of the gas pressure filling the detector, and the beam momentum. The expression where the pressure threshold can be obtained from, is:

$$p_T = \frac{\frac{1}{\sqrt{1-\frac{m^2}{E^2}}} - 1}{\delta} \tag{2.4}$$

Where $\delta = n - 1$, m is the mass of the incident particle and E its energy [32].

Basically this is the way the CC was operated depending on the energy and the particle to be "tagged", in this case, electrons and positrons at different energies. The detailed procedure is explained in section 2.3.

2.2.3 MWPCs

Multiwire Proportional Chambers (MWPCs) were meant for particle tracking determination. Every MWPC is an array of many closely spaced anode wires, placed in the same chamber, each can act as a single and independent proportional counter [20], [34]. Currently all the wires are read by TDCs (Time-to-Digital Converters), with them, the timing of the signal is also possible along with the positioning of the same, which is related with the positioning of the particle.

The basic MWPC consists of a plane of equally spaced anode wires centered between two cathode planes. Typical wire spacings are $\sim 1mm$.

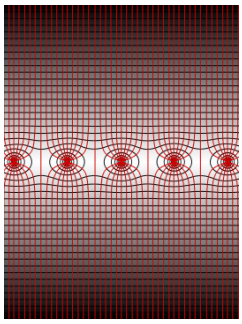

Figure 2.6: Electric field configuration and equipotential lines.

In figure 2.6 is the field configuration of the closely positioned wires, when a negative voltage is applied on the cathode planes. Except for the region very closed to the wires, the field lines are essentially parallel and almost constant, and under the assumption of an infinite anode plane with "zero" diameter wires, the electrostatic potential is then given by

$$U(x,y) = -\frac{CV}{4\pi\epsilon} ln\left[4\left(\sin^2\frac{\pi x}{s} + \sinh^2\frac{\pi y}{s}\right)\right] \tag{2.5}$$

where V is the applied voltage, s the wire spacing, and C, the anode capacitance. If $L \gg s \gg d$, the capacitance is given by

$$C = \frac{2\pi\epsilon}{\frac{\pi L}{s} - ln\frac{\pi d}{s}} \tag{2.6}$$

where L is the anode to cathode gap distance and d is the anode wire diameter. While the assumptions just made are not met in a real chamber, equations 2.5 and 2.6 are good approximations for most purposes.

If electrons and ions are now liberated in the constant field region they will drift along the field lines toward the nearest anode wire and opposing cathode, respectively. Upon reaching the high field region, the electrons are quickly accelerated to produce an avalanche. The positive ions liberated in the multiplication process then induce a negative signal on the anode wire. The neighbouring wires are also affected; however, the signals induced are positive and of small amplitude as shown in figure 2.7.

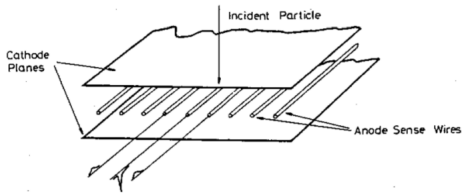

Figure 2.7: The signal on the firing wire is negative whilst on the neighbouring wires, signals are small and positive.

In a similar manner, a positive signal is induced on the cathode. There is thus no ambiguity as to which wire is closest to the ionizing event. The signal from one anode plane, of course, only gives information on one coordinate of the ionizing event. The second coordinate may be obtained by using a second detector whose anode wires are oriented perpendicularly to those of the first. Both planes happen to be in the same chamber in most of the cases. This is the case of the Fenker MWPCs at FTBF.

MWPCs at FTBF

There are 4 “Fenker” MWPC Stations, which consist of an X-plane and Y-plane chambers, and the TDCs to read them out. Each plane has 1mm wire spacing. The aperture is 12.8cm (each plane has 128 wires per plane). Stations are readout using one controller, which can be incorporated into a DAQ system using Ethernet.

The chamber has been designed to minimize the amount of matter in the path of the beam. The windows are made of 0.0005” aluminum foil. The sense wires are 0.0004” gold plated tungsten. The cathode planes are 0.0005” aluminum foil. The chamber half-gap (distance between sense wire

and cathode) is 0.125". In a typical installation, having two sense planes in a module, the material in the beam is 0.025" Al, 0.75" gas and an average of 2×10^{-6} inches of tungsten. This is about 0.002 nuclear collision lengths [22], or 0.007 radiation lengths. In figure 2.8 are the Fenker wire chamber 3 during the alignment stage and the actual composition of the chamber.

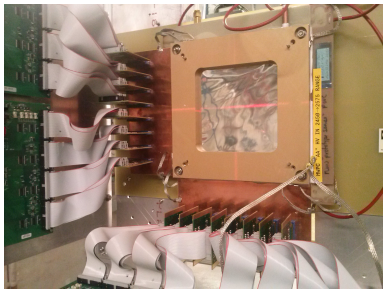

(a) Aligning the wire chamber.

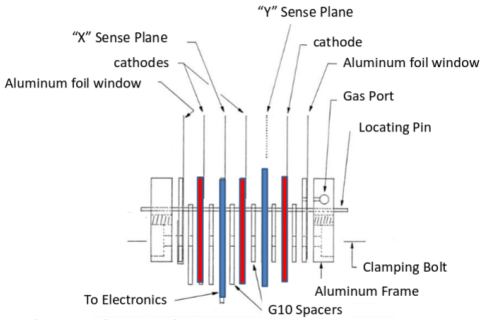

(b) Internal structure of the chambers.

Figure 2.8: Fenker chambers at MTest.

X and Y planes in figure 2.8 were made using 10 microns diameter AuW wire and are installed between three high voltage cathodes made with 12.5 microns aluminum foils. A set of 12 microns aluminum foils complete the assembly.

The gas with which the chambers are filled must fulfil certain requirements, for instance, a very high gain gas mixture ($\sim 10^7$). The one chosen for the Fenker chambers is: $Argon/Isobutane/Methylal$ at 82%/15%/3%, the mixture is the more efficient and stable at high voltages.

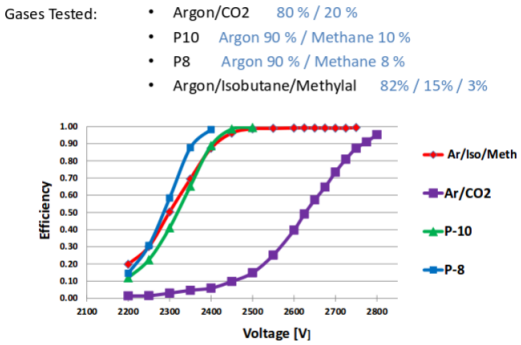

Figure 2.9: Different mixtures of gas for the wire chambers.

MWPCs arrangement

Distances among the chambers are very valuable if trying to determine the "Z" coordinate for particles in the tracking system.

The distance between chambers 2 and 3 is 2.84m (measured by FTBF personnel), and the distance between chamber 3 and the Pb-Glass, 14cm (measured by myself).

2.2.4 Additional equipment

A considerable large number of control electronic devices were used at MTest during the experiment: thermostats for control of the room temperature, light injection modules for PMT gain control, just to mention a few. On the other hand a rather small number of devices at MTest were working in direct contact with the beam at that time. Besides the already mentioned equipment, are the under-appreciated scintillator counters.

MT scintillation counters

Scintillator counters at MTest have the very important task of creating the trigger that is, the coincidence signal that tags an event as a valid event. This is done relatively simple, using three of this scintillator counters (SC) put in logic coincidence with the "SPILL" signal (signal indicating the presence of beam delivered by MCR) as in figure 2.10.

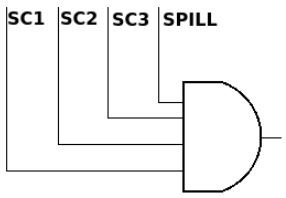

(a) Signals from SC1, SC2, SC3 and the SPILL put in "&" logic coincidence.

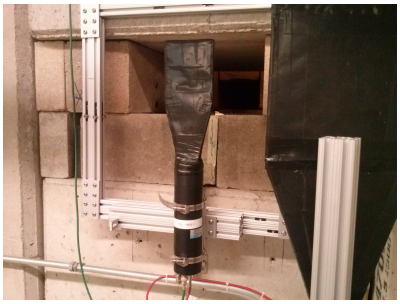

(b) SC3 at the entrance of enclosure MT6.2

Figure 2.10: Trigger logic and SC3.

MT6SC1. Located immediately downbeam of the Cherenkov detector at the entrance to the MT6.1 enclosure (downbeam of the TOF1 detectors). Scintillator is $10cm^2$ and 1/4 inch thick. PMT is a Hammamatsu (no model found).
MT6SC2. Located immediately upbeam of the absorber at the exit to the MT6.1 enclosure. This SC can be slid out of the beam in case particle scattering needs to be reduced. Scintillator is $10cm^2$ and 1/4 inch thick. PMT is a Hammamatsu (model not found).
MT6SC3. Located at the entrance to the MT6.2 enclosure. This SC can be slid out of the beam in case particle scattering needs to be reduced, or helium tubes are being used. Scintillator is 10cm2 and 1/4 inch thick. PMT is a Hammamatsu (model not found).

Helium tubes

A make-shift beamline was installed and filled with helium gas to reduce beam scattering in air. Scattering is a big problem when trying to reach the desired number of events in a short time. Helium is a less dispersive medium than nitrogen and oxygen which fill the room [19]. The procedure consisted in placing the biggest possible number of 4"-diameter tubes filled with helium gas to reduce scattering as much as possible and this way reducing the time for data taking.

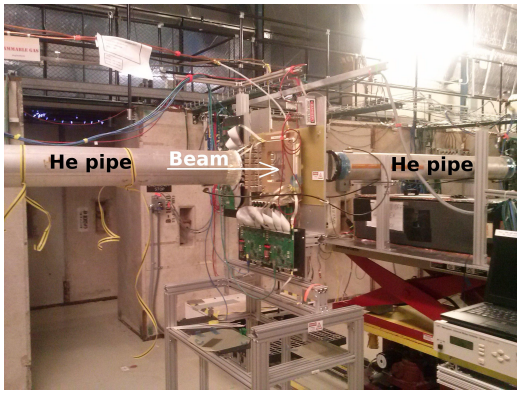

Figure 2.11: Helium pipes along the beamline in enclosure MT6.2.

A few more

One FLUKE 415B HV Power Supply 3 KV, 30 mA and one ES-7092 HV zener divider to provide HV for the PMT; and a Lecroy 428F linear Fan-Out module was also needed for signal distribution and diagnostics.

2.3 Data Taking

Once all the involved equipment has been introduced, the detailed procedure followed to take data will be explained. The schedule at MTest is pretty complicated and available times to make use of the beam are really demanded. All lead-glass data was taken at night hours, holidays or weekends. Therefore, previous to perform the definitive runs, some previous runs were taken in order to test the quality of the signals and prove the programs and macros developed to such a task.

2.3.1 Setup

The setting up of the experiment began with the placement of the equipment along the beamline by the MTest crew. Wire chambers had not been recently calibrated. The last calibration was in 2012, where efficiencies were over 97%, though a more recent "partial" analysis shows the efficiency

$\sim 90\%$ [35]. What was done recently was to look at the profiles and this confirmed that MWPC1 was not working properly (which can be seen at section 3.3), also by the MTest crew. 4 helium pipes were put in position and filled with this gas. The lead-glass calorimeter was taken out from the warehouse and aligned and secured in a movable table for its remote control, given that it had to be removed for other experiments. Signal and HV cables (LEMO cables and connectors [36]) where tested for continuity with a pocket pulsometer [37], and the HV cable, as well for insulation with a "megohmmeter" (50MΩ, high resistance). The PMT's HV was chosen as 1150V due to it was the value that minimized the electronic noise from the output signal, and allowed the separation of signals (shown later) and the overflow due to ADC constraints (also explained below, both at section 3.1).

Trigger and signal integration

The trigger previously mentioned (SC1 && SC2 && SC3 && SPILL) was put in coincidence in a "logic coincidence unit" LRS 365AL LeCroy (NIM module) at the electronic house. The logic signal coming from it, was "fanned-out" to two 821 quad. LeCroy discriminators (NIM modules). The output of one discriminator was set to 60ns and the other one to 360ns. These two outputs fed two LRS 2249W, 12-channel, 11-bit, LeCroy analog-to-digital converters (ADCs) [37].

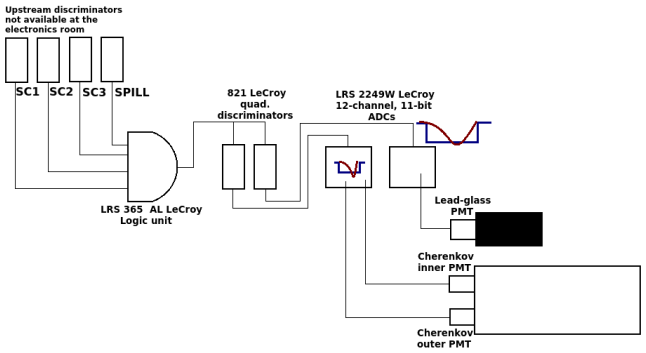

Figure 2.12: Logic circuit for the acceptance of events.

In figure 2.12, the "red" signal is the analogue signal coming from the PMTs, while the "blue" signal is the integration gate.

During the first beam request, the electric signals coming from the Cherenkov and lead-glass PMTs were seen at the oscilloscope, their times determined the above 60ns and 360ns gates respectively. Every time the logic unit recorded a valid event, a dual gate generator unit, sent a veto signal to prevent the ADC reading out another event at the same time, this veto signal was $10\mu s$ long, according with the readout time of the ADC [37]. The PMTs signals and the gates had to be put in time by means of delay boxes and extra delay cables.

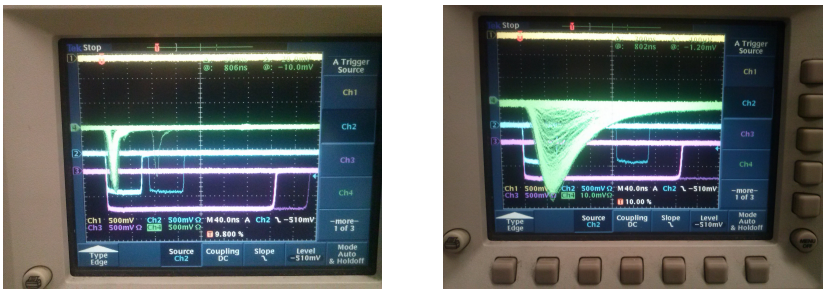

(a) Cherenkov signal.

(b) Lead-glass signal.

Figure 2.13: ADC gates, Cherenkov and lead-glass signals as seen in the scope.

The signals as shown on the scope, were what they were expected to be. With both signals reaching the ADCs at the same time and within the corresponding gates, each signal could be integrated during the time the gates stayed open.

MWPCs have a separate Data Acquisition System (DAQ), they have the same trigger but from another cabling. Overall, one of the most important features to look at, is the timing of the signals, in figure 2.14 is shown the timing of the four chambers, even though, as already mentioned, MWPC1 was very noisy, and MWPC4 was downstream of the calorimeter, and a considerable reduced number of events were seen from it.

One of the most important aspects of the run to take care of, was that both DAQs had the same number of triggers (explained below).

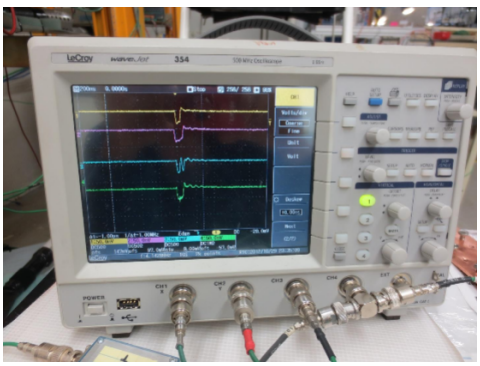

Figure 2.14: Timing of the wire chambers signals.

The wire chambers as well as the lead-glass and Cherenkov signals reach a computer at the control room at MTest through a CAMAC controller.

Final arrangement

With all of the checks for the devices and equipment, the way the experimental arrangement was set finally is shown in figure 2.15. This configuration shows how exactly all the equipment was at the time of data taking.

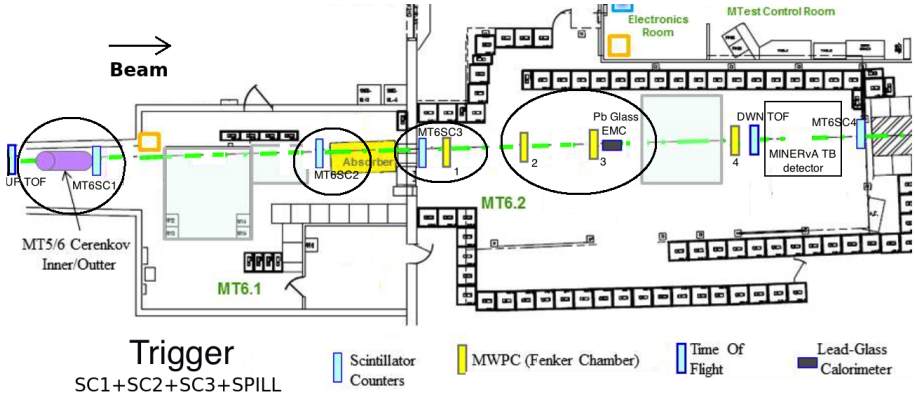

Figure 2.15: Final experimental arrangement.

2.3.2 Procedure

The standard procedure was rather simple, once all had been checked to work properly, it consisted in the following steps. Everything was recorded in the MINERvA electronic logbook [38], where all of the details related with the runs, are.

Cherenkov pressure

Before asking for beam, the Cherenkov pressure had to be validated using the iFIX Cherenkov pressure control console (figure 2.16). To set the pressure one has to look at the spreadsheet at the FTBF website to chose the pressure value for the particle and energy desired, which is done using equation 2.4 [39]. In our experiment the pressure of the nitrogen filling the detector was maintained at 2psia all the time, given that at that value, only electrons and positrons are supposed to make the detector to fire.

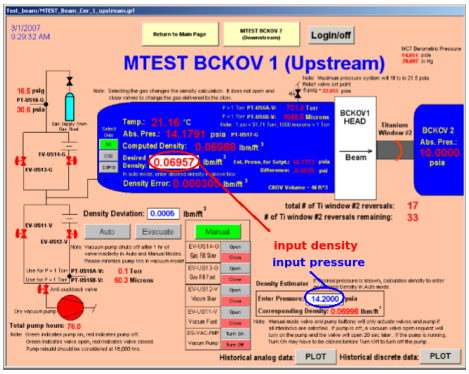

Figure 2.16: iFIX console to set the Cherenkov pressure.

The user enters a density in the "desired density" input box. The density units are pounds per cubic foot and the computer calculates density, based on the ideal gas law with temperature and pressure instrumentation inputs. The system will then open gas input or vacuum valves and turn on the vacuum pump if necessary to reach the set point. If the desired pressure is known, the "density estimator" can calculate a density based on the pressure typed into the "enter pressure" data entry box. The "corresponding density" can then be entered into the "desired density" data entry box. The system computes density based on the pressure reported by the PT-US17-G sensor for the upstream Cherenkov counter (not used during this test) and PT-DS7-G for the downstream CC, and the temperatures reported by upstream RTD TE-US-17-G and downstream RTD TE-DS-7-G sensors. For nitrogen, the acceptable range of density input is 0.0005 to 0.100 lb/ft^3.

Asking for the beam

Calling Main Control Room (MCR) to ask for the required beam characteristics was the first step during the runs.

If all the machinery was working good, MCR set us up. Then looking at the screen at the so called "channel 13" and seeing if there was actually beam, was next (figure 2.17). If the value of ppp (protons per pulse) is at 10^7 or lower, it means that there is actually no beam being delivered to MTest.

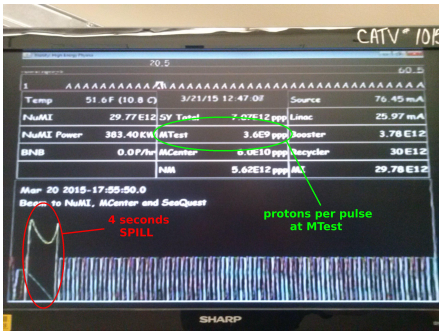

Figure 2.17: Verification of beam being delivered at MTest channel 13.

Running the programs

When the beam was reaching the EMC detector, at the assigned FTBF Linux computer, the two programs for both DAQ systems where open. The beam is present only during 4 seconds every minute, the 4-second SPILL time, right after the SPILL had passed, both programs were started (one right after the other), and a few lines were written related with the file names. When the beam came back in the next SPILL, both programs were already running. After the first SPILL the same number of triggers had to be registered in both programs, indicating that all the particles inside the lead-glass EMC, had also passed through the MWPCs window, and of course that always happened.

When done for the number of events required, both programs were stopped and the info was automatically saved in the computer.

2.3.3 Runs

There were 5 energy levels at which electrons and positrons were tested: 1.55, 2.0, 4.0, 6.0 and 7.0GeV, the original idea was to work at 8.0 instead of 7.0GeV, but the ADC modules available presented overflow at that energy, and the spectrum was not well defined. At each run the beam had the following characteristics (as presented in the logbook):

- Beam type: Pion (that is the way MCR call the secondary beam).
- Energy: One of the above.
- Intensity: 10000 counts (number of required particles per event).
- Beam polarity: e^-s or e^+s.
- Lead-glass in the beamline: of course.
- MT4PB: Out (Lead sheet to stop electrons).

- PbGlass at 1150V.
- Cherenkov at 2psia.

In figure 2.18 there is one of the usual entries, in this case for run number 022.


42921 03/22/2015 11:43:12 **TestBeam_2**

Alejandro Ramirez

Form:	**TestBeam_2/Start_Run_Series**
Run number:	Pb022
Run Mode:	Other (use comment field)
Beam Type:	Pion
Energy (GeV):	1.55GeV
Intetnsity (counts):	10000
Beam Polarity:	Positive
HW config:	HV Off
Lead Glass:	Yes
Detector config:	Other (use comment field)
Run Started:	manual
Comments:	MT4PB Out PbGlass at 1150V Ckov at 2psia

Comments:

Alejandro Ramirez (maramire) 03/22/2015 12:05:18
Ran from 11:42 to 12:04

Figure 2.18: Entry in the MINERvA logbook for run 022.

Besides, there were only two runs for each energy level, for each polarity (e^-s and e^+s), plus a few training runs, summarizing a total of 56 runs.

As can be seen from the run, it took about 20 minutes to reach the desired number of events, plus around 10 minutes making and performing a quick analysis of the plots, plus about 15 more minutes for MCR to change the energy and sometimes like half an hour if a change in polarity was required. Hence, it took like 1 hour to 80 minutes to reach 10000 events into the lead-glass. And it took longer for the lowest energies due to the more scattering present.

The time lapses available to run were 6 to 7 hours long, and 10000 events was the reasonable biggest number to achieve for the five energy levels within that available time.

2.3.4 Programs, macros and DAQ

Two parallel data acquisition systems were used, one for reading out the ADCs registering the signal from the calorimeter and Cherenkov counter (CAMAC readout) and the second one to readout the wire chambers (Wire chambers readout). Both use relative easy programs. The first one uses a LeCroy program written in C ("lecroy.C" by W. Badgett) and for the wire chambers there is a program written in python ("daq-mtest.py" by G. Savage).

For this experiment a special trigger was used (CAMAC & MWPC trigger) which comes from the coincidence of the scintillator counters SC1, SC2, SC3 and the Spill signal. The interface between all the electronic modules and the computer is the CAMAC crate.

Chapter 3

ANALYSIS AND RESULTS

3.1 Raw Spectra

This chapter is devoted to the exposure and analysis of the results from the runs of the previous chapter. Raw spectra are the signals as come from detectors, without any modification or treatment. Through the correlation among each other, valuable information can be extracted about the characteristics of the beam.

3.1.1 Lead-glass spectra

Lead-glass spectra are the means through which the relative energy of the electron/positron beam is obtained. As shown right away, the spectra have a lot of inherent and hidden information that can be extracted thereof by means of the data analysis. However, not just electrons and positrons can get through the calorimeter.

positrons

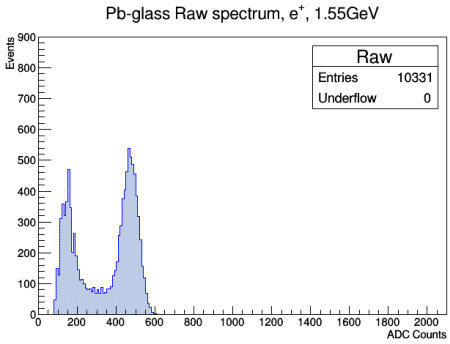

(a) e^+ 1.55GeV

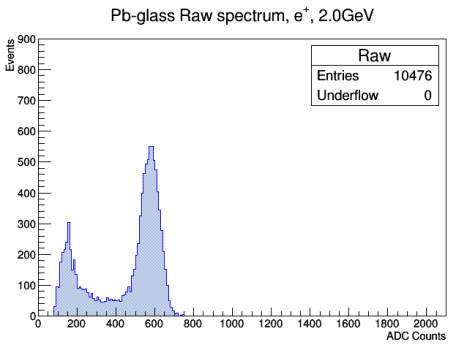

(b) e^+ 2.0GeV

Figure 3.1: Lead-glass raw spectra for positrons, 1.55 and 2.0GeV.

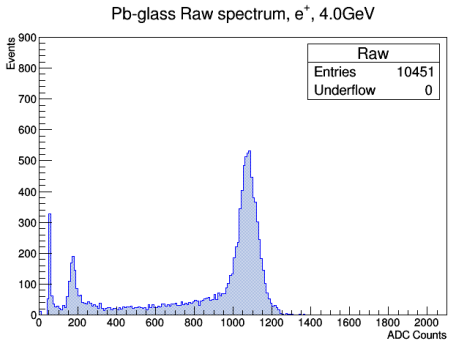

(a) e^+ 4.0GeV

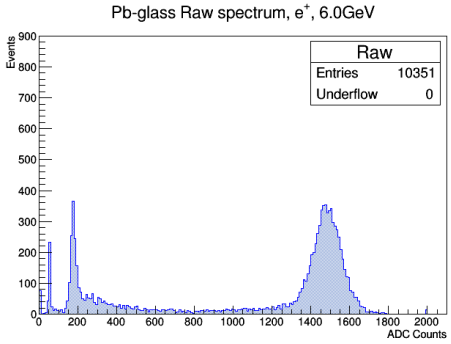

(b) e^+ 6.0GeV

Figure 3.2: Lead-glass raw spectra for positrons, 4.0 and 6.0GeV.

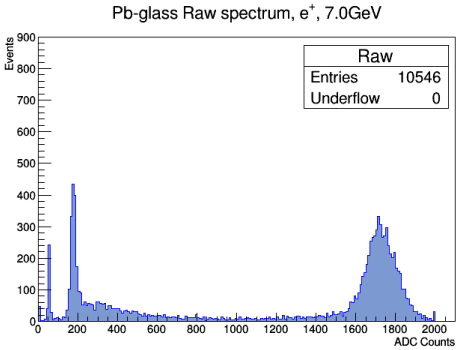

Figure 3.3: Lead-glass raw spectrum for 7GeV positrons.

According to MCR and [40], the beam composition is basically, electrons (e^+/e^-), pions, muons and very few kaons and protons. The 1.55GeV and 2.0GeV raw spectra show two different peaks as in figure 3.1; while spectra at 4.0, 6.0 and 7.0GeV have three as in figure 3.2. The rightmost peak corresponds to the electron/positron energy deposition. The middle peak corresponds to pions and mouns energy deposition, while the remainder peak (leftmost peak) to pedestals (DC level on which the electronic signal seems to be mounted) [20]. Identification of the peaks is possible due to the energy that each of these particles deposit in an electromagnetic calorimeter. As it is well known, a muon is a minimum ionizing particle ("mip"), thus the particles with less energy loss at the spectra, are muons, their energy deposition is almost constant [41]. As hadrons (mesons), the pions loss energy is described by terms of the interaction lengths, these are larger than radiation lengths [42]. Thus, pions would need a deeper sample of the same material to deposit an energy closer to their incoming energy. Therefore, given that one of the main characteristics of the beam is that all of its particles, no matter what, have the same energy, it is understood which of these peaks correspond to each kind of particle. An electron (or positron) due to electromagnetic showers deposits almost all of its energy, while pions and muons a smaller quantity of their energy.

The reason why there are just two peaks at 1.55 and 2.0GeV is that the ADC module (LeCroy LRS 10-bit 12-channel ADC [37]) used at these smaller energies, presented almost a negligible amount of pedestals. At these energies (and just for the positive runs) was possible to use them, because at these energy levels there is no overflow, that in this case, are events with counts above 1024 (10-bit ADC). As the energy goes up, an ADC with more bits is needed.

It would have been nice to have the peaks for mouns and pions as clear as the electron/proton peaks, nevertheless this is of little importance, because the information required comes just from the electron/positron component of the beam insomuch as the calorimeter used is an electromagnetic calorimeter.

The events between the rightmost and the middle peaks are particles that could not cross a considerable fraction of the block's length and therefore leaving a small amount of energy into the detector, most of them electrons/positrons and negative/positive pions.

electrons

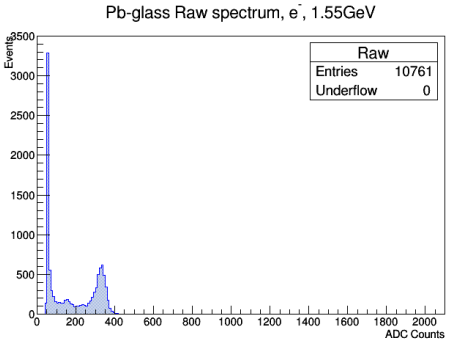

(a) e^- 1.55GeV

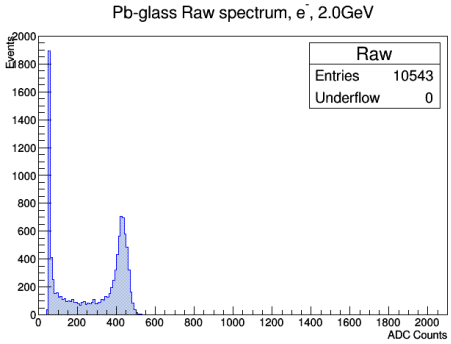

(b) e^- 2.0GeV

Figure 3.4: Lead-glass raw spectra for electrons, 1.55 and 2.0GeV.

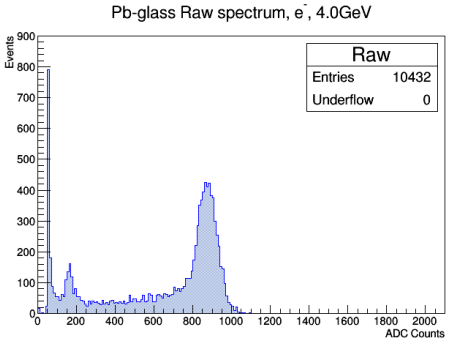

(a) e^- 4.0GeV

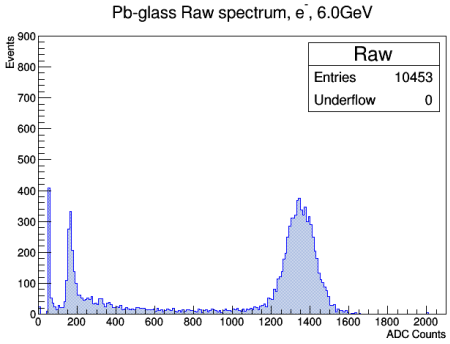

(b) e^- 6.0GeV

Figure 3.5: Lead-glass raw spectra for electrons, 4 and 6.0GeV.

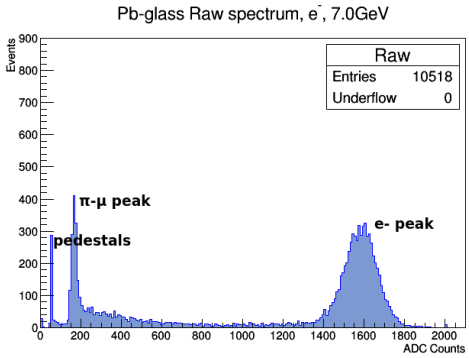

Figure 3.6: Lead-glass raw spectrum for 7GeV electrons.

When doing the analysis for electrons is clear that the muon/pion content is considerably larger at 1.55 and 2.0GeV energies. These is how the beam is at these energies for negative polarities. Later on in this chapter the comparison between polarities is treated with more detailed.

3.1.2 Cherenkov spectra

Although for the experiment, the ideal Cherenkov detector would emit a signal if and only if an electron or a positron pass through it, overcoming the pressure threshold for the Cherenkov light, the reality is not that easy. Actually almost all the electrons and positrons crossing the Cherenkov Counter (CC), made it to "fire", but unfortunately some of the pions and muons made it to fire as well. This issue was worse at lower energies (section 3.2).

The CC spectra showed a spread distribution, this is due to the spread of the beam and due to the not perfect inner surfaces of the detector, then not all photons reach the inner and outer PMTs.

Cherenkov spectra from e^+s

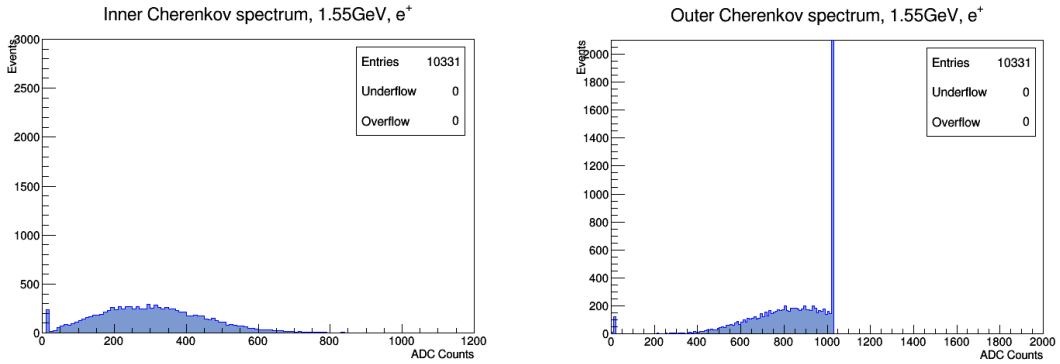

(a) e^+ 1.55GeV inner PMT

(b) e^+ 1.55GeV outer PMT

Figure 3.7: Cherenkov raw spectra for positrons, 1.55GeV.

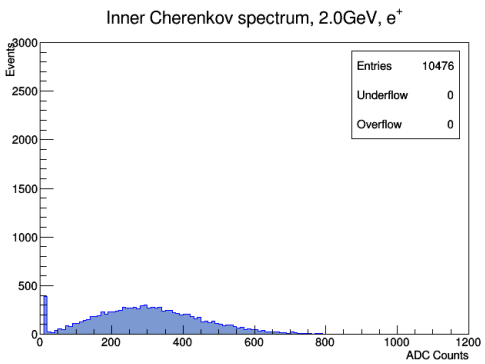

(a) e^+ 2.0GeV inner PMT

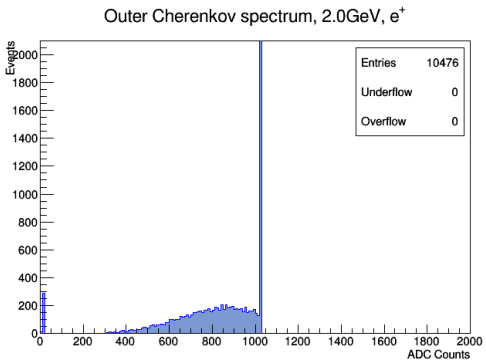

(b) e^+ 2.0GeV outer PMT

Figure 3.8: Cherenkov raw spectra for positrons, 2.0GeV.

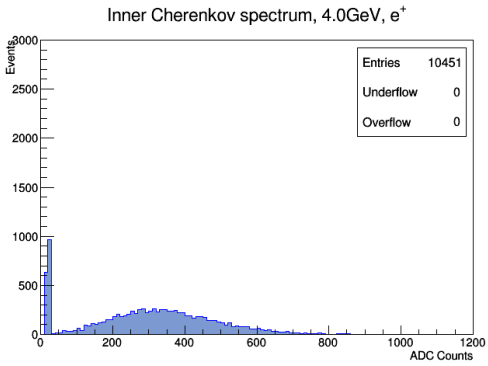

(a) e^+ 4.0GeV inner PMT

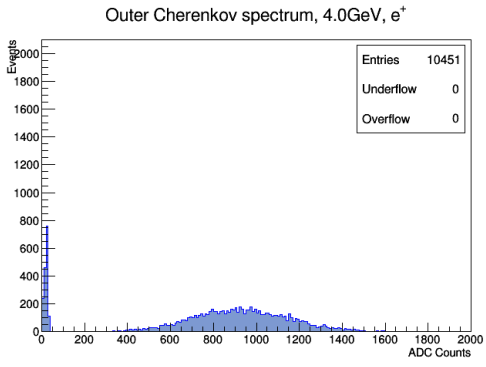

(b) e^+ 4.0GeV outer PMT

Figure 3.9: Cherenkov raw spectra for positrons, 4.0GeV.

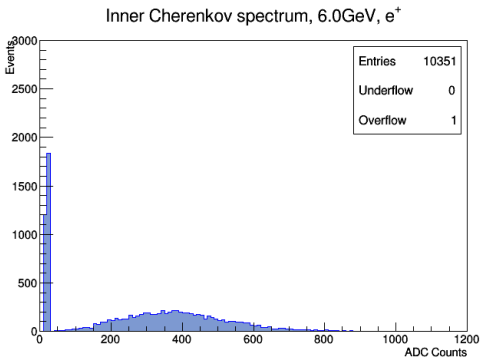

(a) e^+ 6.0GeV inner PMT

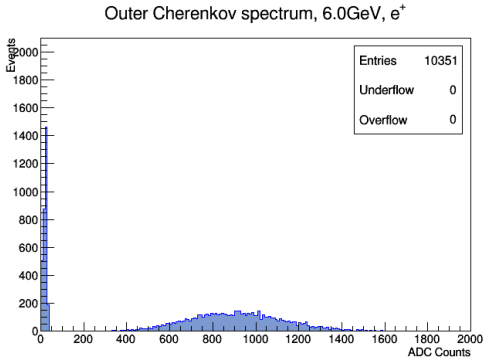

(b) e^+ 6.0GeV outer PMT

Figure 3.10: Cherenkov raw spectra for positrons, 6.0GeV.

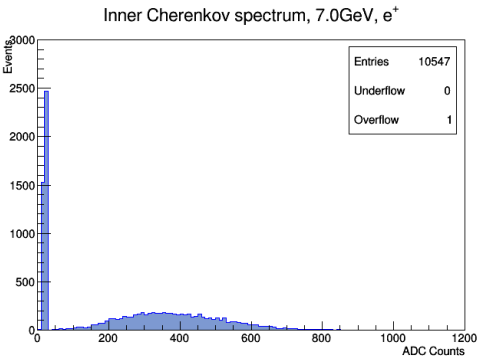

(a) e^+ 7.0GeV inner PMT

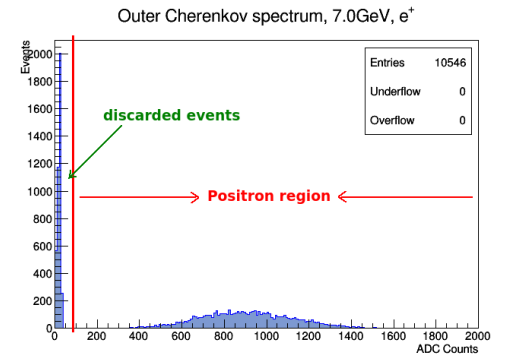

(b) e^+ 7.0GeV outer PMT

Figure 3.11: Cherenkov raw spectra for positrons, 7.0GeV.

Cherenkov spectra from e^-s

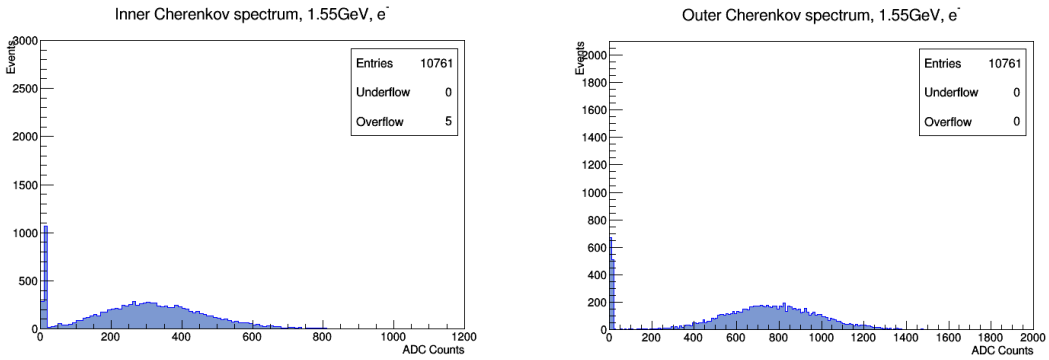

(a) e^- 1.55GeV inner PMT (b) e^- 1.55GeV outer PMT

Figure 3.12: Cherenkov raw spectra for electrons, 1.55GeV.

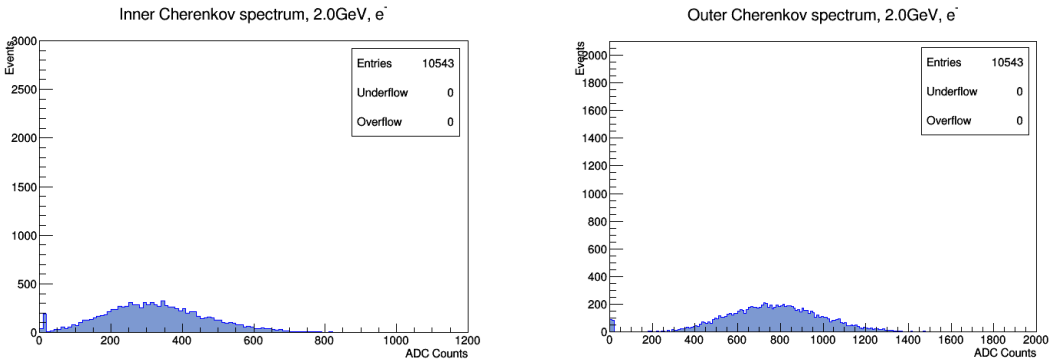

(a) e^- 2.0GeV inner PMT (b) e^- 2.0GeV outer PMT

Figure 3.13: Cherenkov raw spectra for electrons, 2.0GeV.

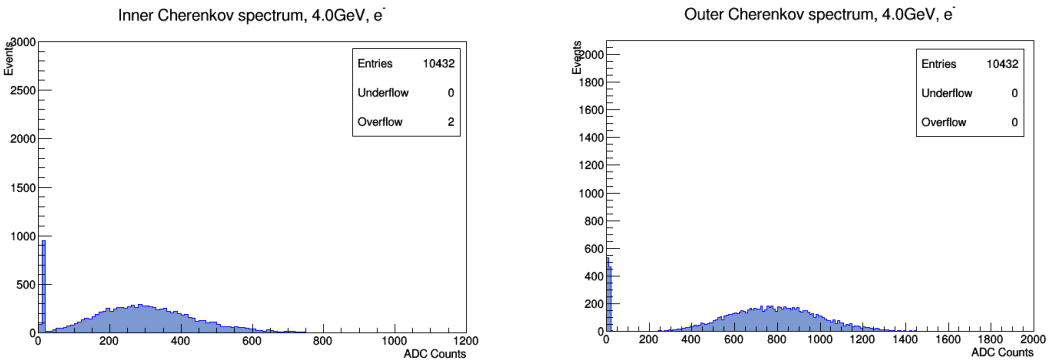

(a) e^- 4.0GeV inner PMT

(b) e^- 4.0GeV outer PMT

Figure 3.14: Cherenkov raw spectra for electrons, 4.0GeV.

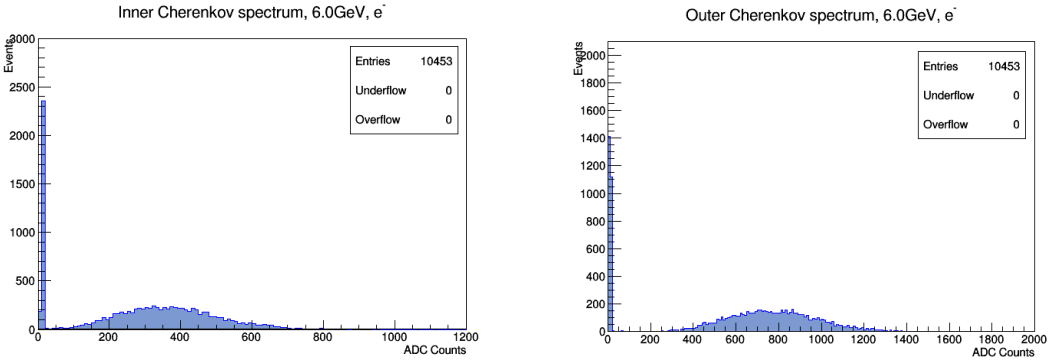

(a) e^- 6.0GeV inner PMT

(b) e^- 6.0GeV outer PMT

Figure 3.15: Cherenkov raw spectra for electrons, 6.0GeV.

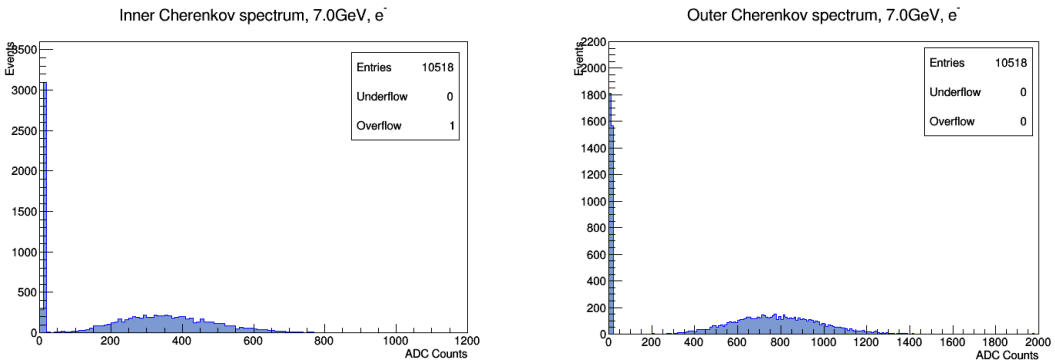

(a) e^- 7.0GeV inner PMT

(b) e^- 7.0GeV outer PMT

Figure 3.16: Cherenkov raw spectra for electrons, 7.0GeV.

These spectra show the events "tagged" as electrons or positrons, figure 3.11, the region of "discarded events" corresponds to the pedestals which help to visualize the non-electron/positron events. The overflow appearing in plots such as in figure 3.8 is due to the ADC available at that time (a 10-bit, 12-channel LeCroy, LRS 2249A module [37], 1024 maximum number of counts). However this does not matter at all, for the purposes to which the Cherenkov spectra were meant, they were meant to tell whether an event "is or is not" an electron or a positron, then if some events appear stacked at the upper bit of the histogram, they are known to be either electrons or positrons.

There are two PMTs in the CC, this is because the detector can be used as a differential or imaging Cherenkov counter as well [43]. Then, these two PMTs are meant to catch the light at a certain angle (when used as a differential or imaging CC).

3.2 Cherenkov Cuts

Is here where the threshold Cherenkov counter exposes its usefulness. It was explained in the previous chapter, that for a given particle of mass m and incoming energy E, there is a pressure threshold above which, the particle begins to emit a Cherenkov glow. Applying cuts to the lead-glass raw spectra, leaving only the events that were selected to be electrons or positrons, new spectra are obtained without all the discarded events.

Then, the "new" electron/positron spectrum for each energy and for each polarity can be further analysed to get the required information regarding these two kind of leptons.

3.2.1 Cherenkov cuts for positrons

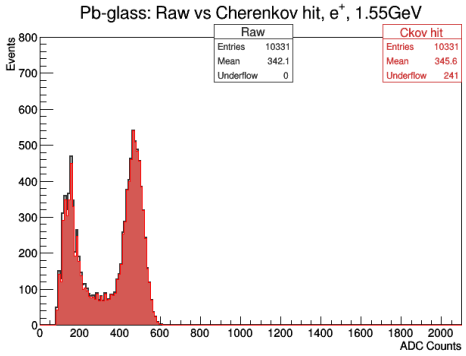

(a) e^+ 1.55GeV

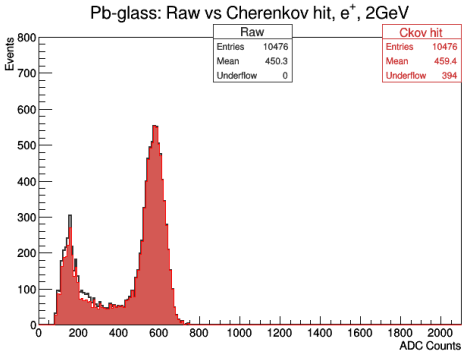

(b) e^+ 2.0GeV

Figure 3.17: Cherenkov cuts for positrons, 1.55 and 2.0GeV.

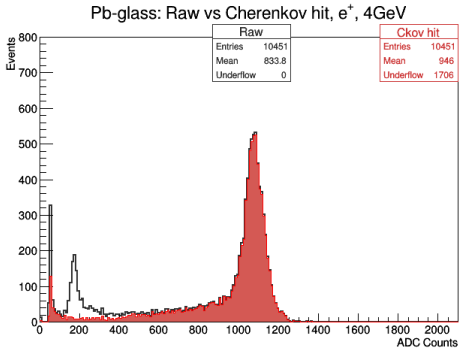

(a) e^+ 4.0GeV

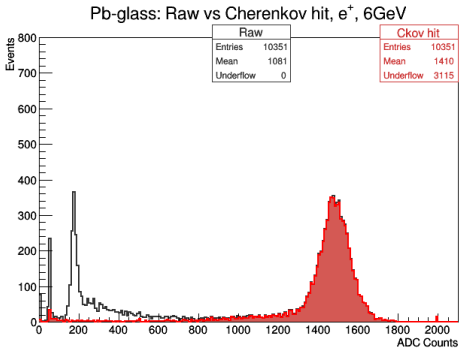

(b) e^+ 6.0GeV

Figure 3.18: Cherenkov cuts for positrons, 4 and 6.0GeV.

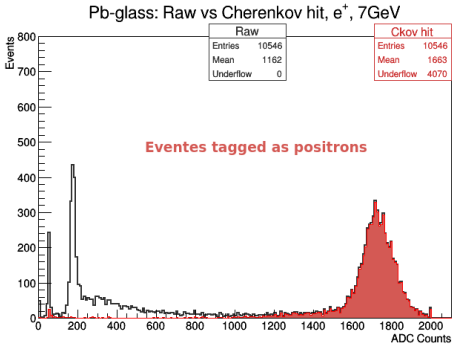

Figure 3.19: Cherenkov cut for positrons at 7GeV.

3.2.2 Cherenkov cuts for electrons

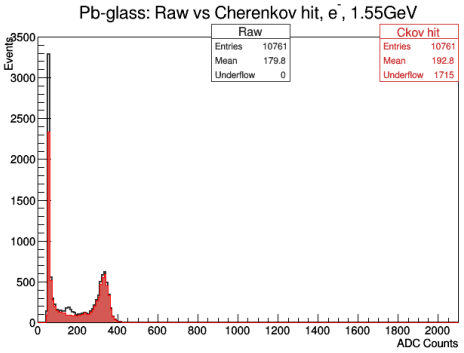

(a) e^- 1.55GeV

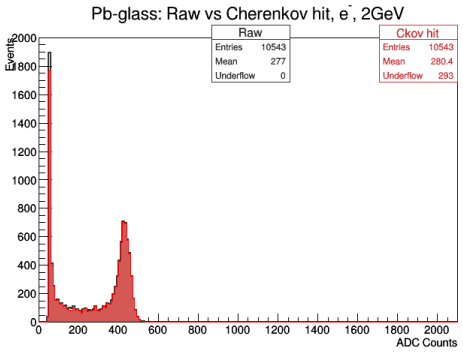

(b) e^- 2.0GeV

Figure 3.20: Cherenkov cuts for electrons, 1.55 and 2.0GeV.

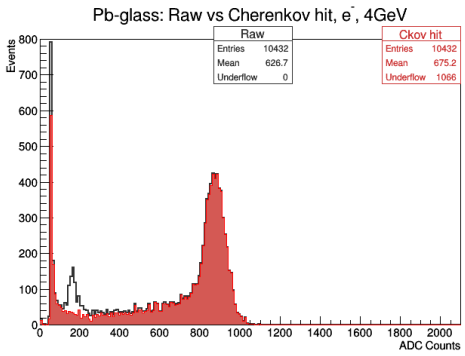

(a) e^- 4.0GeV

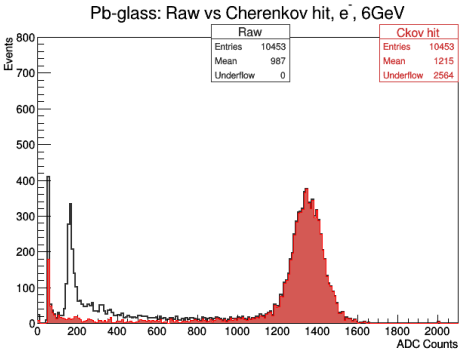

(b) e^- 6.0GeV

Figure 3.21: Cherenkov cuts for electrons, 4 and 6.0GeV.

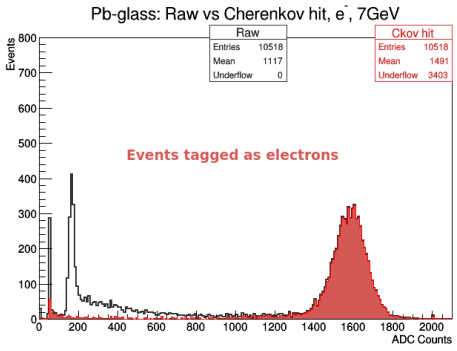

Figure 3.22: Cherenkov cut for electrons at 7GeV.

The shaded region is the electron/positron region. It is clearly seen that at lower energies, the cuts are kind of irrelevant and useless. Before giving a possible explanation for this non-expected behaviour, it is important to show the correlation plots for both Cherenkov and lead-glass spectra, they give a better and clearer view of the cuts and help to define and calculate the Cherenkov detector efficiency.

3.2.3 Cherenkov efficiency

Cherenkov efficiency was a desired quantity which had to be reported for knowing how well this detector performs when selecting electrons and positrons. Its value it is useful in determining its reliability depending on the beam energy. This information is also useful when planing the run times at different energies.

3.2.4 Efficiency from positrons

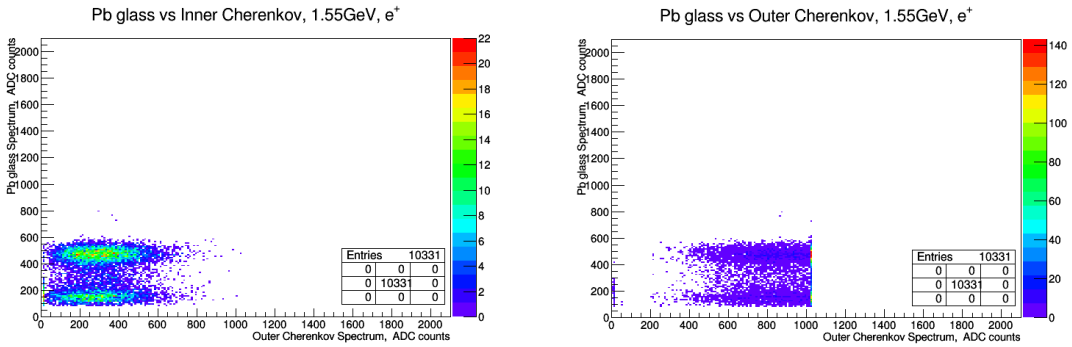

(a) e^+ 1.55GeV inner PMT

(b) e^+ 1.55GeV outer PMT

Figure 3.23: Correlation plots for positrons at 1.55GeV.

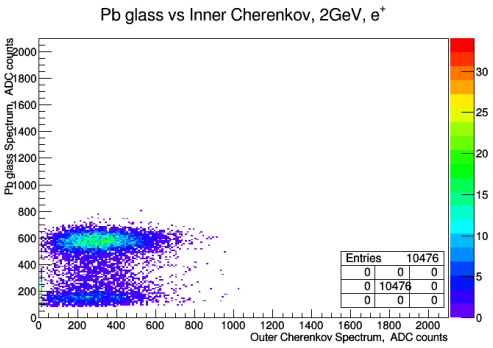

(a) e^+ 2.0GeV inner PMT

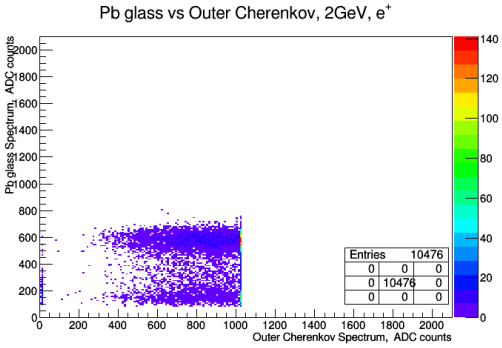

(b) e^+ 2.0GeV outer PMT

Figure 3.24: Correlation plots for positrons at 2.0GeV.

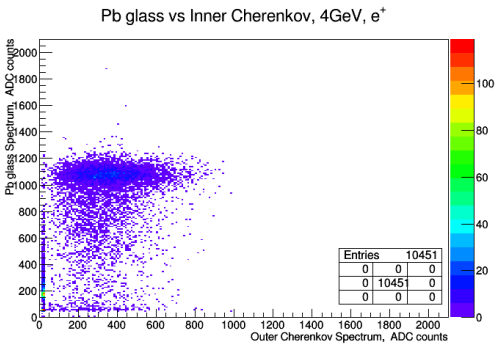

(a) e^+ 4.0GeV inner PMT

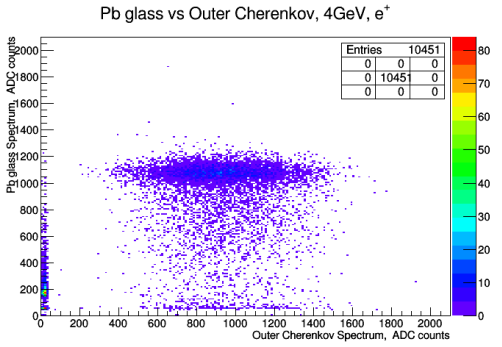

(b) e^+ 4.0GeV outer PMT

Figure 3.25: Correlation plots for positrons at 4.0GeV.

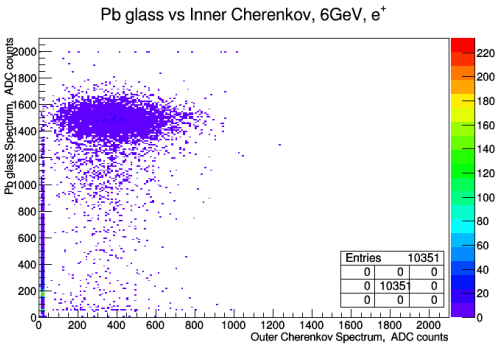

(a) e^+ 6.0GeV inner PMT

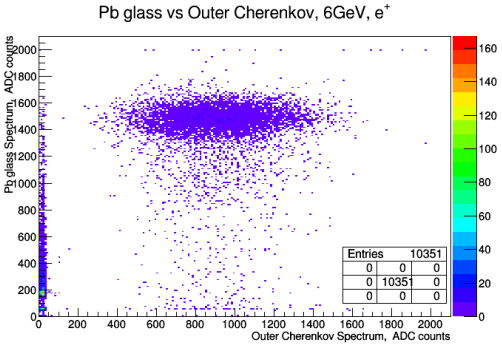

(b) e^+ 6.0GeV outer PMT

Figure 3.26: Correlation plots for positrons at 6.0GeV.

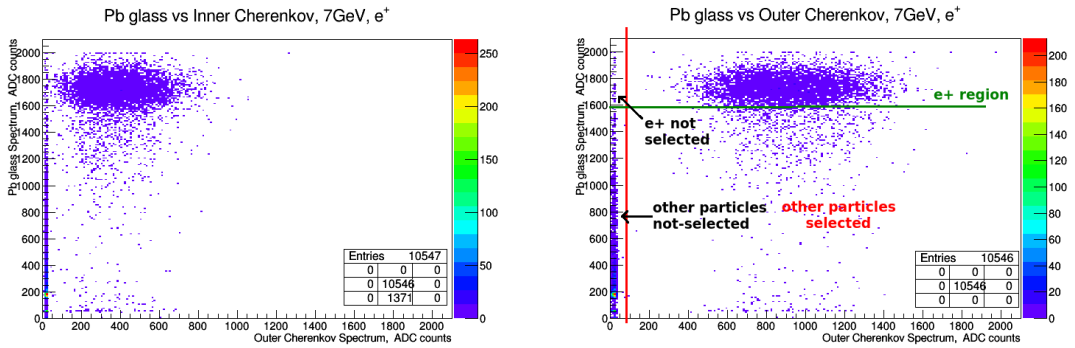

(a) e^+ 7.0GeV inner PMT

(b) e^+ 7.0GeV outer PMT

Figure 3.27: Correlation plots for positrons at 7.0GeV.

These plots exemplify clearly when the Cherenkov fired in relation with the events in the lead-glass calorimeter. Both signals are synchronized according to figure 2.13, where can be seen that both signals are in time with each other through their respective gates. Furthermore, both signals always appeared at the same instant for every SPILL. So, from figures 3.23, 3.24, 3.25, 3.26 and 3.27 it is possible to see the separation of events, which is better for higher energies. Also, from figure 3.27 the efficiency of the CC at that energy can be defined as the e^+ region/(e^+ region + e^+ not-selected region).

In the "root" macros devoted to make these plots, it was added a small program to calculate the efficiencies at each energy, where the cuts are made "by eye", i.e., drawing the red lines shown in figure 3.27. Doing this, the following values were obtained.

	positrons		**electrons**	
Energy (GeV)	Inner PMT eff.	Outer PMT eff.	Inner PMT eff.	Outer PMT eff.
1.55	99.54±.09%	99.98±.02%	99.08±.20%	99.79±.07%
2.0	99.39±.10%	99.95±.03%	99.49±.10%	99.96±.03%
4.0	99.70±.07%	99.90±.04%	99.60±.09%	99.84±.05%
6.0	99.60±.08%	99.65±.08%	99.60±.08%	99.69±.07%
7.0	99.27±.10%	99.41±.10%	99.33±.10%	99.50±.09%

Table 3.1: Cherenkov efficiencies for e^+ and e^-.

The uncertainty in the efficiency values comes from the binomial uncertainty [44]

$$\frac{N}{M} \pm \frac{\sqrt{N\left(1-\frac{N}{M}\right)}}{M} \tag{3.1}$$

where "N" events out of "M" events are selected.

3.2.5 Efficiency from electrons

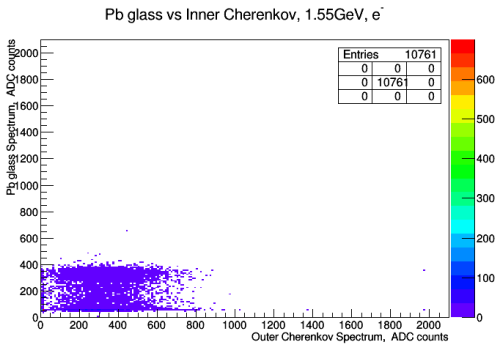

(a) e^- 1.55GeV inner PMT

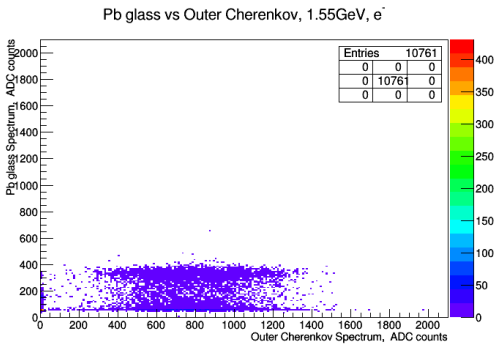

(b) e^- 1.55GeV outer PMT

Figure 3.28: Correlation plots for electrons at 1.55GeV.

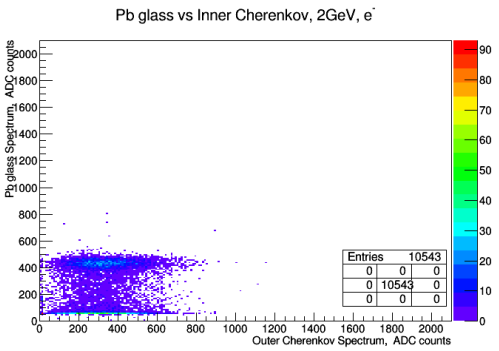

(a) e^- 2.0GeV inner PMT

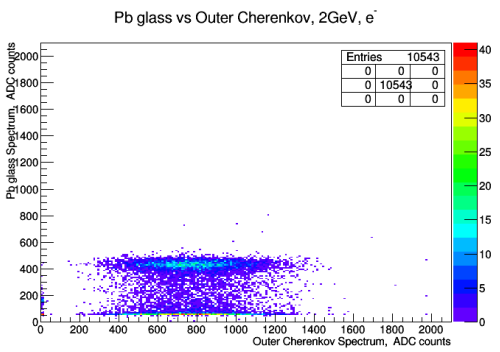

(b) e^- 2.0GeV outer PMT

Figure 3.29: Correlation plots for electrons at 2.0GeV.

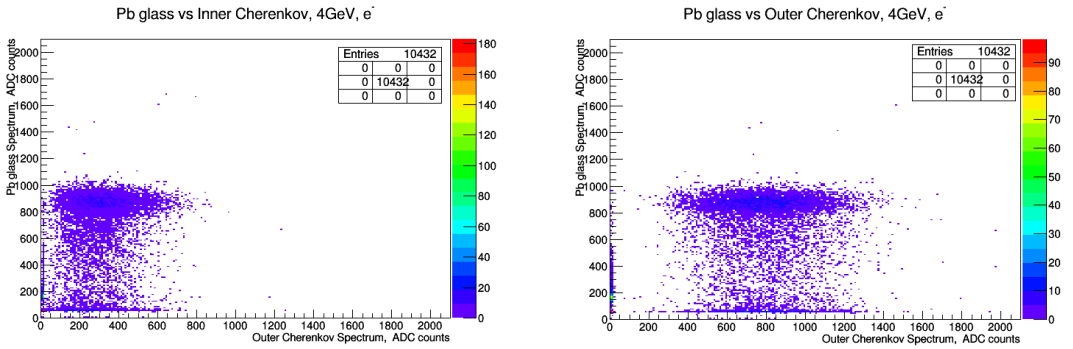

(a) e^- 4.0GeV inner PMT (b) e^- 4.0GeV outer PMT

Figure 3.30: Correlation plots for electrons at 4.0GeV.

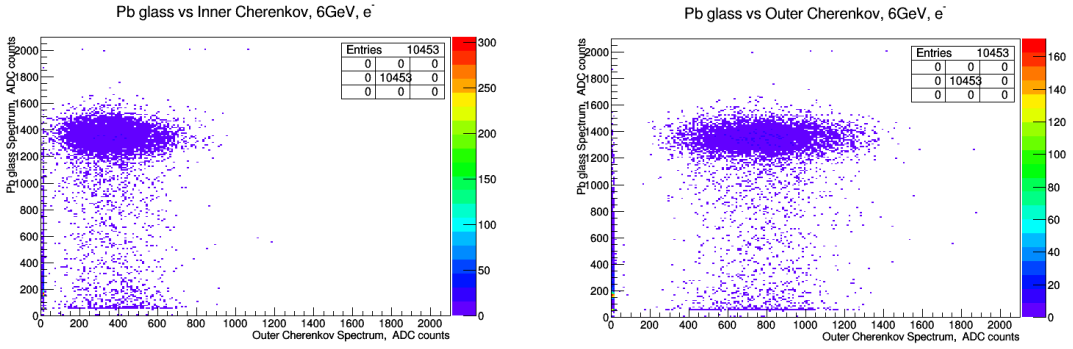

(a) e^- 6.0GeV inner PMT (b) e^- 6.0GeV outer PMT

Figure 3.31: Correlation plots for electrons at 6.0GeV.

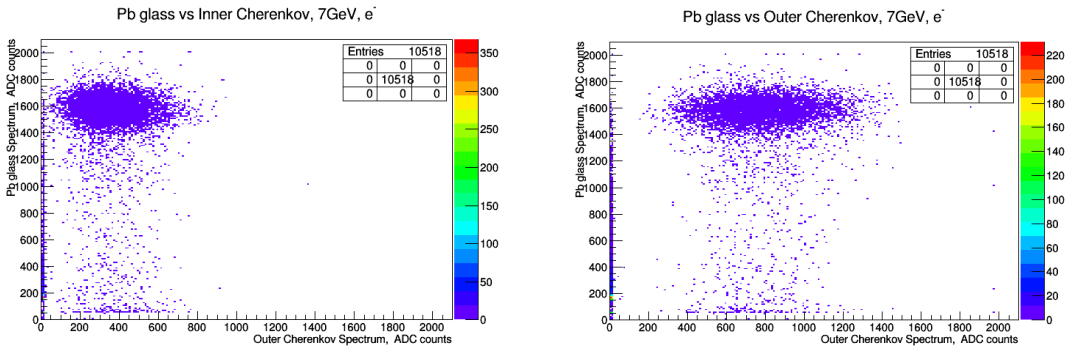

(a) e^- 7.0GeV inner PMT (b) e^- 7.0GeV outer PMT

Figure 3.32: Correlation plots for electrons at 7.0GeV.

3.3 MWPCs Data

The MWPCs were used for monitoring the beam profiles. The purpose for this, was to know how spread and centered the beam was during the data taking. This tracking procedure was really handy, because with it, was possible to know if the beam was really passing focused at the center of the chamber 3 and therefore focused at the center of the calorimeter. Without this information, runs could have been larger in order to reach the same 10000 events required per run. As going up in the energy of the incoming particles, the profile gets more focused at the center of the beam as it was expected, given that at higher energies the scattering gets diminished. In figure 3.33 are compared the beam profiles for e^+ at 1.55GeV and at 7.0GeV, as seen by wire chamber number 3, the one that was closer to the calorimeter.

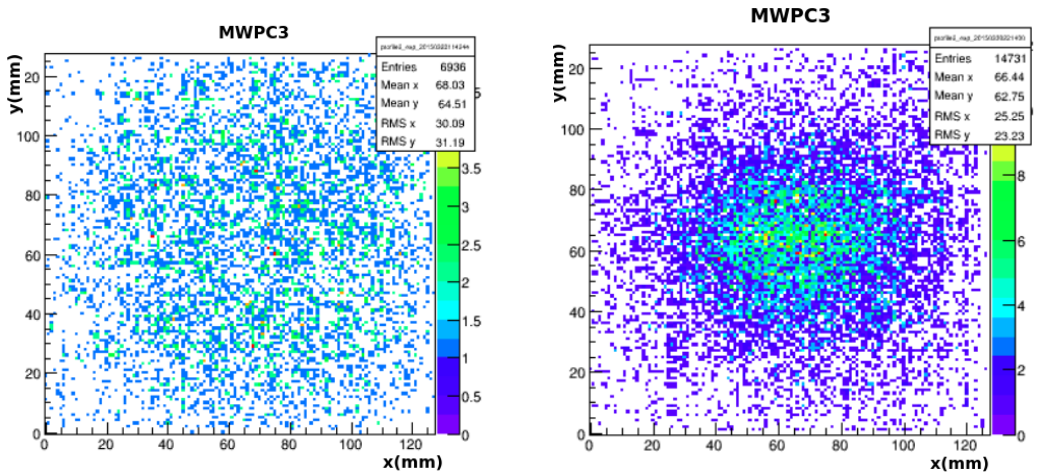

(a) e^+ profile at 1.55GeV

(b) e^+ profile at 7.0GeV

Figure 3.33: Beam profiles for e^+ at 1.55GeV and at 7.0GeV as seen by MWPC3.

Even though, the beam as a whole is more focused at 7.0GeV, for instance, it is interesting and important to note the fact that the electron/positron peak is more spread at higher energies as seen in figures at section 3.4.1 for example. We do not adventure any definitive answer to this beam characteristic.

The wire chambers, through its data acquisition system were really helpful for matching the number of triggers (events) in the wire chambers and in the lead-glass calorimeter. This was a warranty that almost all the particles getting into the calorimeter were passing through the wire chambers as well. Some other particles could passed through the calorimeter coming from other directions, like cosmic rays [45], for example. However due to their so much lower rate, they may be considered negligible.

3.4 Fits

This part of the analysis involves the adjustment of the electron and positron peaks to a "model function". By doing this, parameters such as their mean, standard deviation and a few more are obtained therewith. As part of the goals (section 2.1), perhaps the more important of them, or at least the one with more influence or repercussion is the "beam linearity". The parameters from these fits give this characteristic of the beam.

3.4.1 Fits for positrons

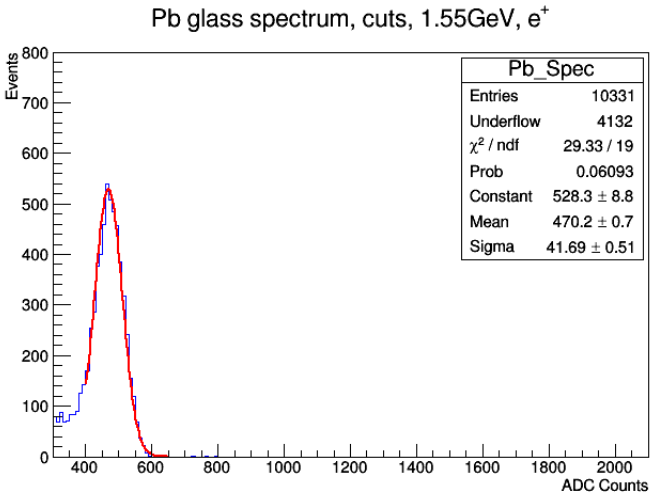

Figure 3.34: Gaussian fit for e^+ at 1.55GeV.

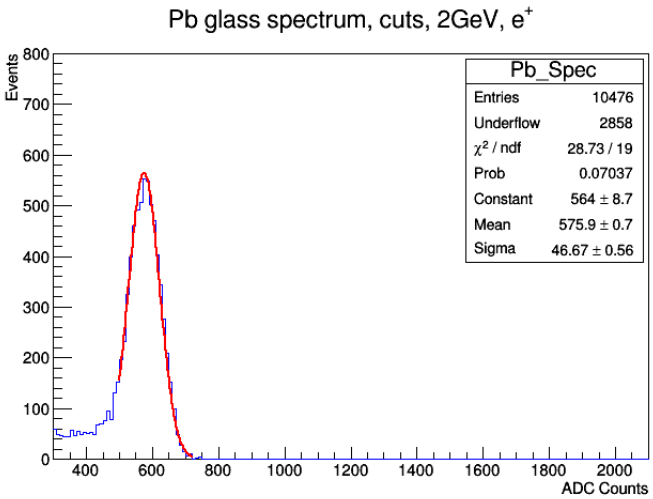

Figure 3.35: Gaussian fit for e^+ at 2.0GeV.

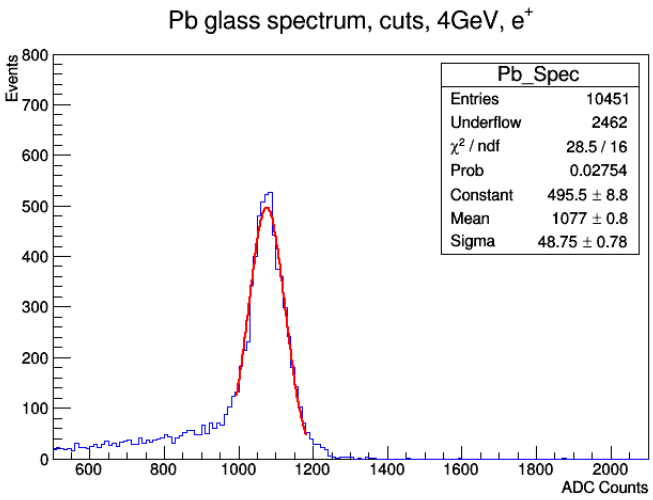

Figure 3.36: Gaussian fit for e^+ at 4.0GeV.

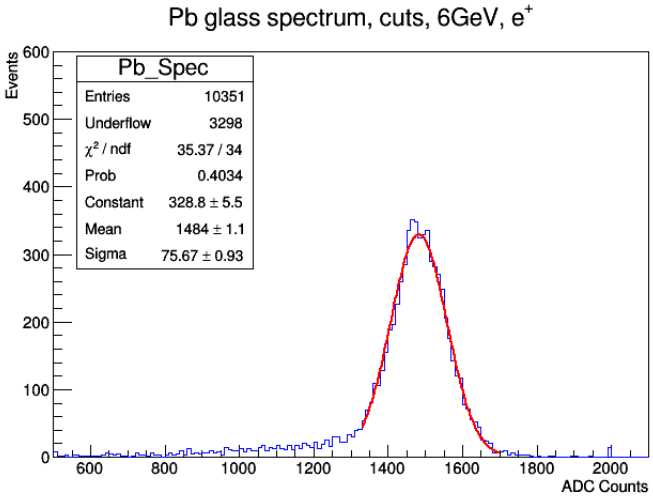

Figure 3.37: Gaussian fit for e^+ at 6.0GeV.

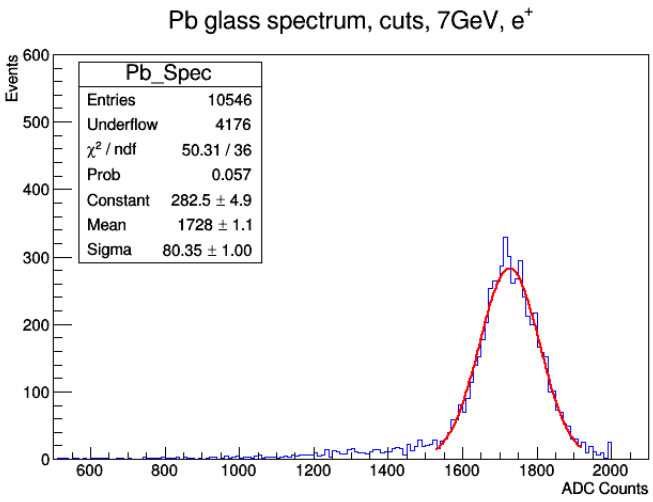

Figure 3.38: Gaussian fit for e^+ at 7.0GeV.

3.4.2 Fits for electrons

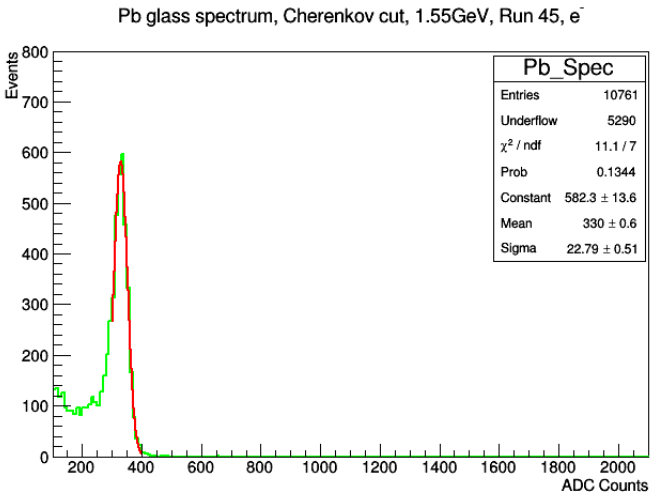

Figure 3.39: Gaussian fit for e^- at 1.55GeV.

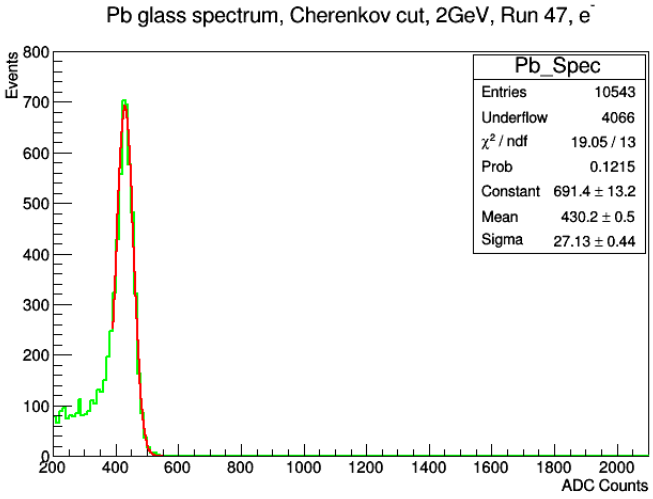

Figure 3.40: Gaussian fit for e^- at 2.0GeV.

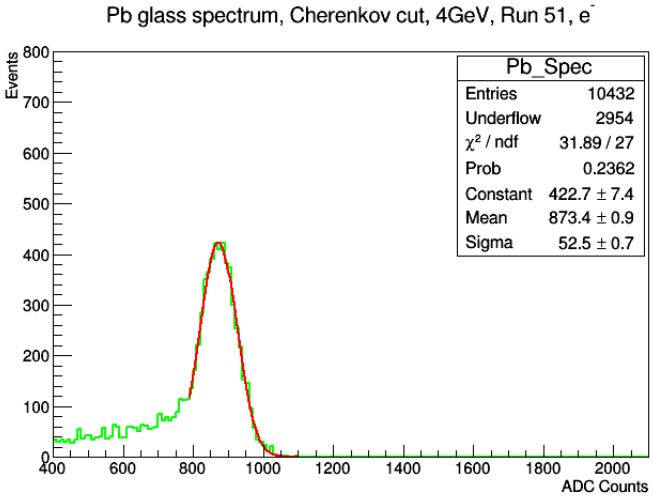

Figure 3.41: Gaussian fit for e^- at 4.0GeV.

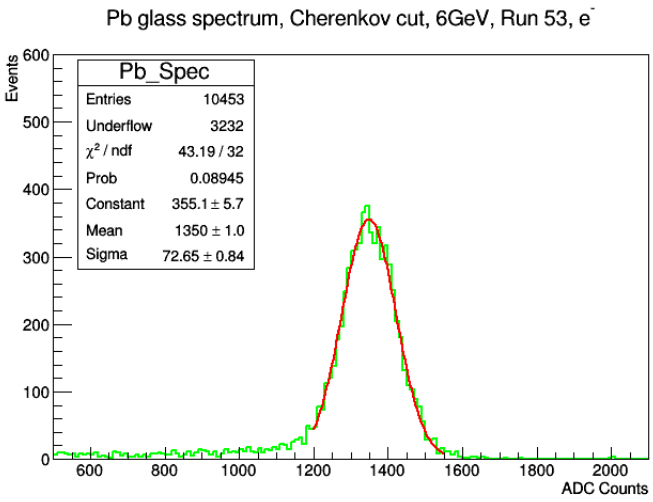

Figure 3.42: Gaussian fit for e^- at 6.0GeV.

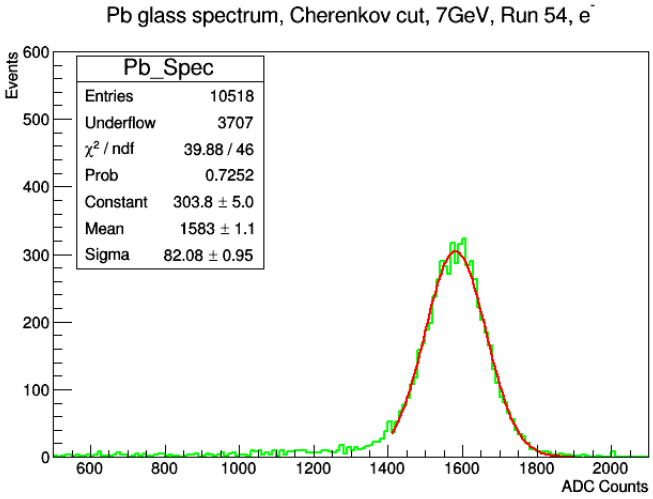

Figure 3.43: Gaussian fit for e^- at 7.0GeV.

3.4.3 Fit Analysis

Root by CERN [46] is a really useful data analysis framework which allows, among other things, a quick and reliable construction of histograms and the calculation of all their parameters. In the plots of the previous sections: 3.4.1 and 3.4.2, appears a "statistical box" that gives the statistics and fit parameters. Specifically, for each energy and for each polarity, the statistical box gives:

- Number of entries: Number of events into the calorimeter for that specific run.
- Underflow: Which are the rejected events by means of the Cherenkov cut.

- χ^2/ndf (number of degrees of freedom): A test for the goodness-of-fit of theoretical formulae to experimental data.
- Probability: This is a more rigorous test for the goodness-of-fit. It is the probability of obtaining a χ^2 value coming out what was saw in the data.
- Constant: Amplitude of the Gaussian fit.
- Mean: Mean of the Gaussian fit.
- Sigma: Standard deviation of the Gaussian fit.

There are a few things to explain about these parameters. First, as can be seen, the fits for all the peaks are Gaussian fits. They do not fit the entire shape of the spectra as was expected, because there is a merge between electrons and pions at the left tail of the peak, and because of the particles not crossing the whole length of the calorimeter, as well. Fitting with other distributions was not required, because the statistical parameters involved with the Gaussian, were already "pretty" good (see tables 3.2 and 3.3).

The fit is considered good if $\chi^2/ndf \sim 1$, and a more rigorous test for the fit is that for which the "Probability value is $\geq 5\%$ [20]. All the fits but the one for positrons at 4GeV met both requirements. This point has $\chi^2/ndf = 28.5/16 = 1.78$ which might appear to be a good fit, but has a Probability=2.75%. However the fit is close to the limit of 5% for the probability value and given that it is not that bad, it was decided to be used for the analysis. Tables 3.2 and 3.3 summarize the parameters coming from the fits.

positrons				
Energy (GeV)	Mean	σ (standard deviation)	χ^2/ndf	Probability
1.55	470.2±0.7	41.69±0.51	29.33/19=1.54	0.06
2.0	575.9±0.7	46.67±0.56	28.73/19=1.51	0.07
4.0	1077.0±0.8	48.75±0.78	28.5/16=1.78	0.03
6.0	1484.0±1.1	75.67±0.93	35.37/34=1.04	0.40
7.0	1728.0±1.1	80.35±1.00	50.31/36=1.39	0.06

Table 3.2: Fit parameters for e^+.

electrons				
Energy (GeV)	Mean	σ (standard deviation)	χ^2/ndf	Probability
1.55	330.0±0.6	22.79±0.51	11.1/7=1.58	0.13
2.0	430.2±0.5	27.13±0.44	19.05/13=1.46	0.12
4.0	873.4±0.9	52.5±0.70	31.89/27=1.18	0.24
6.0	1350.0±1.0	72.65±0.84	43.19/32=1.34	0.09
7.0	1583.0±1.1	82.08±0.95	39.88/46=0.86	0.73

Table 3.3: Fit parameters for e^-.

3.5 Linearity of the Beam

Taking the mean from tables 3.2 and 3.3, a plot showing the expected or advertised energy by MCR versus the counts of the ADC coupled to the PMT attached to the calorimeter, can be made. The importance of this plot, even though it does not show an absolute energy scale, is extremely useful.

It was supposed that MCR delivered the beam based in an equation (the beam equation) which is the equation of a straight line (equation 3.2). Using this equation, MCR selected the momentum required by the user and then set the magnetic field in the Hall probe and that was it, the user trusted MCR.

But MINERvA folks at Test Beam decided to measure this characteristic of the beam directly, without trusting MCR. Therefore, even using a simple Analog-to-Digital Converter (ADC), which is a pretty linear device (section 3.5.1) [37], and a Photo-Multiplier Tube (PMT), not as linear as the ADC (section 3.5.1), the data points corresponding to the mean of the fit, for each energy and for each polarity could be obtained, and this way a test for the "beam linearity" could be made.

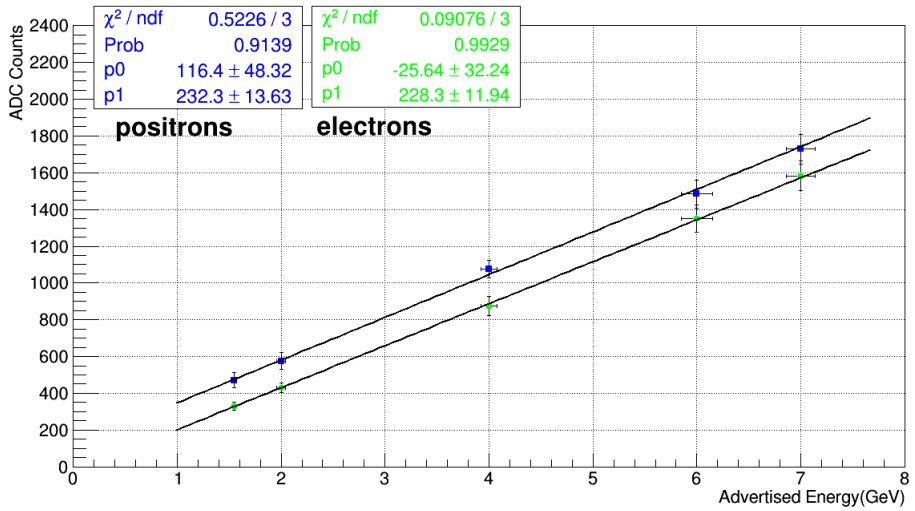

Figure 3.44: Linear fit for both e^+ and e^-.

In figure 3.44 the vertical errors correspond to σ (the standard deviation) [20], and the horizontal errors correspond to the 2% uncertainty of the beam energy, according to MCR. Perhaps at first glance, there is not an astonishing result from this plot. But there are two considerably separated lines where it was expected to be just one, or maybe two, but statistically equivalent (really close to each other), but these, are not.

This result, and other similar obtained using the TB detector calorimeter (figure 1.30), showed that when users asked for the same energy at different polarities, they actually were getting different polarities, but as well, different energies.

There is a different way to look at the beam linearity, or should it be said, beam non-linearity. In figure 3.45 the plot gives the rms (root mean square) value [20], for the energy points for both polarities. This means, the percent deviation of these points from the fit line, which represents 0% deviation.

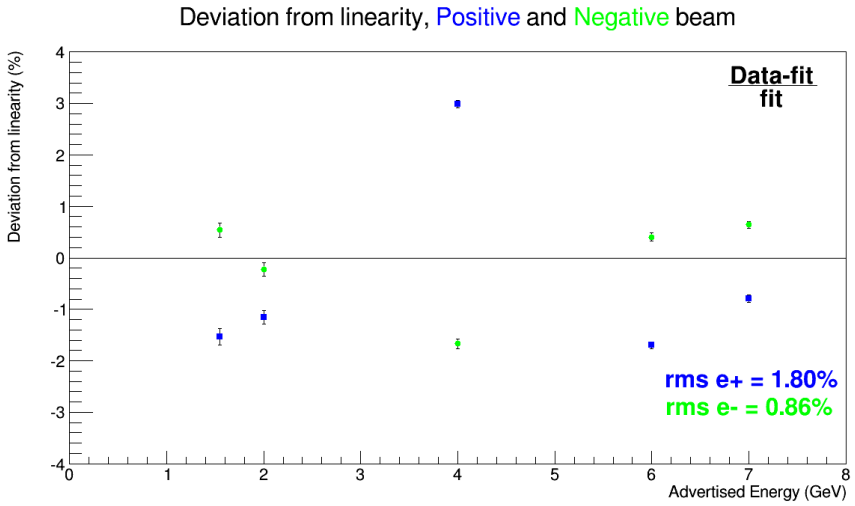

Figure 3.45: Rms for both e^+ and e^-.

The fits made in the positive and negative lines (figure 3.44), deliver 2 parameters, the slope (p_1) and the intercept (p_0), through them it is possible to calculate which would be the "mean" for each "energy point", this value receives the name of "fit", whereas the value gotten experimentally, receives the name of "data". Then, computing the value $(data - fit)/fit$, the percentage of deviation from the fit line is obtained and a value assigned to the plot (figure 3.45). The error is represented by calculating the error in quadratures for: $(data - fit)/fit$, i.e., $\delta\left[(data - fit)/fit\right]$, which gives: $\delta\left(data\right)/fit$. The error on the data is the error on the mean that shows up at tables 3.2 and 3.3 [20].

3.5.1 Linearity of the devices

Devices like the PMT, ADC and the lead-glass calorimeter present effects of non-linearity. For the ADC, no corrections were made, given that its integral non-linearity is $< 0.2\%$ of reading [20], this means that it differs from the best straight line fit to measure its points, for at most 2 counts in a 1024-channel device. This value is smaller than the final uncertainty expected by the MINERvA Test Beam crew.

Although it is well known the lead-glass block has been used in many successful experiments ([47] for instance), it has been used since the 70's, and is very probable that this had caused loss of linearity. It would have been a good idea to expose the block to sunlight in order to try to reverse this loss of linearity [48]. However, the beam busy schedule did not allow us to do so, and there

was not such possible improvement in linearity, and a certain fraction of the beam non-linearity is due to the calorimeter.

Once the remainder of devices were trusted to be linear to a certain extent, it remained to look at the PMT, to get the best resolution, response and linearity for the detector at a given HV. First, data was taken at some voltages (1050, 1100, 1150 and 1200V) for each energy. However when trying for small voltages (1050 and 1100V) there was a poor, almost null separation of the electron from the pion/muon peak at the lead-glass spectra (see figures 3.2 and 3.5). When trying 1200V, there was overflow of events at the 7GeV level in both figures 3.2 and 3.5. So 1150V was picked, this HV value has a maximum sensitivity of 30, compared to the recommended sensitivity region 50/200 [30]. The constraint noy allowing to go further in voltage was the lack of ADCs able to avoid overflow (maybe a 12-bit ADC). Of course, the PMT also carries a fraction of the measured beam non-linearity. The PMT was not tested for linearity, the reason why, is because the procedure available for the PMTs available involves light pulses so much slower than the Cherenkov pulses created at the lead-glass [48].

From figure 3.45 arises an interesting and decisive feature of the beam: if its non-linearity were just due to the devices (PMT, ADC and calorimeter), the plot would be pretty symmetric, i.e., points for opposite polarities would lie at opposites sides of the 0%-deviation line, this means that if the beam were symmetric by itself, the non-linearity from devices would affect it the same at any polarity, and clearly this is not the case.

3.5.2 Change of the beam equation

The beam equation already explained in section 1.2.5, had to be changed after the MINERvA Test Beam crew found out MCR was not delivering the same energy for both polarities, and actually it was found out that MCR did not know whether the "positive or negative" beam had the right value, or if one had the right value, even.

Then, as already mentioned, MCR stared an analysis to verify the magnet settings, in specific, the value of the magnetic field for the so called, "Hall probe", which is the guiding value to determine the beam momentum.

Once this process ended, MCR came out with a new equation, changing from

$$MT4W(Gauss) = +10.96Gauss + (57.92Gauss/GeV)\, P_{BEAM} \tag{3.2}$$

to

$$MT4W(Gauss) = -11.75Gauss + (57.92Gauss/GeV)\, P_{BEAM} \tag{3.3}$$

It is clear that they only changed the intercept of the straight line, but the change was considerable large, from +10.96 Gauss to -11.75 Gauss. When this change was set, no more lead-glass data were taken, and for now it is no possible to have a comparison of the beam linearity, using the "old" and "new" equation. However, the people in charge of the MINERvA TB detector, had the chance to take data with the TB detector calorimeter (see section 1.2.5). With their new results it turned out that the beam equation settings now is much better, but how much better? see [49].

What it can be done with the lead-glass data, is to look at the new beam equation and see what really the energies were at the time of taking data, performing just an easy calculation. So with the old equation, the magnetic field in the MT4W Hall probe, let us say for 2GeV, was

$$+10.96 Gauss + (57.92 Gauss/GeV)\, 2.0 GeV = 126.8 Gauss \tag{3.4}$$

Using the new (corrected) beam equation, this value in Gauss corresponds actually to

$$P_{BEAM} = (126.8 Gauss + 11.75 Gauss) \,/\, (57.92 Gauss/GeV) = 2.392 GeV \tag{3.5}$$

Doing the same correction for all the energy points, for both polarities, these are the energy points at which data were actually taken:

Old requested Energy (GeV)	**Old MT4W probe (Gauss)**	**New corrected P_{BEAM}**
1.55	100.74±1.0	1.94±0.05
2.0	126.80±1.0	2.39±0.06
4.0	242.64±1.0	4.39±0.10
6.0	358.48±1.0	6.39±0.13
7.0	416.40±1.0	7.39±0.15
-1.55	-78.81±1.0	-1.16±0.04
-2.0	-104.88±1.0	-1.61±0.05
-4.0	-220.72±1.0	-3.61±0.08
-6.0	336.56±1.0	-5.61±0.12
-7.0	-394.48±1.0	-6.61±0.14

Table 3.4: Actual energy points at which data were taken.

The uncertainties in table 3.4 were reported by the Fermilab Accelerator Division (AD).

3.5.3 Redoing fits

Having the actual energy values at which data were taken, it is mandatory to redo plots 3.44 and 3.45, and see how they look using the corrected values.

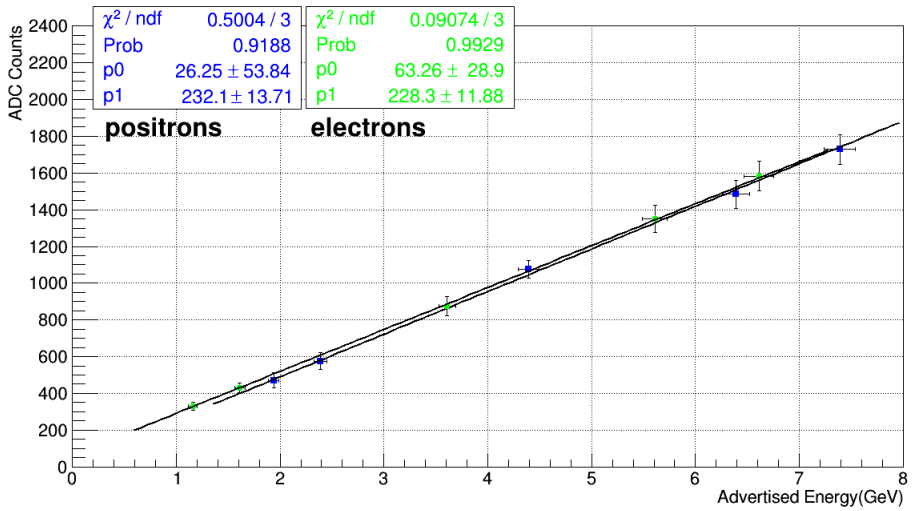

Figure 3.46: Linear fit for both e^+ and e^-, using actual energy points.

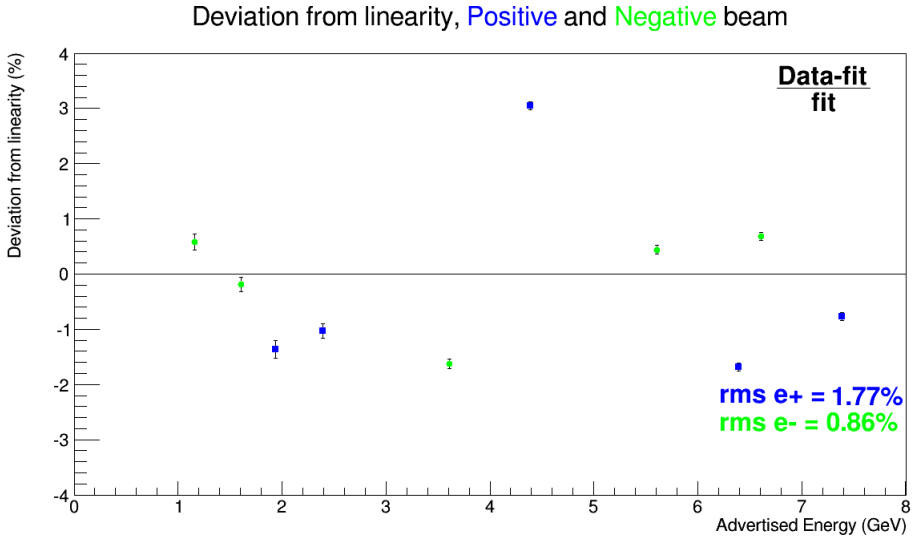

Figure 3.47: RMS for both e^+ and e^-, using actual energy points.

This time there are different lines in figure 3.46 and different points in figure 3.47. Lines are now closer, but it does not mean that the energies were the same, it is just that they have been shifted in opposite directions, according to the actual energy values.

3.5.4 Difference between polarities

Now, the differences between polarities using the old beam equation, are presented. Doing this comparison at that time, is the way MCR and AD found out they were doing wrong.

Looking at the fitted peaks (section 3.4), is clear that for a given energy value, the means are different for different polarities, and not just the mean, also σ. The standard deviations are almost the double for positrons than electrons at 1.55 and 2.0GeV, so, for these two values the difference is shown only in terms of the means. For the other three points, their standard deviations are different at an 8% level at most, therefore their difference is also given in terms of their standard deviation.

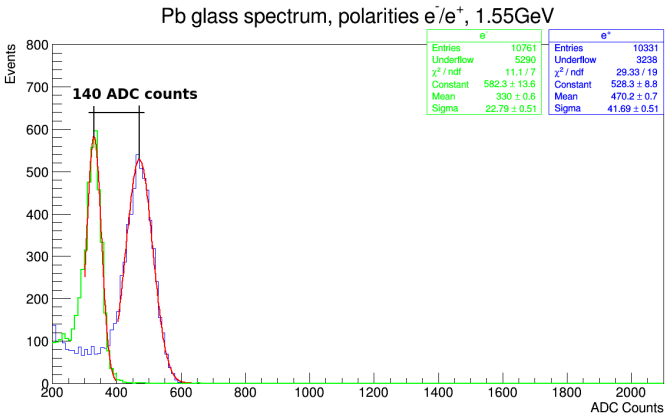

(a) Difference between polarities at 1.55GeV

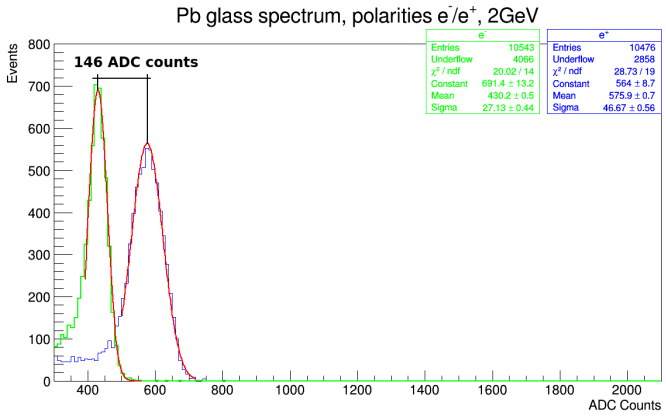

(b) Difference between polarities at 2.0GeV

Figure 3.48: Difference between polarities, 1.55 and 2.0GeV.

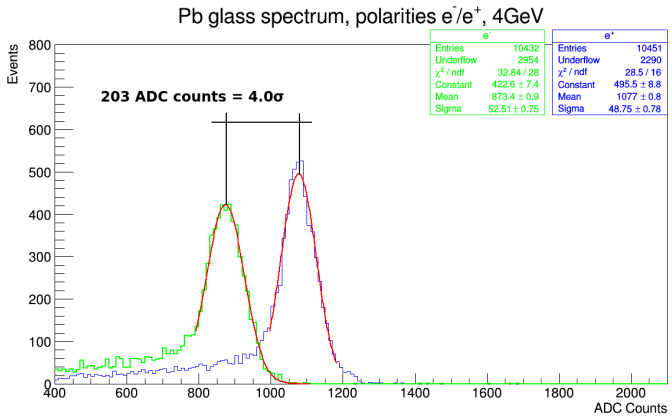

(a) Difference between polarities at 4.0GeV

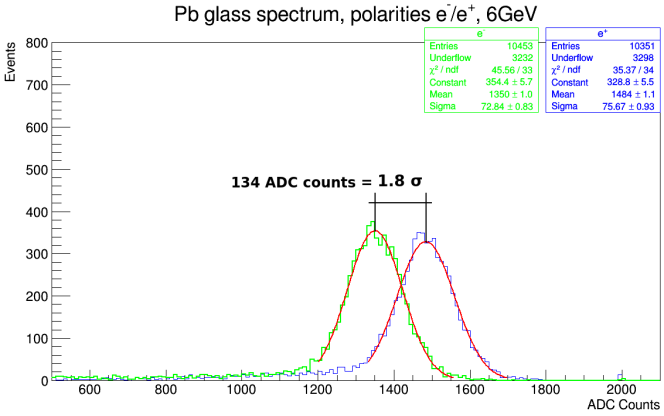

(b) Difference between polarities at 6.0GeV

Figure 3.49: Difference between polarities, 4.0 and 6.0GeV.

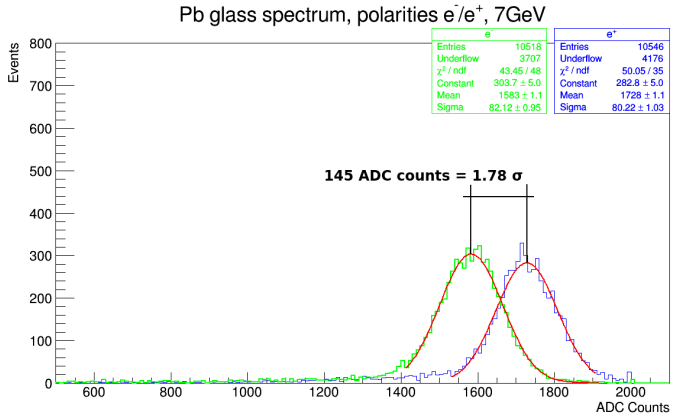

Figure 3.50: Difference between polarities at 7.0GeV.

The differences are shown in terms of ADC counts (difference between means) and in terms of standard deviations, σ.

3.6 Electron Content

The electron and positron content of the beam can be determined at a certain extent. There are three methods at hand to do it and they deliver different values, especially at lower energies.

The first one is to look at the Cherenkov cuts (section 3.2) and simply give the percentage of events that the Cherenkov detector tagged as electrons. Of course this method will fail at the lowest energy values, where the cuts make no difference; it also accounts for the leakage events, these are those events with a small energy deposition, but tagged by the CC.

The second utilizes the same "eye cuts" used for determining the Cherenkov efficiencies, selecting only the events selected by the CC, from the cut to the rightmost bin as in figure 3.27.

The third method consists in counting the "bin" content of all the bins below the fit line from the left end of the fit line to the rightmost bin (section 3.4).

These values are summarized, for the three methods in table 3.5.

	positrons			**electrons**		
Energy	CC cut	Eye cut	Bin Content	CC cut	Eye cut	Bin Content
1.55GeV	97.67±.15%	51.50±.49%	51.51±.49%	84.06±.35%	35.77±.46%	29.75±.44%
2.0GeV	96.24±.19%	60.24±.48%	60.27±.48%	97.22±.16%	49.02±.49%	42.15±.48%
4.0GeV	83.68±.36%	59.01±.48	57.84±.48%	89.78±.30%	50.89±.49%	52.07±.49%
6.0GeV	69.91±.45%	58.29±.48%	60.53±.48%	75.47±.42%	59.78±.48%	61.91±.48%
7.0GeV	61.41±.47%	53.40±.49%	55.42±.48%	67.65±.46%	65.51±.46%	59.38±.48%

Table 3.5: Approximate e^+ and e^- content of the beam, using CC cuts, eye cuts and the bin content.

Of course the low energy values are pretty different, but it is necessary to understand the rare functioning of the CC at these levels, as was already mentioned, there is a higher double occupancy at these levels [12]. Also there was a thesis, which says that probably some pions knocked out some electrons, making the CC to fire.

Although the CC was at the time working just as a threshold CC [50], it has mirrors which can make the detector to work as a RICH (Ring Imaging CHerenkov) [43], and thus, there is an alternative and less strong thesis that the effect is due to mirror misalignment [51]. It is probably not a good thesis because, mirrors misalignment would no produce a Cherenkov glow out of nothing, but all of these ideas need to be proved before giving any conclusion.

At higher energies, all methods begin to give closer values of the content, although they are not that close, yet. The uncertainty values come again from the binomial uncertainty formula 3.1, [44].

3.7 Tuning

When looking at different runs, even for the same "expected energy", there were also differences [1]. This of course was expected, but just within the 2% level advertised by MCR. Here is shown the so called "tuning" or reproducibility of the negative (e^-) beam, i.e., how well MCR is able to deliver a beam with the same characteristics through time.

The runs commented here were taken with a few days of difference between each other (April 15th and April 19th, 2015 [38]). It is supposed that MCR "plays" with currents in the magnets in order to set probe's magnetic field (always the same value), when users ask for the same energy and polarity. Here are shown the differences in tuning for the 2.0 and 7.0GeV.

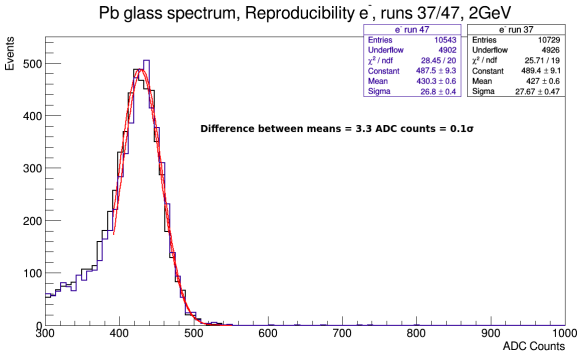

Figure 3.51: Reproducibility of the electron beam at 2.0GeV.

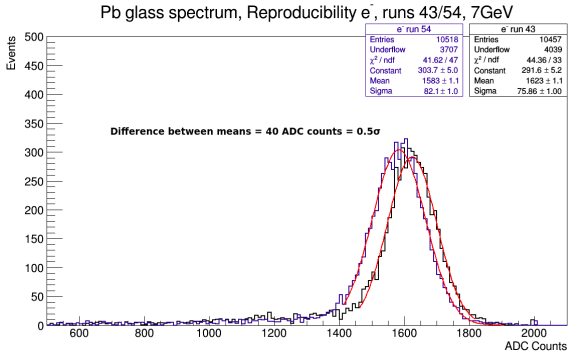

Figure 3.52: Reproducibility of the electron beam at 7.0GeV.

[1] Due to the busy schedule of MTest, and for that reason the busy schedule of the beam, it was possible to perform just 3 runs: 2 for e^- and 1 for e^+.

These plots show the best and the worst tunings respectively. It has to be mentioned that this issue has nothing to do with the beam equation, because in this case, it was supposed the beamline had the same settings. Here, the difference is greater than the maximum 2% ($\sim 2.5\%$).

3.8 Energy Resolution

For detectors which are designed to measure the energy of the incident radiation, the most important factor is the energy resolution. This is the extent to which the detector can distinguish two closely lying energies. Ideally, the detector would give a sharp delta-function peak. In reality this is never the case, and one observes a peak structure with a finite width, usually Gaussian in shape. In general, the width arises because of fluctuations in the number of ionizations and excitations produced [20]. In this experiment, the fluctuations were principally due to leakage out of the back and leakage at the sides of the calorimeter.

The resolution is usually given in terms of the full width at half maximum of the peak (FWHM). Energies which are closer than this interval are usually considered unresolvable. The energy resolution at an energy E, is

$$\Delta/E = FWHM/E \approx 2.355\sigma/E \tag{3.6}$$

A lead-glass "SF5" calorimeter has an ideal resolution given by [22], [24], [28]

$$0.01 + 0.05/\sqrt{E\,(GeV)} \tag{3.7}$$

Let us perform this calculation for each of the energy points tested. Equation 3.6 is the measured resolution, while equation 3.7 is the predicted resolution. There is no need to use either the actual energy value (new beam settings) or the first measured quantities. Because we have been using relative energy (ADC counts), we have the information needed, and can define a resolution in terms of these quantities. We must clarify that the resolution is nor solely of the detector nor of the beam. There is a merged resolution depending on both of them. We are about to compare the measured resolution against the lead-glass ideal resolution [22], [24], [28], the last one concerns only to the detector's resolution. Even though, obtaining the experimental resolution helps to better understand the beam and the detector, and how the last one performs under the influence of the former. So, in equation 3.6, E is represented by the mean in ADC counts.

	positrons		**electrons**	
Energy (GeV)	Ideal resolution	M. resolution	Ideal resolution	M. resolution
1.55	0.0501	0.2088±0.0123	0.0501	0.01626±0.0224
2.0	0.0453	0.1908±0.0120	0.0453	0.1485±0.0163
4.0	0.035	0.1066±0.0160	0.0350	0.1415±0.0134
6.0	0.0304	0.1200±0.0123	0.0304	0.1267±0.0116
7.0	0.0289	0.1095±0.0124	0.0289	0.1221±0.0116

Table 3.6: Ideal and measured energy resolutions.

Where the errors are expressed as sums in quadrature of the errors of the mean and σ.

Chapter 4

CONCLUSIONS

MINERvA could be understood as a "chain" of calibration processes, where the final goal is to reduce the uncertainties in the neutrino-related measurements.

The study of the electron/positron beam at MTest is a third generation calibration process, given that it is part of one of the calibration systems of the Test Beam detector, which is in itself, a calibration process for the MINERvA full (main) detector.

The analysis of the low-energy electron/positron beam was a procedure to determine at a certain extent and in a relative way (by means of ADC counts, not an absolute energy, which is being generated with a Monte Carlo model), the points lying in the horizontal axis of plots 1.16, which is the energy to which the incoming particles, reach the Test Beam detector. So, if MINERvA wants to reduce uncertainties, it has to know pretty well the energy of these particles in all of its calibration systems.

The information taken out from the current analysis, can be summarised as follows:

- With the fits performed to the electron and positron peaks, the low-energy electron/positron beam, was found to have a deviation from linearity of the order of 2% for positrons and of the order of 1% for electrons.
- In plot 3.45 there is a clear non-symmetric deviation from linearity related to both polarities. If the observed deviation from linearity were due to the measurement devices, it would be symmetric. This means that the beam is not symmetric by itself, in relation with both polarities.
- From the linearity plot 3.44 it is clear that the energy corresponding to electrons is not the same than the energy of positrons, when it was "believed" to be so. The largest difference is at the "advertised" 4.0GeV value, with $\approx 4.0\sigma$ apart from each other. Lead-glass result together with the result coming from the TB detector calorimeter (section 1.2.5), made MCR changed their "beam equation". Because of this, some of the runs already taken with the TB detector had to be performed again.

- An also unexpected, and outstanding result is the difference between runs of the supposed same energy and polarity. This means that there is a non-reproducibility of the beam energy. This fail in tuning is now under study. However it has to be mentioned that the non-reproducibility is within the 2% tolerance at the energy values of 1.55 and 2.0GeV.
- The Cherenkov efficiency has been demonstrated to be around 99%, for all energy measurements. This was done, making cuts "by eye".
- The "failure" of the Cherenkov counter at low energies avoids to well-determine the electron/positron content of the beam, which with the use of approximate calculations, is between 50 to 60%. Though these values are not quite trusted.
- The measured energy resolution is higher than (worse than) the ideal energy resolution, at some values is five times the ideal resolution. It has to be taken into account that the detector has leakage out of the back and at its sides. These leakages accounts for the mismatch in the resolution.

Appendix A

TEST BEAM 2, TRIGGER SYSTEM

The basic idea of the Test Beam trigger and DAQ is to emulate those of the MINERvA underground [5]. But given the difference between beams [2, 12], this is not possible.

A.1 Triggers Underground

Undeground, the trigger "tells" us that AD (Accelerator Division) sent neutrinos through the MINERvA detector. The integration gates are opened at this time and process light created in the detector by particle interactions. Here, it can be said that a trigger signals to the chance for taking interesting data.

The gate begins 0.5μs before the neutrino pulse arrives, which is 10μs long. 5.5μs after the pulse, the FEB gate is closed. At this time, the DAQ starts reading out (see figure A.1).

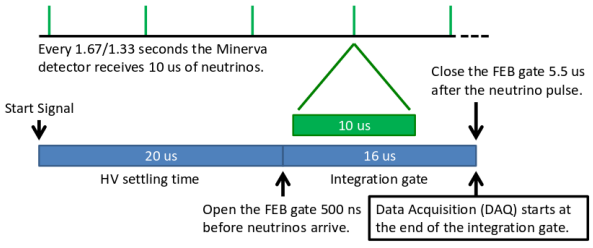

Figure A.1: Integration gate and neutrino pulse duration underground.

A.2 FEB Gates Above Ground

At the Test Beam, the situation is quite different. The idea was to get something similar to underground conditions, but as was already mentioned, it is not possible.

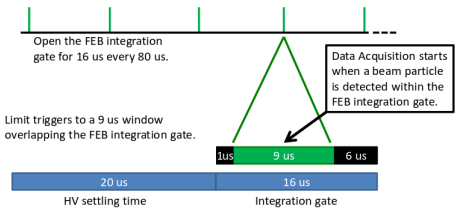

Figure A.2: Above ground gates.

Above ground, there are individual particles hitting the TB detector instead of a bunch of neutrinos. Also there is beam once every minute, during ~ 4 seconds.

At Test Beam, the DAQ starts reading out after 1μs of a particle detection, and during 9μs, as is seen in figure A.2[1]. Basically, what is done, is to open the FEB gate and hope for an interesting event. This gate has to be open as often as possible and hope that a particle reaches the detector during this time. Given that at the Test Beam there is not a signal advertising that a certain kind of particle is going to reach the detector at a specific time, the FEB gate is put in coincidence with the "CRIM" signal. So, at the coincidence between the CRIM signal with either the "Beam trigger" or the "Cosmic trigger" an event is read out, as explained below.

A.2.1 Trigger types

For getting the final Test Beam trigger, some other triggers are needed.

Beam trigger

A particle that gets into the detector and pass through Scintillator counters SC1, SC2 and SC3 is counted as a "Beam trigger". This particle has to pass during the SPILL period (~ 4 seconds). Therefore, the beam trigger is the logic coincidence: SC1&& SC2&& SC3&& SPILL (see figure A.3). When a valid event happens, the DAQ reads out all the Test Beam subsystems.

[1] All figures in this appendix, by Geoff Savage, Fermilab

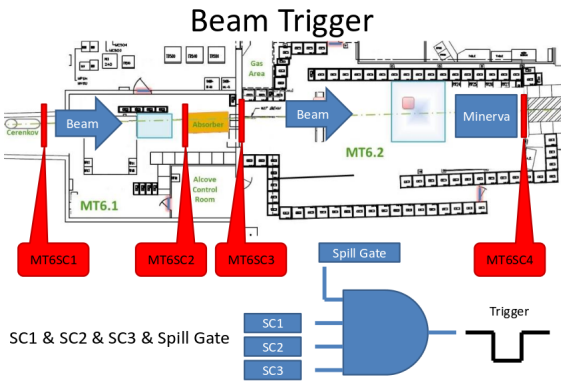

Figure A.3: Beam trigger.

Cosmic trigger

A cosmic ray passing through the detector is used for internal calibration. It is created by the coincidence of cosmic panels in front and behind the Test Beam detector (figure A.4).

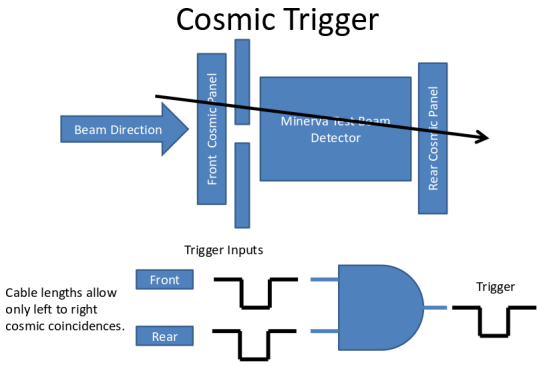

Figure A.4: Cosmic trigger.

The cosmic trigger has to be enabled just during the out SPILL period, during ~ 56 seconds. During this period, just the CAMAC DAQ is read out (not the wire chambers, obviously). The coincidence is allowed only for particles going in the front to rear panel direction, this is not because to a particular reason, it is just because the timing given by the delay cables.

A.2.2 TB trigger

Using the above triggers and a few more signals in different logic combinations, it is possible to form the so called Test Beam or MINERvA trigger. In figure A.5 there is the Test Beam trigger made by the coincidence: "Trigger or" && "neg Cherenkov" && "neg veto" && "CRIM", where "&&" means **and**, while "neg" means **the absence of**.

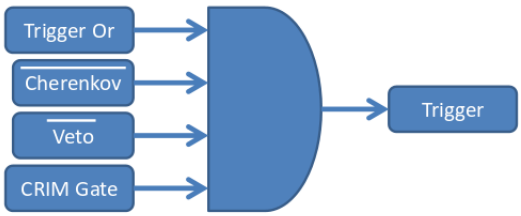

Figure A.5: TB trigger.

Trigger or

This trigger is formed by the "or" logic: Beam trigger || (Cosmic trigger && neg SPILL), were "||" means **or**. The "and" coincidence means that the cosmic events are taken into account only when there is no beam, as already mentioned. This way, the "Trigger Or" is formed either from the Beam trigger, or the Cosmic trigger presence.

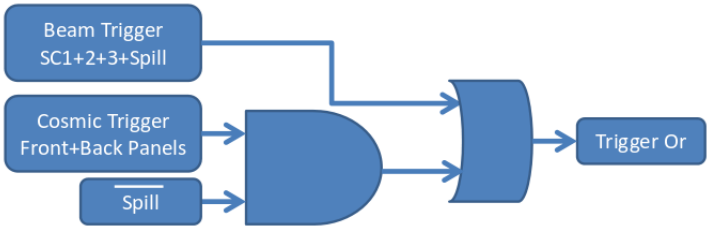

Figure A.6: "Or" trigger.

Neg Cherenkov

The "neg Cherenkov" signal is used when electron and positron like events are wanted to be avoided. As previously explained, the Cherenkov detector can send a pulse when electrons or positrons pass through it, overcoming the pressure threshold.

As explained in sections 1.1.3 and 1.2, the product of the neutrino interactions, are hadrons, which are analysed at the TB detector. Thus the Cherenkov signal is used to get rid of electron and positron events not needed here.

Neg veto

The veto signal is meant to discard events during the readout time, i.e., when the DAQ is registering a trigger, thus if a TB trigger is to be readout, it is necessary that this signal is not present. Also, the "begin spill" and "end spill" signals are required to avoid taking data during the settling or going of the spill signal, correspondingly.

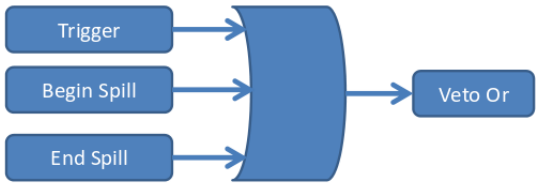

Figure A.7: Neg veto trigger.

CRIM gate

The CRIM (CROC Interface Module) signal which is rather part of the DAQ system (not treated here), is the signal providing the timing interface to the CROCEs (Chain Read Out Controller) [5]. It is a kind of clock synchronizing and the FEB gate for the acceptance of events. Just when this gate is open, and in coincidence with the CRIM signal, the TB detector accepts an event as a true event. The CRIM gate is the equivalent to the neutrino presence signal for the underground detector [52].

For the Test Beam, the CRIM opens the gates independently at a frequency set by the user ranging between 0.5Hz and 52kHz [53].

Bibliography

[1] L. Aliaga, et al., Design, Calibration, and Performance of the MINERvA Detector, Nucl.Instrum.Meth. A743 (2014) 130–159. arXiv:1305.5199, doi:10.1016/j.nima.2013.12.053.

[2] P. Adamson, et al., The NuMI Neutrino BeamarXiv:1507.06690.

[3] Minerva wiki web page, https://cdcvs.fnal.gov/redmine/projects/minerva/wiki, online; accesed 16-July-2015.

[4] S. Wojcicki, Neutrino Oscillations in Minos, in: Proceedings, 16th Lomonosov Conference on Elementary Particle Physics: Particle Physics at the Year of Centenary of Bruno Pontecorvo, 2015, pp. 52–57. doi:10.1142/9789814663618_0010.

[5] G. N. Perdue, et al., The MINERνA Data Acquisition System and Infrastructure, Nucl. Instrum. Meth. A694 (2012) 179–192. arXiv:1209.1120, doi:10.1016/j.nima.2012.08.024.

[6] L. Aliaga, et al., MINERvA neutrino detector response measured with test beam data, Nucl. Instrum. Meth. A789 (2015) 28–42. arXiv:1501.06431, doi:10.1016/j.nima.2015.04.003.

[7] Ftbf web page, http://ppd.fnal.gov/ftbf/, online; accesed 16-July-2015.

[8] Fermilab web page, http://www.fnal.gov/, online; accesed 16-July-2015.

[9] D. P. Moehs, J. Peters, J. Sherman, Negative hydrogen ion sources for accelerators, IEEE Trans. Plasma Sci. 33 (2005) 1786–1798. doi:10.1109/TPS.2005.860067.

[10] Fermilab switchyard rookie book. a complete explanation of fermilab's beamlines and their components., http://www-bdnew.fnal.gov/operations/rookie_books/Switchyard_v3.3.pdf, online; accesed 16-July-2015.

[11] Fermilab switchyard notes page. a complement for fermilab's rookie book, explanation for all the beamline magnets., http://www-bd.fnal.gov/external_beams/Projects/MTest/EBMemopad.html#IIIa, online; accesed 16-July-2015.

[12] Ftbf page about the beam delivery path. it also explains the double occupancy events., http://ppd.fnal.gov/ftbf/beam/delivery.html, online; accesed 16-July-2015.

[13] Geant4 web page., http://geant4.cern.ch/http://geant4.cern.ch/, note = Online; accesed 16-July-2015.

[14] C. E. Perez, A. M. Gago, J. Morfin, D. A. Jensen, R. Gran, BeamLine Design for MINERvA TestBeam Detector, in: Hadron collider physics. Proceedings, 19th Symposium, HCP2008, Galena, USA, May 27-31, 2008, 2008. arXiv:0808.0199.
URL https://inspirehep.net/record/792153/files/arXiv:0808.0199.pdf

[15] Ftbf instrumentation web page., http://www-ppd.fnal.gov/ftbf/instrumentation/index.html, online; accesed 16-July-2015.

[16] T. J. Roberts, K. B. Beard, D. Huang, S. Ahmed, D. M. Kaplan, L. K. Spentzouris, G4Beamline Particle Tracking in Matter-dominated Beam Lines, Conf. Proc. C0806233 (2008) WEPP120.

[17] H. Crannell, C. J. Crannell, H. Whiteside, J. F. Ormes, M. J. Ryan, Interaction lengths of energetic pions and protons in iron, Phys. Rev. D7 (1973) 730–740. doi:10.1103/PhysRevD.7.730.

[18] Ftbf beam delivery path page. this plot was made by the calis collaboration, though it was never published., http://ppd.fnal.gov/ftbf/beam/delivery.html, online; accesed 16-July-2015.

[19] Helium scattering., http://www.microscopy.ethz.ch/downloads/Interactions.pdf, online; accesed 16-July-2015.

[20] W. R. Leo, Techniques for Nuclear and Particle Physics Experiments, Second Revised Edition, Springer-Verlag, 1993.

[21] K. A. Olive, et al., Review of Particle Physics, Chin. Phys. C38 (2014) 090001. doi:10.1088/1674-1137/38/9/090001.

[22] T. Ferbel, Experimental Techniques in High-Energy Nuclear and Particle Physics, Second Edition, World Scientific, 1991.

[23] E. Longo, I. Sestili, Monte Carlo Calculation of Photon Initiated Electromagnetic Showers in Lead Glass, Nucl. Instrum. Meth. 128 (1975) 283, [Erratum: Nucl. Instrum. Meth.135,587(1976)]. doi:10.1016/0029-554X(75)90679-5.

[24] A. V. Dolgopolov, et al., Results of a beam test of the combined lead glass and PWO cells detector for the COMPASS electromagnetic calorimeter, Submitted to: Nucle. Instr. Method.

[25] G. Abshire, et al., Measurement of Electron and Pion Cascades in a Lead / Acrylic Scintillator Shower Detector, Nucl. Instrum. Meth. 164 (1979) 67. doi:10.1016/0029-554X(79)90434-8.

[26] W. R. Nelson, T. M. Jenkins, R. C. McCall, J. K. Cobb, ELECTRON INDUCED CASCADE SHOWERS IN COPPER AND LEAD AT 1-GeV, Phys. Rev. 149 (1966) 201–208. doi:10.1103/PhysRev.149.201.

[27] Particle Data Group., Phys. Lett 75B(1981) 1, found as a reference at Ferbel's book (Experimental techniques in high-energy nuclear and particle physics).

[28] F. G. Binon, et al., HODOSCOPE GAMMA SPECTROMETER GAMS-200, Nucl. Instrum. Meth. 188 (1981) 507. doi:10.1016/0029-554X(81)90261-5.

[29] A. N. Diddens, et al., A Detector for Neutral Current Interactions of High-energy Neutrinos, Nucl. Instrum. Meth. 178 (1980) 27. doi:10.1016/0029-554X(80)90854-X.

[30] PMT manufacturer data sheet, http://frank.pocnet.net/other/EMI/EMI_Photomultiplier_Tubes_1970.pdf, online; accesed 17-July-2015.

[31] J. Litt, R. Meunier, Cerenkov counter technique in high-energy physics, Ann. Rev. Nucl. Part. Sci. 23 (1973) 1–44. doi:10.1146/annurev.ns.23.120173.000245.

[32] Ftbf, instrumentation page. it shows the threshold pressure for cherenkov radiation in gases., http://ppd.fnal.gov/ftbf/instrumentation/cherenkov/cc_mtest.pdf, online; accesed 17-July-2015.

[33] N. Giglietto, et al., Overview of the GLAST physics, in: New worlds in astroparticle physics. Proceedings, 5th International Workshop, Faro, Portugal, January 8-10, 2005, 2005, pp. 129–133.

[34] F. Sauli, Principles of Operation of Multiwire Proportional and Drift Chambers.

[35] Minerva document with the explanation of wire chambers efficiencies., http://minerva-docdb.fnal.gov:8080/cgi-bin/RetrieveFile?docid=10770&filename=LeoB%20Collab%20Meeting%20Mar%202015%20%281%29.pdf&version=2, online; accesed 29-July-2015.

[36] LEMO Group company website., http://www.lemo.com/en, online; accesed 29-July-2015.

[37] Fermilab's physics research equipment pool. the fermilab's page to request all kind on nim and camac modules as well as a great number of other electric and electronic devices., http://cdorg.fnal.gov/ese/prep/index.php, online; accesed 17-July-2015.

[38] Minerva experiment's electronic logbook, where the entries related with the experiment are. look for entries related with the user "maramire"., http://dbweb4.fnal.gov:8080/ECL/minerva/E/index, online; accesed 17-July-2015.

[39] Spreadsheet at the ftbf page in which the user can see the pressure threshold needed depending on the particle and energy desired., http://ppd.fnal.gov/ftbf/instrumentation/cherenkov.htm, online; accesed 17-July-2015.

[40] Beam composition according to ftbf. there are some references and studies from previous experiments., http://ppd.fnal.gov/ftbf/beam/energies.html, online; accesed 17-July-2015.

[41] D. E. Groom, N. V. Mokhov, S. I. Striganov, Muon stopping power and range tables 10-MeV to 100-TeV, Atom. Data Nucl. Data Tabl. 78 (2001) 183–356. doi:10.1006/adnd.2001.0861.

[42] R. Wigmans, Calorimetry: Energy measurement in particle physics, Int. Ser. Monogr. Phys. 107 (2000) 1–726.

[43] B. N. Ratcliff, Imaging rings in ring imaging Cherenkov counters, Nucl. Instrum. Meth. A502 (2003) 211–221. doi:10.1016/S0168-9002(03)00276-6.

[44] Error analysis for efficiency, http://www.pp.rhul.ac.uk/~cowan/stat/notes/efferr.pdf, online; accesed 17-July-2015.

[45] P. K. F. Grieder, Cosmic rays at earth: Researcher's reference, manual and data book, Elsevier, Amsterdam, 2001.

[46] Web page for root, a data analysis framework by cern, https://root.cern.ch/drupal/, online; accesed 17-July-2015.

[47] M. T. Graham, The Two photon decay of the chi0 state of charmonium, Ph.D. thesis, Minnesota U. (2002).
URL http://www-spires.fnal.gov/spires/find/books/www?cl=FERMILAB-THESIS-2002-19

[48] Private talk with Howard Budd, Senior experimenter, University of Rochester and Fermilab, talk on February-2015.

[49] Minerva logbook entry where the plots using the tb calorimeter are shown with the old and new equation., http://dbweb4.fnal.gov:8080/ECL/minerva/E/show?e=45232, online; accesed 17-July-2015.

[50] Private talk with Eric Ramberg, General Detector Research and Development technical coordinator, Fermilab, talk on April-2015.

[51] Private talk with Win Baker, retired Senior experimenter, Fermilab, talk on March-2015.

[52] Document showing the complete version of the TB triger and DAQ., http://minerva-docdb.fnal.gov:8080/cgi-bin/RetrieveFile?docid=10793&filename=minerva-tb-trigger-and-daq-20150312.pdf&version=1, online; accesed 17-July-2015.

[53] B. Baldin, VME Data Acquisition Modules for MINERvA Experiment.